博 士 学 位 論 文

Doctoral Dissertation

Creating granitic geothermal reservoirs

by carbon dioxide injection

（二酸化炭素圧入による花崗岩質地熱貯留層の造成）

東北大学大学院環境科学研究科

Graduate School of Environmental Studies, Tohoku University

先進社会環境学専攻	専攻 major／コース course
学籍番号 Student ID No.	C0GD1502
氏　名 Name	Eko Pramudyo

<table>
<tr><td>指　導　教　員
Supervisor at Tohoku Univ.</td><td colspan="2">Prof. Noriaki Watanabe</td></tr>
<tr><td>研 究 指 導 教 員
Research Advisor at Tohoku Univ.</td><td colspan="2"></td></tr>
<tr><td rowspan="4">審　査　委　員
（〇印は主査）
Dissertation Committee Members
Name marked with “○” is the Chief Examiner</td><td colspan="2">〇　Prof. Noriaki Watanabe</td></tr>
<tr><td>1　Prof. Atsushi Okamoto</td><td>2　Assoc. Prof. Kiyotoshi Sakaguchi</td></tr>
<tr><td>3　Assoc. Prof. Masaoki Uno</td><td>4　Assist. Prof. Jiajie Wang</td></tr>
<tr><td>5</td><td>6</td></tr>
</table>

Table of Contents

Chapter 1 : Introduction

1.1. Background and Literature Review

Geothermal power generation has been predominantly operating on hydrothermal-type resources (Huttrer, 2020). Alternatively, enhanced geothermal systems (EGSs) are potentially feasible energy resources for providing baseload electricity (Tester et al., 2006). Over the last two decades, research on EGS development has expanded into the exploitation of superhot and supercritical geothermal environments (> c.a. 400 °C), which could increase the productivity and sustainability of power generation (Asanuma et al., 2012; Elders et al., 2018). Additionally, superhot geothermal reservoirs offer the potential benefit of geologic carbon storage because carbon dioxide (CO_2) is denser than the resident brine; hence, it descends (Parisio and Vilarrasa, 2020).

Studies have recently demonstrated that fracturing could contribute to EGS reservoir creation in superhot geothermal environments (Watanabe et al., 2017b; 2019), where a complex cloud-fracture network (CFN), i.e., a network of permeable microfractures densely distributed over the rock body (Figure 1.1), forms in granite as a result of injecting water at near or above its critical temperatures (374 °C for pure water and 400 °C for seawater). Parisio et al. (2021) suggested that fracturing in superhot geothermal environments is possible at up to approximately 600 °C, which is the theoretical limit of brittle crust in igneous provinces. The CFN is induced at lower injection pressures than during conventional hydraulic fracturing with colder water due to the stimulation of pre-existing microfractures by low-viscosity (< 100 μPa·s) water near or above its critical temperature. For example, if a vertical well is drilled into a rock with a 10 MPa tensile strength in a stress field, with 40 MPa maximum and minimum horizontal stresses and 90 MPa vertical stress, the breakdown pressure in conventional hydraulic fracturing would be 90 MPa. It is because conventional hydraulic fracturing using colder water (e.g., viscosity = 143.4 μPa · s at 200 °C and 40 MPa) in low-permeability rock requires a pressure equal to the sum of that required to reduce the concentrated stress across a particular plane on the borehole wall to zero and the tensile strength of the rock (Hubbert and Willis, 1957). Alternatively, low-viscosity water (e.g., viscosity = 39 μPa · s at 450 °C and 40 MPa) penetration would achieve CFN at pressure as low as approximately 50 MPa for the same fracturing scenario based on Watanabe et al. (2017b; 2019).

Nevertheless, studies have demonstrated that water utilization in superhot EGSs is characterized by specific challenges, such as difficulties in maintaining the permeability in a water-based superhot EGS owing to the competing process between free-face dissolution and the stress solution of fracture asperities (Watanabe et al., 2020), and concerns over fracture clogging by amorphous silica formed during phase changes in granite-reacted water from subcritical to supercritical or superheated steam in granite (Watanabe et al., 2021a). Moreover, water utilization for fracturing, as evaluated in shale-gas extraction operations, causes high-water footprints (Wilkins et al., 2016).

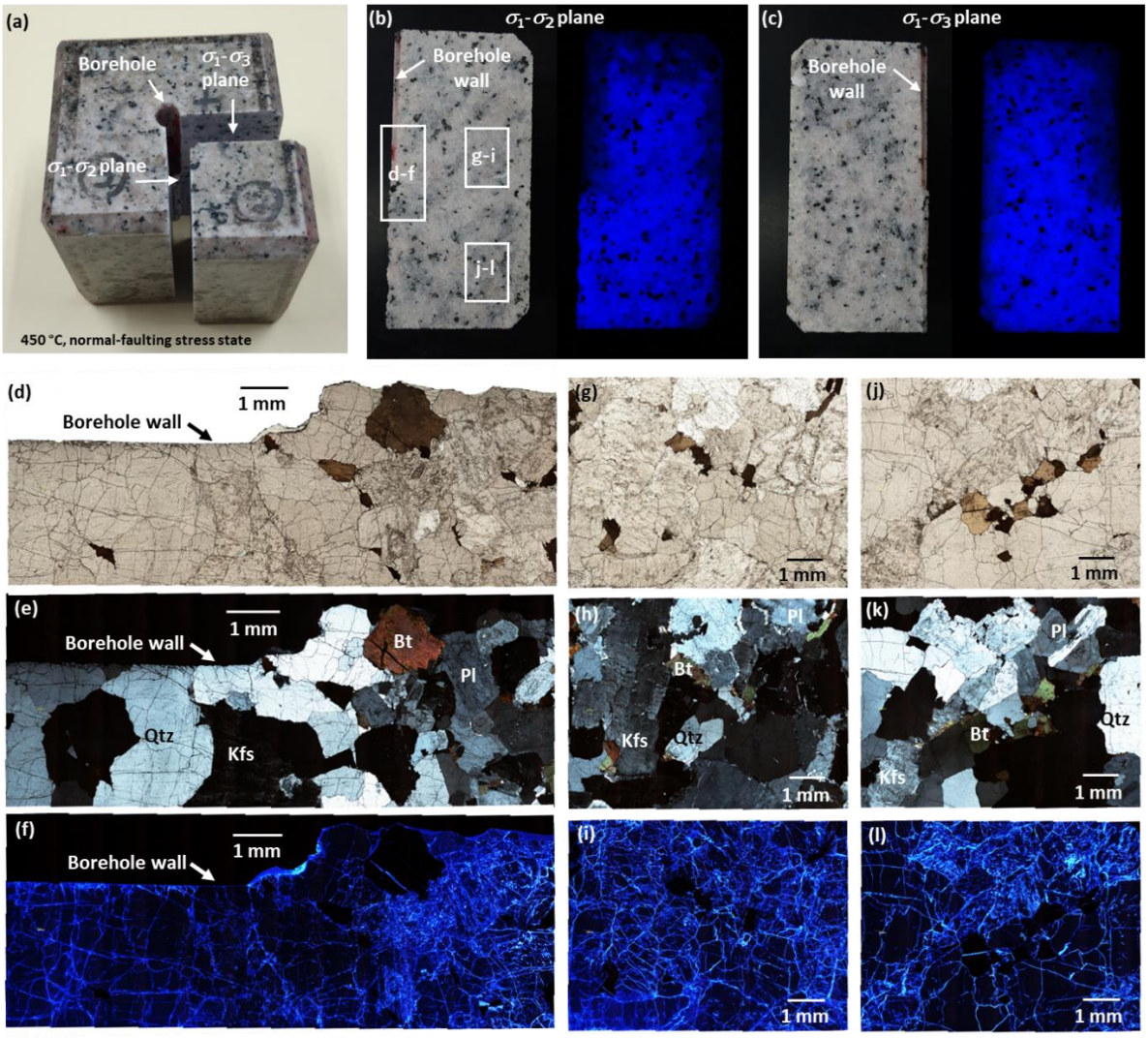

Figure 1.1. Complex cloud-fracture network in granite produced via water injection at 450 °C under true triaxial stress (σ_1: maximum principal stress, σ_2: intermediate principal stress, and σ_3: minimum principal stress), where a is the fluorescent-resin impregnated post-experimentation sample. b, c Even blue fluorescence over the cross-sections of both the centered σ_1–σ_2 and σ_1–σ_3 planes of the sample; optical microphotographs of a thin section of the σ_1–σ_2 plane cross-section near and far from the borehole using (d, g, j) uncrossed polarized, (e, h, k) crossed polarized, and (f, i, l) UV light. Adapted from Watanabe et al. (2019)

In petroleum industry, nitrogen gas (N_2), helium (He), and carbon dioxide (CO_2) have been the proposed fracturing-fluid alternatives as they are less reactive to rock-forming minerals (Gandossi and Estorff, 2015; Moridis, 2018). Accordingly, those fluids are proposed majorly for fracturing in shale formations, where unwanted reactions, such as clay swelling would occur in water injection. Among those fluids, CO_2 has emerged as a potential-alternative fracturing fluid for creating geothermal reservoir in granitic environments because in addition to being less reactive to rock forming minerals in geothermal environments (Brown, 2000), it is safer and easier to handle than N_2 and He, and does not require special equipment during fracturing operation, such as low temperature storage when N_2 is used

(Gandossi and Estorff, 2015; Moridis, 2018). CO_2 is denser than N_2 and He; hence, achieving intended pressures at greater depth is easier (Gandossi and Estorff, 2015; Moridis, 2018). Moreover, several studies have indicated that CO_2 reduces water footprint (Wilkins et al., 2016) and functions as heat-mining fluid (Brown, 2000; Pruess, 2006; Randolph and Saar, 2011). Based on Heidaryan et al. (2011), CO_2 has low viscosity (<100 μPa · s) at temperatures and pressures corresponding to conventional and superhot geothermal environments (approximately 150–500 °C, 10–100 MPa). For example, at 40 MPa, CO_2 viscosity at 150 and 450 °C are 49.4 μPa · s and 38.9 μPa · s, respectively. Therefore, CO_2 injection can be expected to induce CFN, not only in superhot geothermal environments but also in conventional geothermal environments (c.a. 150–300 °C).

To the best of the author's knowledge, only few laboratory fracturing experiments on granite have been performed using CO_2 and at geothermal conditions to date. Ishida et al. (2016) performed CO_2 fracturing of granite at low temperatures (<45 °C) and magnitudes of stress (σ_1 = 6 MPa, σ_2 = 4 MPa, σ_3 = 3 MPa; σ_1, σ_2, and σ_3 are the maximum, intermediate, and minimum principal stress, respectively). Later, Isaka et al. (2019) performed CO_2 fracturing of granite at 50–300 °C under confining stresses of 5–40 MPa, with a small differential stress of 5 MPa; however, the resulting fracture patterns in those studies were simple compared to the CFN, even though the fractures were tortuous. Therefore, it is suspected that despite low CO_2 viscosity similar to that of water at near or above its critical temperature, the observed differences were caused by the small differential stresses in their experiments (≤5 MPa), compared to the larger values (35–80 MPa) investigated in Watanabe et al. (2017b; 2019).

To date, the laboratory CO_2 fracturing experiments, including experiments to create CFNs, were performed on intact rock samples. However, natural (i.e., pre-existing) fractures can be present in geothermal environments. Tester et al. (2006) implies that natural fractures with a length of approximately 1–10 m are those that may contribute to reservoir connectivity, when hydroshearing (i.e., inducing shear-slip by fluid injection) of the natural fractures is performed. Therefore hereafter, the term "natural fracture" and "naturally fractured (geothermal) environment" refer to pre-existing fractures with length in meter scale and geothermal environment containing network of meter-scale pre-existing fractures, respectively. Hydroshearing has been the major stimulation method in naturally fractured environments (Rinaldi et al., 2015); nevertheless, desired-reservoir connectivity is not always achieved (Batchelor, 1986; Wallroth et al., 1999; Tester et al., 2006; Lu, 2018). Moreover, creating induced fractures via cold-water injection is difficult in naturally fractured environments (Pine and Batchelor, 1984).

Alternatively, CO_2 injection is expected to induce not only shear-slip on the natural fractures but also CFN formation in the matrix (unfractured rock) part by stimulating the pre-existing microfractures. Although fluid flow in these environments is mostly controlled by the stimulated natural fractures (Cornet and Jianmin, 1995; Evans et al., 2005), CFN could potentially provide additional connections between the stimulated natural fractures. Moreover, CO_2 injection has been assumed to produce dynamic slip on a larger area (implying larger shear displacement) than water injection (e.g., Rutqvist and Rinaldi, 2019), increasing the chance of large permeability enhancement according to Ishibashi et al. (2016). This remained to be verified by laboratory experiments performed at geothermal temperatures.

Therefore, the possibility and characteristics of CO_2 injection induced CFN in naturally fractured geothermal environments, along with the shearing of the natural fractures need to be clarified.

Nevertheless, experimental results from Isaka et al. (2019) imply a potential challenge in fracturing using CO_2, where CFNs formed at relatively small differential stresses are expected to comprise small number of fractures or fractures with narrow aperture. Such challenge is also expected in CFNs formed at conventional geothermal temperatures, as experimental results from Watanabe et al. (2017b) exhibited a decreasing trend in the number of fractures appearing in X-ray computed tomography (CT) sections from 450 to 360 °C. The apparent temperature dependence of CFNs was suspected to be correlated to temperature dependence of mechanical properties of granite. For example, based on Heuze (1983), Young's modulus of granite is higher at conventional geothermal temperatures than that at superhot geothermal temperatures, which implies that rocks would be less deformable in conventional geothermal environments than in superhot geothermal environments. Therefore, additional stimulation methods to overcome such challenges need to be elucidated. For instance, at conventional geothermal conditions, further stimulation using chelating agent injection may be effective in increasing the fracture aperture via minerals dissolution, as implied by Rose et al. (2010).

1.2. Objectives and Thesis Structure

This study aimed to elucidate the possibility and characteristics of CO_2 injection-induced fracturing, CO_2 injection-induced fracturing and shearing of natural fractures in naturally fractured environments, and chelating agent injection as an additional stimulation method to improve CO_2 injection-induced fracture network permeability, in an attempt to create granitic geothermal reservoirs. To achieve the objectives, literature review and experimental works were performed; they are discussed within five chapters in this thesis, including this chapter (Chapter 1).

In Chapter 2, the author discusses the possibility and characteristics of CO_2 fracturing in granite at geothermal conditions based on a series of experiments under conventional- and true-triaxial stress states. A set of experiments under conventional-triaxial stress conditions were performed to clarify the influence of temperature and differential stress variation on the fracture formation pressure, and the characteristics of the resulting CFNs. An experiment was performed under true-triaxial stress condition, to verify the process of CO_2 fracturing on larger scale under a more realistic condition.

In Chapter 3, the possibility of achieving CFNs and their characteristics in naturally fractured geothermal environments, along with shearing of the natural fractures, were clarified through a set of experiments performed on cylindrical samples containing sawcut inclined from the samples' axis. Initially, a set of experiments was performed without fluid injections to clarify the sawcut friction coefficient at conventional and superhot geothermal temperatures, along with the shear slip characteristics. Then, experiments involving CO_2 injection were performed at conventional and superhot geothermal temperatures to elucidate the possibility and characteristics of CO_2 injection-induced shearing and CFN formation with respect to temperature difference. An experiment with water injection was also performed at a conventional temperature to examine the advantages and challenges of CO_2 injection compared to those of water injection.

In Chapter 4, the author experimentally elucidated the characteristics of additional stimulation using chelating agent injection to improve CO_2 injection-induced CFN permeability at conventional geothermal conditions. A series of experiments was performed under conventional-triaxial stress states to examine the effect of varying differential stress on the permeability enhancement process by chelating agent injection at weakly acidic and alkaline condition. An experiment was performed on a thermally fractured cubic granite sample subjected to a true-triaxial stress to elucidate the permeability enhancement process on a larger scale under radial flow condition. Based on those experiments, combined with literature studies, several possible schemes were made for creating geothermal reservoir via CO_2 injection and additional stimulations.

In Chapter 5, the author provides comprehensive conclusions on the possibility, characteristics, advantages, and challenges of creating granitic geothermal reservoirs via CO_2 injection from conventional to superhot geothermal conditions, including the potential methods to overcome the challenges.

Chapter 2 : Possibility and Characteristics of CO_2 Fracturing

2.1. Introduction

In this chapter, of which the contents have been published as Pramudyo et al. (2021), the author discusses the results of CO_2 fracturing experiments in granite at conventional and superhot geothermal conditions. Ishida et al. (2016) and Isaka et al. (2019) have reported that CO_2 penetration (e.g., viscosity = 49.4 μPa · s at 150 °C and 40 MPa) achieves tortuous and branching fractures in granite under relatively small differential stress conditions. However, those fractures were simpler than cloud-fracture networks (CFNs) that form by the penetration of water near and above its critical temperature (e.g., viscosity of 39 μPa · s at 450 °C and 40 MPa) under large differential stress conditions (Watanabe et al., 2017b; 2019; Goto et al., 2021), despite the similarity in CO_2 and water viscosities at the respective experimental conditions. It was thus hypothesized that CFNs would form at conventional and superhot geothermal temperatures under large differential stress conditions. The CO_2 fracturing experiments discussed in this chapter were performed to clarify the possibility of CFN formation in conventional and superhot geothermal environments and to elucidate the process and characteristics of the resulting CFNs. The author introduces the experimental systems and procedures incorporated in the experiments, including the pre- and post-experimental investigation on the sample. The experiments comprised a set of five CO_2-fracturing experiments on dry cylindrical granite samples at 200–450 °C under varying conventional-triaxial stress states and a CO_2-fracturing experiment on a large cubic granite sample at 300 °C under a true-triaxial stress condition. The author presents the characteristics of the resulting CFNs with respect to temperature variation under the same-differential stress and differential stress variation at the same temperature. The CFN formation mechanism and the applicability of the well-known Griffith failure criterion to predict CFN-formation pressure is also discussed. The author discusses the potential implications of the present-experimental results for creating granitic-geothermal reservoirs in conventional and superhot geothermal environments.

2.2. Material and Methods

2.2.1. Experiment under Conventional Triaxial Stress

For the fracturing experiments under conventional stress states, cylindrical granite samples (diameter, 30 mm; length, 25 mm) with a single borehole (diameter, 1.5 mm; length, 10 mm) were prepared using Inada granite from Ibaraki prefecture, Japan (Figure 2.1.a). Inada granite is medium-grained, chosen for its extensive historical research and well-characterized properties. The tensile and compressive strengths, Young's modulus, porosity, and intrinsic permeability of the granite near atmospheric pressure are 4–9 MPa, 160–180 MPa, 55–80 GPa, 0.5−0.8%, and 2×10^{-18}–8×10^{-18} m^2, respectively (Table 2.1) (Watanabe et al., 2017a; Goto et al., 2021; Yamaguchi, 1970; Lin et al., 2003). The same granite was used in previous studies on hydraulic fracturing in superhot geothermal conditions (Watanabe et al., 2017b; Watanabe et al., 2019; Goto et al., 2021).

X-ray computed tomography (CT) and permeability measurements were performed on the samples pre- and post-experiments. The X-ray CT was performed under dry, room temperature (approximately

23 °C), and pressure conditions at an X-ray tube voltage of 120 kV, a tube current of 150 μA, and a voxel size of 25 μm × 25 μm × 25 μm to verify the formation of a complex fracture pattern at the voxel-scale rather than obtaining an entire network image, which required thin-section observations. Notably, visual observations of the samples after these experiments generally suggest that the number of fractures visible in the CT images is smaller than the actual number. The sample permeability was measured in a radial flow geometry at room temperature and atmospheric pressure by injecting water into the borehole with graphite gaskets (Watanabe et al., 2017b; Goto et al., 2021).

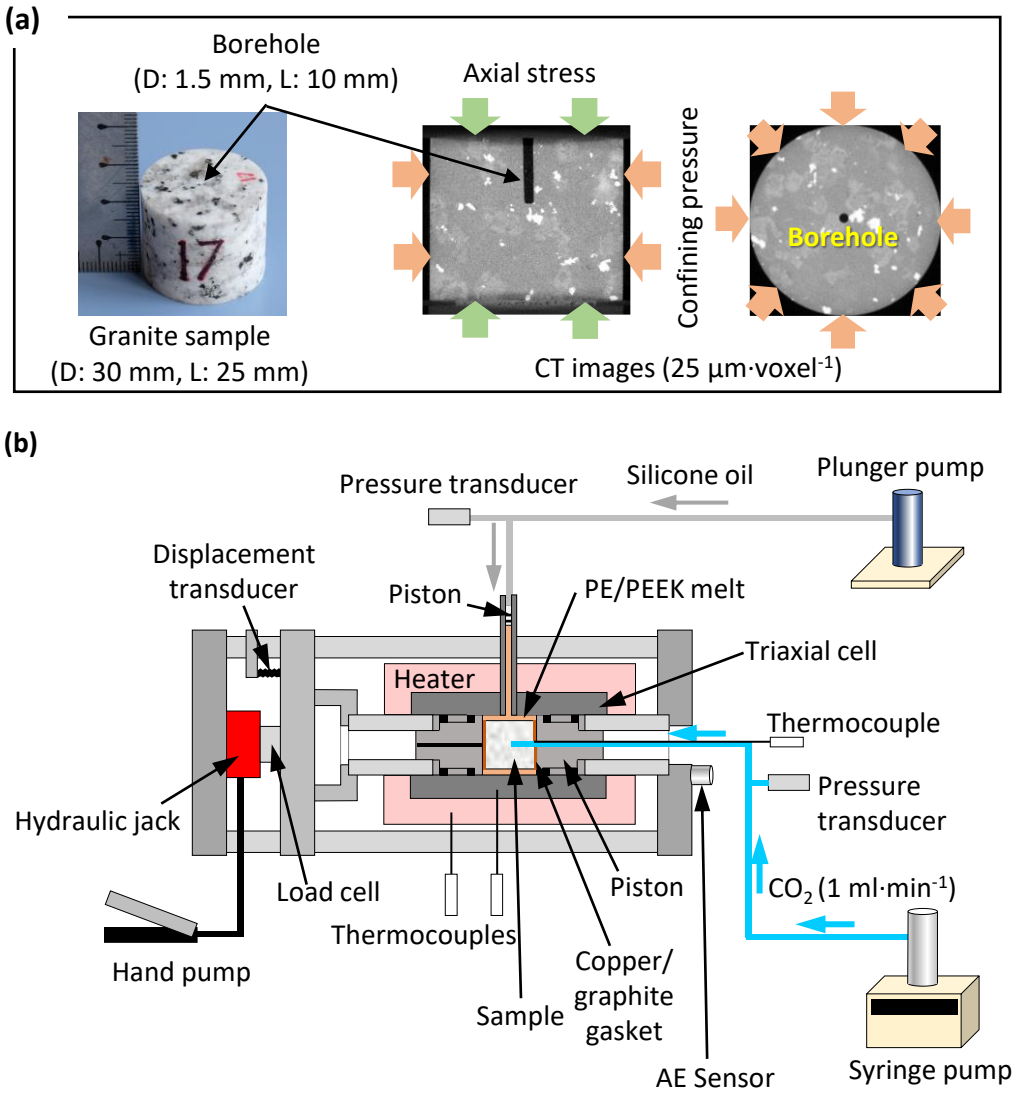

Figure 2.1. (a) Granite sample and loading conditions, and (b) design of the fracturing experiment under conventional triaxial stress

The experiments were performed using an experimental system (Figure 2.1b) first developed by Watanabe et al. (2017a). The special triaxial cell employed a high-viscosity plastic melt as a confining pressure fluid and a 50-μm thick plastic film (polyimide) as a sleeve for the sample. The plastic melt was either polyether ether ketone (PEEK) or polyethylene (PE). PEEK melts at 343 °C and is used for

experiments performed at temperatures ranging from 350 to 500 °C, whereas PE melts at 120 °C (Watanabe et al. 2017b), decomposes at approximately 370 °C (Walendziewski and Steininger, 2001), and is used for experiments performed at 150–300 °C. The polyimide plastic film does not have a melting point (it decomposes before melting at >500 °C). A tube with a PEEK or PE rod, which injects PEEK or PE melt at the experimental temperature, was attached to the upper part of the cell. PEEK or PE melt injection provided confining pressure and was controlled using a metallic piston that was displaced by pumping silicone oil at a constant pressure.

Table 2.1. Mechanical and hydraulic properties of Inada granite

Property	Value
Tensile strength (MPa)	4 – 9
Compressive strength (MPa)	160 – 180
Young's modulus (GPa)	55 – 80
Porosity (%)	0.5 – 0.8
Intrinsic permeability (m^2)	2×10^{-18} – 8×10^{-18}

The axial stress (corresponds to the maximum principal stress, σ_1) in the triaxial cell was provided by two cylindrical pistons with an axial hole for fluid flow. The piston positioned at the injection side was equipped with an injection pipe connected to a syringe pump. The axial load was applied by a handpump-operated hydraulic jack that displaced the piston on the production side. Axial stress was induced in the sample through copper or graphite gaskets placed between the piston and the sample end faces, where the gasket at the injection side had a hole.

Acoustic emission (AE) measurements were performed to determine the breakdown pressure (or fracture pressure) during fluid injection using an AE measurement device (Physical Acoustics Corporation's two-channel data acquisition and digital signal processing AE system, PCI-2) with an AE sensor (R15α 150-kHz resonant frequency sensor, Physical Acoustics Corporation). The AE device with the sensor gathers acoustic signals through axial load pistons, an amplifier, and a computer for recording and processing.

For the experiment, the polyimide-film-wrapped sample was first placed inside the PEEK or PE cylinder within the triaxial cell. Then, the gaskets were attached to the sample end faces. The triaxial cell was then placed inside an electric furnace, and at a relatively small axial stress (approximately 7 MPa) maintained by a hydraulic jack, the temperature was increased to a prescribed value, melting both the PEEK or PE cylinder and the bottom part of the plastic-rod. The sample was then loaded by a prescribed axial stress, followed by a prescribed confining pressure corresponding to both intermediate (σ_2) and minimum principal stress (σ_3).

Throughout the experiments, CO_2 was injected at a constant flow rate of 1 $ml \cdot min^{-1}$ at room temperature using a syringe pump. Injection was started from an initial borehole pressure of 10 MPa, at which CO_2 existed in the liquid phase within the syringe pump at room temperature, thus enabling flow

rate control. The injected CO_2 was heated to the experimental temperature in the injection pipe before delivery to sample face. The CO_2 injection was terminated when CFN formation was verified either by an increase in AE activity, the occurrence of a connection between the borehole and confining pressures, or the escape of gas from the triaxial cell.

Goto et al. (2021) elucidated CFN formation via flow-induced micro-fracturing and the applicability of the Griffith failure criterion under superhot geothermal conditions. Accordingly, fluid flow and the resultant stimulated zone first occurred in zones with relatively high permeability created by pre-existing microfractures. Micro-fracturing propagated as the fluid pressure gradient between the stimulated and unstimulated zones increased, thus increasing the fluid flow into the unstimulated zone. Because fracturing is induced by water penetration into pre-existing microfractures, the injection pressure can be assumed to be similar to the pore pressure; therefore, the breakdown pressure may also be similar to the pore pressure required for fracturing/failure (fracture pressure, $P_{p,frac}$) and can be predicted by the Griffith failure criterion assuming fracturing originated from preexisting fractures, according to Eqs (2.1) and (2.2) (Griffith, 1924; Jaeger et al., 2007; Secor, 1965; Cox, 2010).

$$P_{p,frac} = \frac{8\sigma_t(\sigma_1+\sigma_3)-(\sigma_1+\sigma_3)^2}{16\sigma_t} \text{ at } (\sigma_1 - \sigma_3) \geq 4\sigma_t, \tag{2.1}$$

$$P_{p,frac} = \sigma_3 + \sigma_t \text{ at } (\sigma_1 - \sigma_3) < \sigma_t, \tag{2.2}$$

where σ_t is the rock tensile strength.

Table 2.2 enlists the temperatures and stress conditions of the experiments performed. To clarify CFN formation and applicability of Griffith failure criterion at superhot geothermal conditions, two experiments were performed at 450 °C with differential stress values of 50 MPa (Experiment 1, σ_1 = 90 MPa, $\sigma_2 = \sigma_3$ = 40 MPa) and 65 MPa (Experiment 2, σ_1= 90 MPa, $\sigma_2 = \sigma_3$ = 25 MPa). These temperature and stress conditions were selected to compare the present results to those in the previous water fracturing at the same (Experiment 1) or similar (Experiment 2) condition (Watanabe et al., 2017b; Goto et al., 2021). Based on Eq. (2.1), it was expected that Experiments 1 and 2 would yield breakdown pressures of 42.7 and 19.8 MPa, respectively, assuming σ_t = 7 MPa. The σ_t value was selected based on evidence from previous works (Watanabe et al., 2017a; Watanabe et al., 2017b; Watanabe et al., 2019; Goto et al., 2021), which corresponded to the known range of 4–9 MPa for equivalent granite. Note that in the Experiment 2, the maximum available borehole pressure was limited to 25 MPa (i.e., equal to confining pressure) to verify that fracturing could occur at pressure levels below confining pressure, as expected.

To clarify CFN formation and applicability of the Griffith failure criterion under conventional geothermal conditions, two experiments were performed at 200 °C, one with 50 MPa differential stress (Experiment 3, σ_1 = 90 MPa, $\sigma_2 = \sigma_3$ = 40 MPa) and the other with 65 MPa differential stress (Experiment 4, σ_1 = 90 MPa, $\sigma_2 = \sigma_3$ = 25 MPa). These experiments were also expected to yield breakdown pressures of 42.7 and 19.8 MPa for Experiments 3 and 4 respectively, assuming σ_t of 7 MPa. The tensile strength was assumed to be constant throughout the temperature range in this study (200–

450 °C). Based on Heuze (1983), Westerly granite tensile strength decreased by approximately 3 MPa from 200 to 450 °C; however, equal σ_t values were assumed for all present experiments because variations could occur among different samples, even at the same temperature, as inferred from the breakdown pressures revealed in previous studies (Watanabe et al., 2017b; Watanabe et al., 2019; Goto et al., 2021; Heuze, 1983).

Table 2.2. Conditions of the fracturing experiments under a conventional triaxial stress state (Experiments 1–5), and true triaxial stress state (Experiment 6)

Experiment	Temperature (°C)	Stress (MPa)				Triaxial stress state
		σ_1	σ_2	σ_3	$\sigma_1 - \sigma_3$	
Experiment 1	450	90	40	40	50	Conventional
Experiment 2	450	90	25	25	65	Conventional
Experiment 3	200	90	40	40	50	Conventional
Experiment 4	200	90	25	25	65	Conventional
Experiment 5	300	90	40	40	50	Conventional
Experiment 6	300	40	15	5	35	True

Temperature dependencies in the fracturing characteristics, such as the fracture apertures and permeabilities, were expected from these experiments. Therefore, to elucidate the temperature dependencies, an experiment was performed at 300 °C with 50 MPa differential stress (Experiment 5, σ_1 = 90 MPa, $\sigma_2 = \sigma_3$ = 40 MPa); thus, in conjunction with Experiments 1 and 3, the influence of temperature on the fracturing characteristics can be evaluated under the same stress conditions.

2.2.2. Experiment under True Triaxial Stress

Fracturing experiments under a true triaxial stress state with AE measurements were performed at 300 °C (Experiment 6, Table 2.2) to verify CFN formation at a conventional geothermal temperature and to reveal the detailed characteristics of CO_2 fracturing on a larger scale and under a more realistic stress condition. The experiment was performed at σ_1 = 40 MPa, σ_2 = 15 MPa, and σ_3 = 5 MPa, where the maximum principal stress was set to vertical. The same stress state has been used in several hydraulic fracturing experiments under superhot geothermal conditions (Goto et al., 2021, Watanabe et al., 2019); thus, a comparison of the results among the studies could be made.

For this experiment, a cube (100 mm × 100 mm × 100 mm) of Inada granite was prepared with a single borehole (diameter, 10 mm; length, 50 mm) at the center (Figure 2.2a). The edges of the sample were chamfered to accommodate deformation during the experiment, resulting in a 90 mm × 90 mm loading face on each side. Analyses were performed using an experimental system that was originally developed by Watanabe et al. (2019) and Goto et al. (2021). It predominantly comprised a true triaxial cell that uses a plastic (PEEK or PE) melt to seal along the chamfered edges covered by the polyimide film, a triaxial loading system, a pump (syringe or plunger) to inject fluids into the sample, a pump (syringe or plunger) for injecting the plastic melt, an elastic wave measurement system (P-wave or AE

measurement system), and a temperature control and data logging system.

The true triaxial cell comprised a pressure vessel with a cubic skeleton, six pistons that apply a compressive load to the cubic rock sample via a copper gasket, a plastic filling that melts and seals the sample edges at the experimental temperature, a plastic melt injector to control the melt's pressure, and thermal insulators used in conjunction with heaters for the pressure vessel (Figure 2.2). The pressure vessel had six cylindrical holes to allow the pistons to be inserted into the vessel, with graphite packing placed at the sliding portion to provide sealing for the plastic melt. The main body of the piston had a cylindrical shape with a square loading face that corresponded to that of the sample. This geometry created spaces between the chamfered edges of the piston and the chamfered edges of the sample, which are then filled with polyethylene (PE) plastic fillings. During the experiment, the PE filling was melted and pressurized to seal the pore pressure. The pressurization was performed by injecting more PE at a constant pressure using an injector tube, and to prevent the PE melt from sticking to the rock surface; the polyimide film was used to cover the sample edges, as depicted in Figure 2.2a.

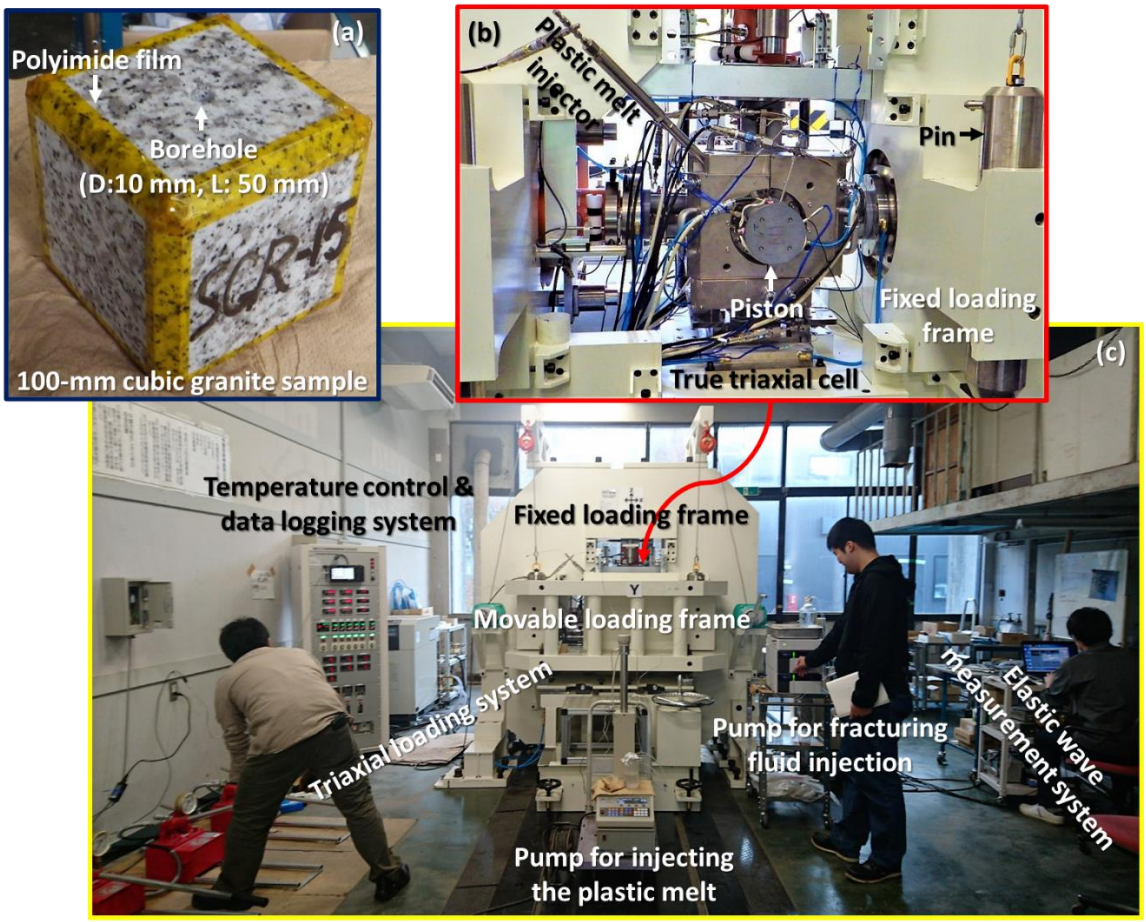

Figure 2.2. (a) Granite sample, (b) High-temperature true triaxial cell, and (c) experimental fracturing system under true triaxial conditions (adapted from Watanabe et al., 2019)

The piston main body was also equipped with four cartridge heaters, a pipe for fluid injection or production, and a thermocouple inside the pipe to measure temperatures near the sample face. As an

injection pipe, the pipe was connected to a pump. A copper gasket with grooves, either to directly inject fluid into the borehole or to gather the produced fluid to production pipes, was placed between the piston and the loading faces of the sample. The AE sensor was attached to the end face of the elastic wave guide bar, located at the opposite side of the piston loading face. The bar temperature was maintained near room temperature using a cooling jacket circulating water from a chiller.

The true triaxial cell was placed into a triaxial loading system comprising one fixed and two movable frames (Figure 2.3). The cell was placed on a loading platform of the fixed frame with extreme care to prevent loading eccentricity. When a compressive load was applied, the movable loading frame engaged the fixed frame using four cylindrical pins. Three hydraulic rams in the loading frames pushed the true triaxial cell pistons via a spherical seated platen. Piston displacement was ascertained to measure the sample deformation with linear variable differential transformer (LVDT) displacement transducers. The platen was maintained near room temperature via water circulation through narrow channels.

After preparing the experimental system, the temperatures of the pressure vessel and pistons were increased to 300 °C, while a hydrostatic load was applied to the sample according to the minimum principal stress (5 MPa). Once at temperature, the PE melt was injected into the pressure vessel at 4 MPa, and the sample was then subjected to a prescribed true triaxial stress state. Pressure-controlled CO_2 was injected into the borehole and increased stepwise at 2 MPa pressure increments, maintaining each level for approximately 60 s. The injected CO_2 reached the experimental temperature along the flow path before arriving at the sample face. During injection, the valves of the five production pipes were closed to prevent external flow, as in previous hydraulic fracturing experiments (Watanabe et al., 2017b; Watanabe et al., 2019).

To verify CFN formation, P-wave velocity measurements were performed pre- and post-fracturing experiment under dry, room temperature, and atmospheric pressure conditions. For measurement, each sample face was divided into 3 × 3 pixels, and the travel time between each of the opposing pairs at 100 mm distance was measured to compute 27 P-wave velocities. The measurements provided the distribution of P-wave velocities within the sample, and these velocities at each voxel were estimated to assess the fracture pattern by solving a system of 27 equations of the form of Eq. (2.3):

$$\frac{1}{V_p} = \frac{\frac{1}{V_{p1}}+\frac{1}{V_{p2}}+\frac{1}{V_{p3}}}{3}, \tag{2.3}$$

where V_p is the velocity for each pixel pair, and V_{p1}, V_{p2}, and V_{p3} are the respective velocities for voxels between pairs.

A thin section was obtained from the resin-impregnated fractured sample to verify CFN formation via optical microscopy (Nishiyama and Kusuda, 1994; Nishiyama et al., 2002). Prior to acquisition, the fractured sample was first impregnated with a thermosetting acrylic resin mixed with a fluorescent substance. The sample was then cut to expose its interior, where a thin section was obtained from the σ_1–σ_3 plane. Fractures were assessed based on a marked difference in brightness under ultraviolet (UV) light irradiation.

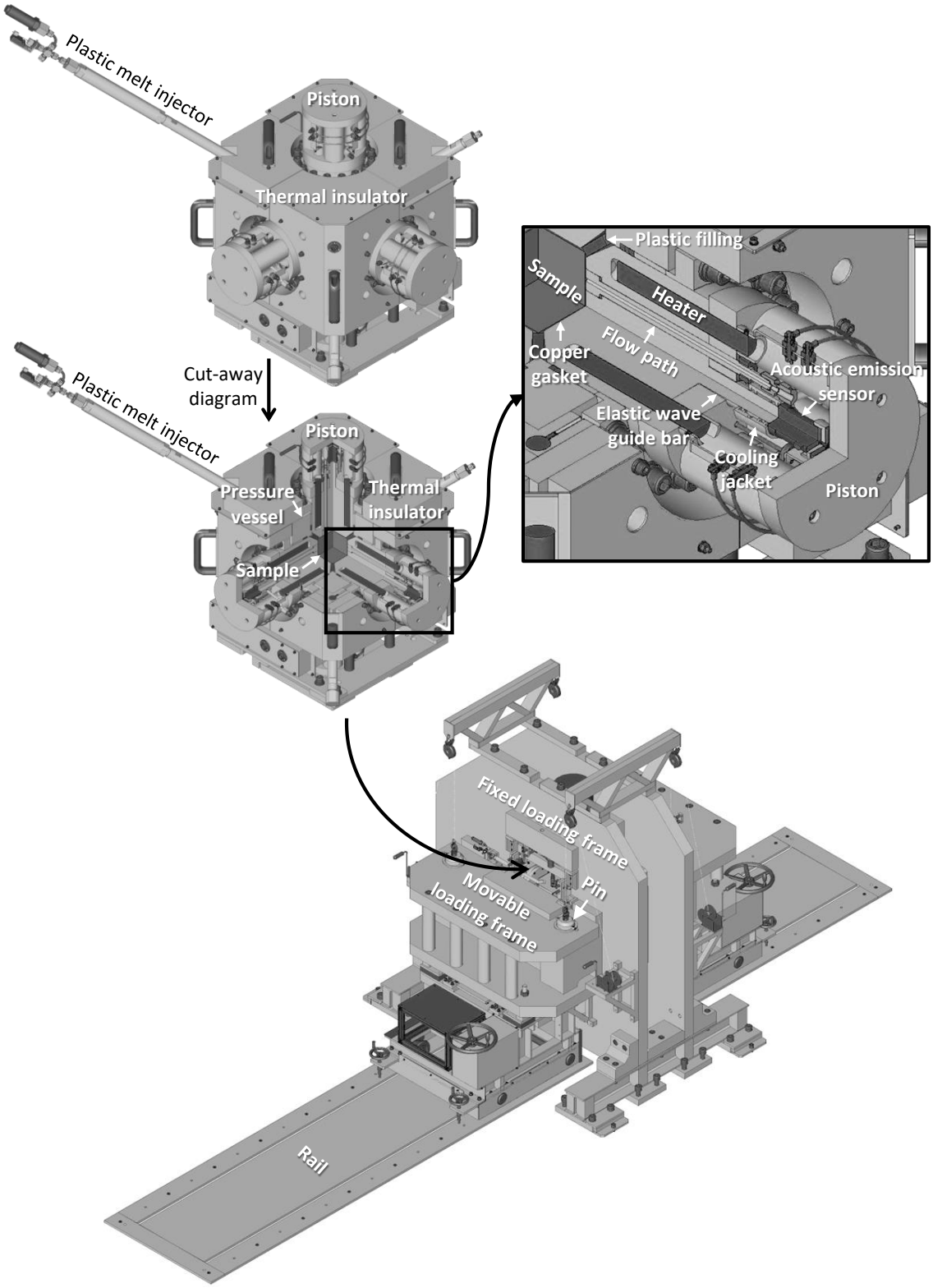

Figure 2.3. Three-dimensional design of the high-temperature true triaxial cell and triaxial loading frame

2.3 Results and Discussion

2.3.1. CO_2 Fracturing in Superhot Geothermal Conditions

Figure 2.4 depicts the borehole pressure and AE energy behaviors during Experiment 1 (450 °C, σ_1 = 90 MPa, $\sigma_2 = \sigma_3$ = 40 MPa) and an X-ray CT image of the sample post-experimentation. In the AE measurement device used in this study, AE energy was computed as the time integral of the absolute signal voltage and reported in arbitrary units (arb. unit). The breakdown pressure was determined to be 39 MPa, as indicated by the onset of a significant increase in the AE energy. The AE energy profile also demonstrated several prior peaks likely caused by some deformation of pre-existing microfractures (Knill et al., 1968). CO_2 injection was stopped at c.a. 45 MPa when an increase in the confining pressure indicated the formation of fractures connecting the borehole and sample surface, and the borehole pressure was gradually decreased. The X-ray CT images from the sample demonstrated a complex fracture pattern with approximately 11 visible-fractures per cm^2 (highlighted in yellow in all subsequent images when they had relatively small apertures and, thus, low visibilities on a gray scale). The fractures on the surface of this sample caused detachment of some mineral grains, which precluded the permeability measurement post the experiment. Even so, it was estimated that the fractures would yield a permeability in the range of 10^{-15} to 10^{-12} m^2 based on the results of previous studies (Watanabe et al., 2017b; Watanabe et al., 2019; Goto et al., 2021).

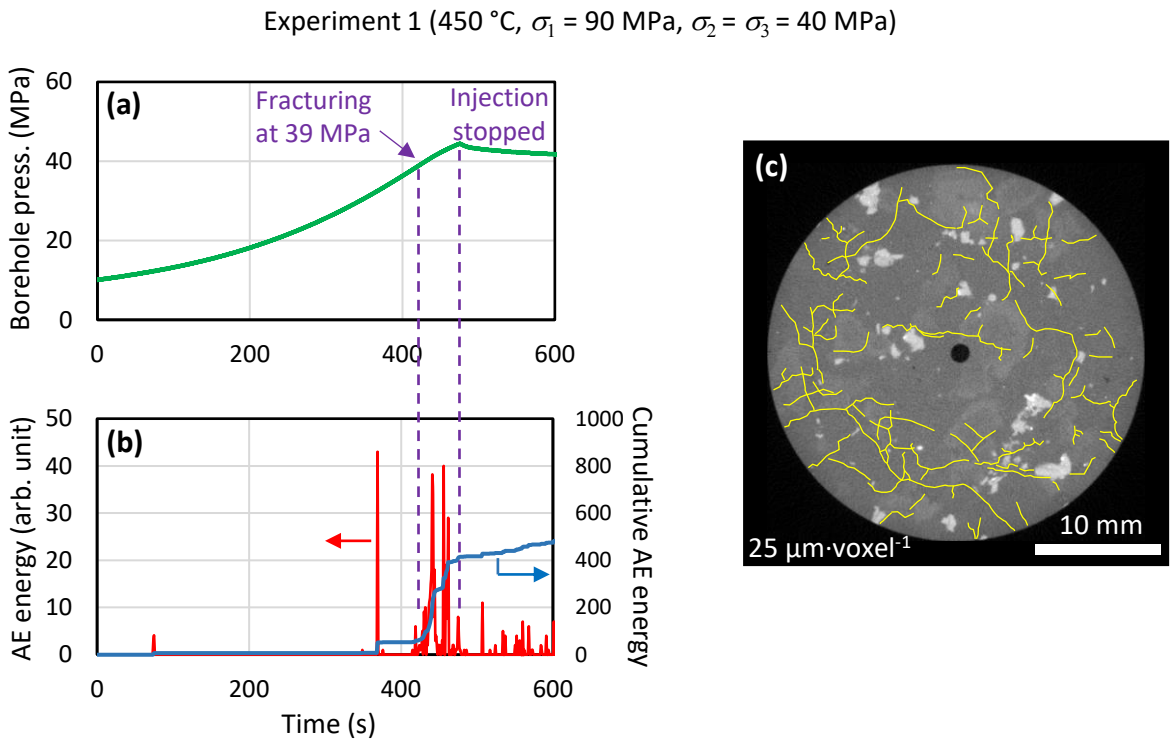

Figure 2.4. (a) Borehole pressure, (b) AE energy (red line) and cumulative AE energy (blue line) during Experiment 1, and (c) post-experimental X-ray CT image of the sample. Relatively small apertures are highlighted in yellow to increase gray scale visibility

Similar AE energy behaviors, breakdown pressure levels, and fracture pattern complexities were observed in hydrofracturing experiments under the same temperature and stress conditions (Watanabe et al., 2017b; Goto et al., 2021). Watanabe et al. (2017b) suggested that the CFN observed were formed through infiltration and stimulation of pre-existing microfractures by low-viscosity water. Hence, Goto et al. (Goto et al., 2021) suggested the applicability of the Griffith failure criterion for fracturing formation. The breakdown pressure in Experiment 1 (39 MPa) was close to the fracture pressure value predicted by Eq. (2.1), 42.7 MPa at σ_t = 7 MPa (Figure 2.5), and some degree of difference between breakdown pressures was observed in previous studies (Watanabe et al., 2017b; Watanabe et al., 2019; Goto et al., 2021); however, the overall experimental values still largely aligned with those predicted. Therefore, along with the ability of low-viscosity CO_2 to penetrate and stimulate pre-existing microfractures, the breakdown pressures suggested that the Griffith failure criterion may also be upheld in CO_2 fracturing.

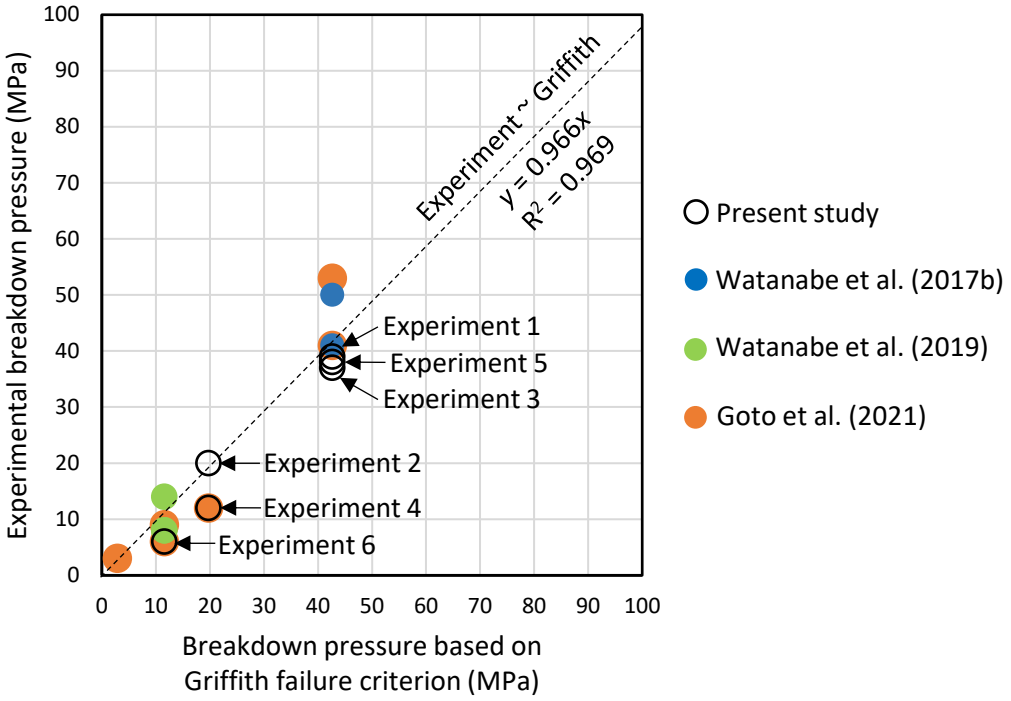

Figure 2.5. Comparison between the breakdown pressures observed and the calculated Griffith failure criterion under the assumption of a constant tensile strength of 7 MPa in the present and previous studies (water fracturing at 360–450 °C)

The results of Experiment 2 (450 °C, σ_1 = 90 MPa, $\sigma_2 = \sigma_3$ = 25 MPa) indicated that the AE energy started to increase when the borehole pressure reached 20 MPa (Figure 2.6), thus indicating an extremely close breakdown pressure to the predicted failure criterion (19.8 MPa) for σ_t of 7 MPa (Figure 2.5). The post-experiment X-ray CT images of the sample demonstrated not only the formation of a complex fracture pattern but a larger number of wide-aperture fractures (> 50 visible-fractures per cm^2) than Experiment 1, with a smaller differential stress and same temperature. Furthermore, the sample sustained

large-scale damage so that it needed to be kept within the plastic cylinder to prevent further disintegration and, thus, precluded the post-experiment permeability measurements for this sample. Referring to previous research (Watanabe et al., 2017b; Watanabe et al., 2019; Goto et al., 2021), however, it was estimated that the fractured sample in Experiment 2 had a permeability $>10^{-12}$ m^2.

In this study, quantifications on the characteristics of CFNs, for example fracture aperture and its changes with varying experimental conditions, were precluded due to considerable uncertainties (related to the resolution) in the X-ray CT based measurements. Additionally, the quantitative discussion would be vague, as the fracture apertures should have been wider at atmospheric conditions than those under experimental condition. Therefore, most discussions on the characteristics of CFNs are limited to qualitative descriptions based on visual observation on X-ray CT sections and permeability measurements when possible.

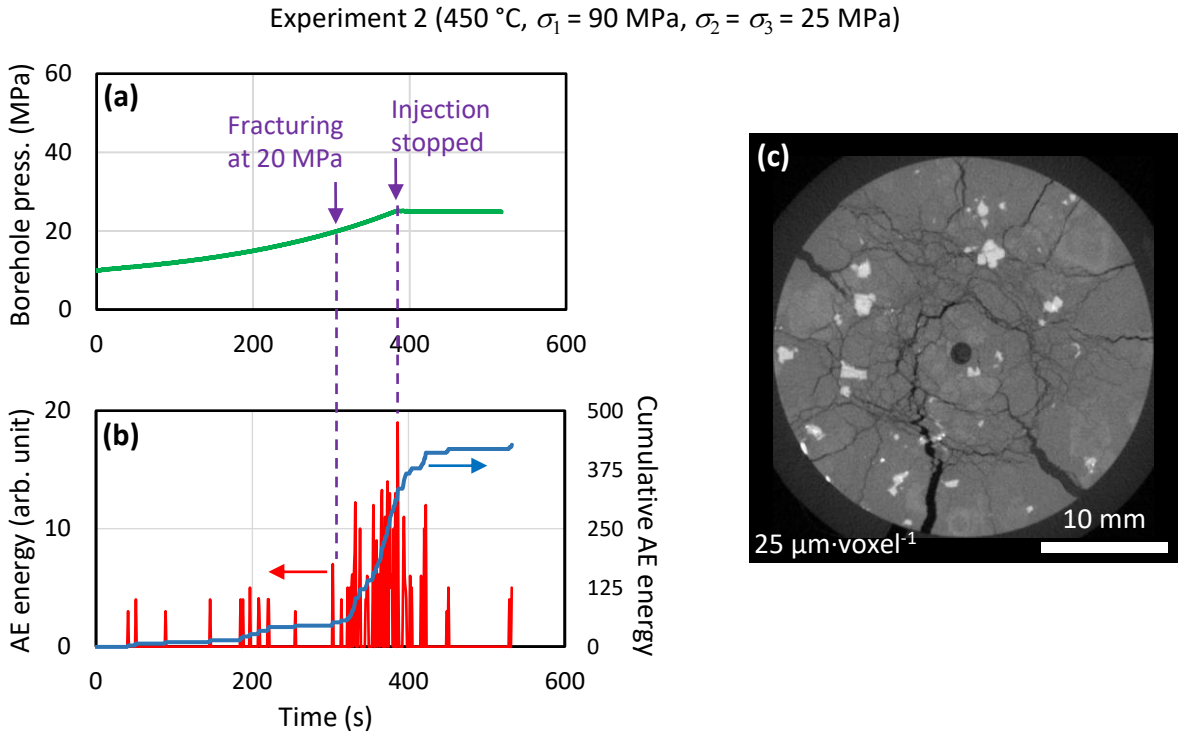

Figure 2.6. (a) Borehole pressure, (b) AE energy (red line) and cumulative AE energy (blue line) during Experiment 2, (c) post-experimental X-ray CT image of the sample

Similar responses of breakdown pressure and fracture aperture to increases in differential stress were also observed in hydraulic hydrofracturing experiments performed at the same temperature and differential stresses of 50 and 80 MPa (Goto et al., 2021), and it was again verified that the Griffith failure criterion was applicable. Aperture changes with differential stress may be caused by a change in shear deformation of the fractures. When a differential stress is applied to a rock containing a fracture network, shear deformation occurs in the fractures inclined to σ_1, causing dilation of the fractures parallel and subparallel to the σ_1 direction (i.e., perpendicular or sub-perpendicular to the σ_3 direction, Figure 2.7). This process might also provide a certain degree of dilation for the inclined fractures via the

self-propping mechanism, owing to the roughness of the fracture surfaces.

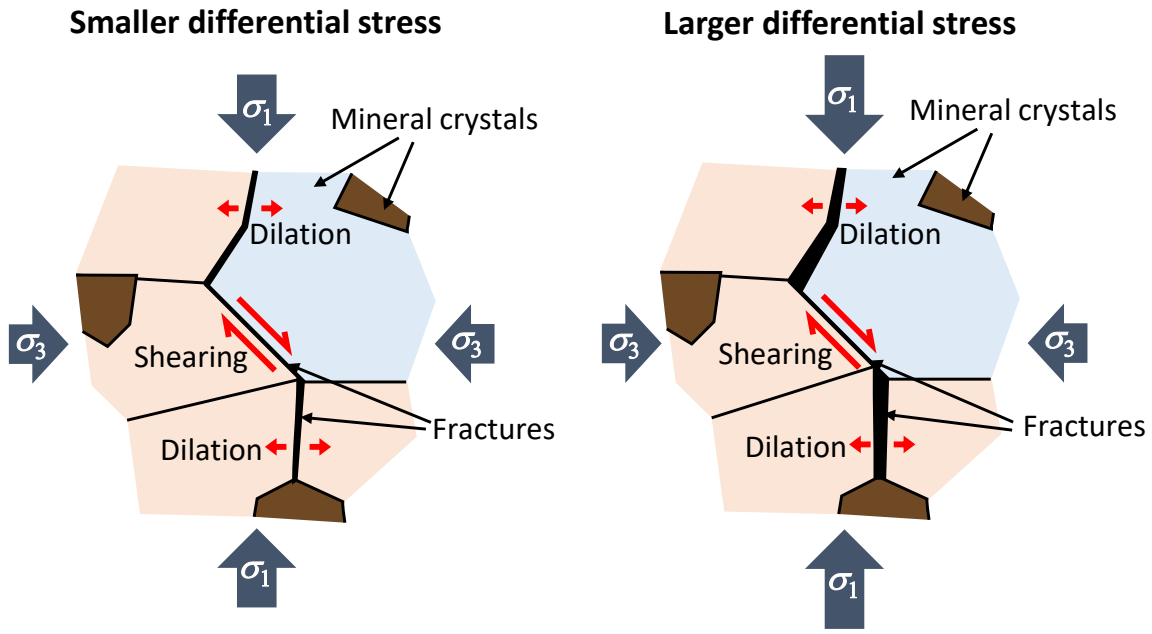

Figure 2.7. Illustration of the influence of differential-stress variation on fracture aperture. Larger differential stress induces larger fracture aperture in the cloud-fracture network

2.3.2. CO_2 Fracturing in Conventional Geothermal Conditions

Experiment 3 (200 °C; Figure 2.8) yielded qualitatively similar AE behavior and a breakdown pressure level to Experiment 1 (450 °C) performed at the same differential stress (50 MPa). The AE behavior and breakdown pressure level in Experiment 4 (200 °C, 65 MPa differential stress; Figure 2.9) were similar to the results from Experiment 2 (450 °C) performed with the same differential stress. Notably, the AE energy level in Experiment 4 was higher than that in other experiments, possibly a result of the fracturing of the lower-temperature rock having greater elasticity under larger differential stress (i.e., the shear stress within the rock) (Heuze, 1983; Goebel et al., 2013). The breakdown pressure was observed at 37 and 12 MPa in Experiments 3 and 4, respectively, based on the significant increase in AE energy, the latter of which was significantly lower than that predicted (Figure 2.5). The difference was thought to be the result of the variation in σ_t of the rock, as depicted in Eq. (2.1), where a small (e.g., 1 MPa) variation in σ_t causes an increasingly noticeable difference in breakdown pressure as the differential stress increases. Accordingly, a 12 MPa breakdown pressure corresponds to a σ_t of 6 MPa. A similar degree of difference was also observed in previous studies and was ultimately considered to significantly match the Griffith failure criterion. Therefore, Experiments 3 and 4 results similarly suggested that the Griffith failure criterion is applicable for CO_2 fracturing under conventional geothermal conditions.

X-ray CT images of the samples from Experiments 3 and 4 demonstrated the formation of complex fracture patterns, with more fractures appearing in Experiment 4 (approximately 6 fractures per cm^2) than in Experiment 3 (approximately 5 fractures per cm^2). Permeability of the Experiment 4 sample

demonstrated a 31-fold enhancement (from 2.0×10^{-18} to 6.2×10^{-17} m^2), which was greater than the 10-fold increase observed in Experiment 3 (from 2.1×10^{-18} to 2.1×10^{-17} m^2). Thus, the results suggested that the effects of differential stress on fracturing characteristics were similar in both conventional and superhot geothermal conditions (i.e., fracture aperture increased with differential stress). Nonetheless, the number of fractures appearing in the X-ray CT images from Experiments 3 and 4 was smaller (<50%) than those from experiments performed at 450 °C, similarly supporting that the fracture aperture decreased with decreasing temperature.

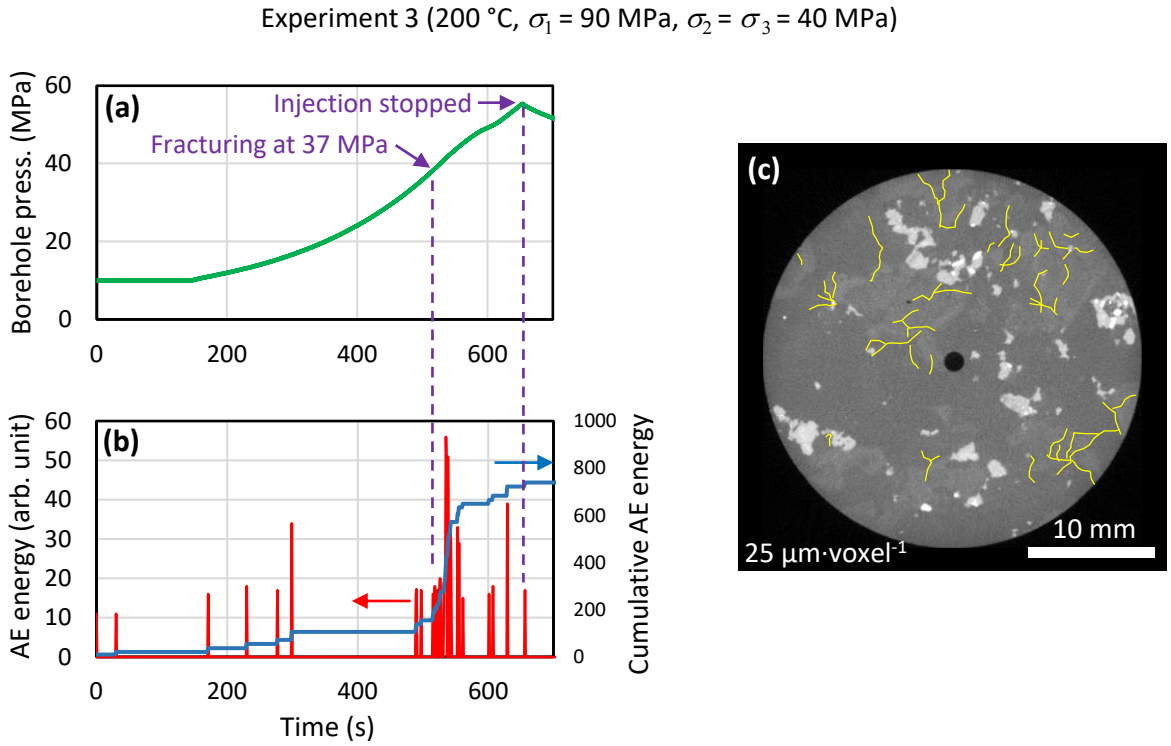

Figure 2.8. (a) Borehole pressure, (b) AE energy (red line) and cumulative AE energy (blue line) during Experiment 3, and (c) post-experimental X-ray CT image of the sample. Relatively small apertures are highlighted in yellow to increase gray scale visibility

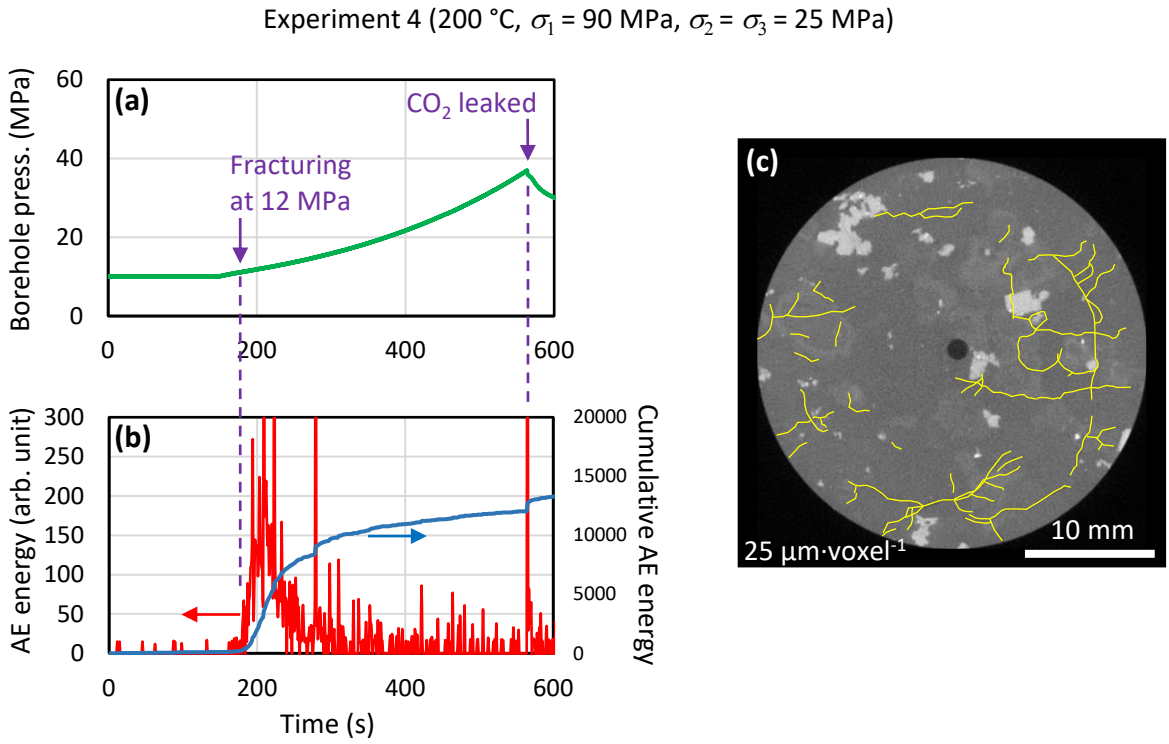

Figure 2.9. (a) Borehole pressure, (b) AE energy (red line) and cumulative AE energy (blue line) during Experiment 4, and (c) post-experimental X-ray CT image of the sample. Relatively small apertures are highlighted in yellow to increase gray scale visibility

Accordingly, Experiment 5 was performed at 300 °C and 50 MPa differential stress to evaluate the effects of temperature on fracturing characteristics. Figure 2.10 depicts that the borehole pressure and AE behavior were similar to those observed in Experiment 1 (450 °C) and 3 (200 °C), with the same differential stress. The breakdown pressure in Experiment 5 was determined to be 38 MPa, which was also close to that observed in the two experiments (Figure 2.5). The number of fractures appearing in the X-ray CT image was in between the number of fractures that appeared in Experiments 1 and 3 (approximately 8 fractures per cm^2). Additionally, a 13-fold permeability enhancement (from 2.6×10^{-18} to 3.3×10^{-17} m^2) occurred due to fracturing. Hence, the decrease in temperature reduced the number of visible (wide-aperture) fractures, although it remains obscure whether the actual number of fractures also decreased.

The temperature dependence of rock's mechanical properties is likely responsible for the observed changes in the fracture aperture. As explained in Section 2.3.1, shear deformation caused fracture dilation and provided some degree of preservation too; however, these deformations and the preservation must have been enhanced by high rock deformability and permanent deformation, respectively, during the experiments performed at high temperatures. It is vastly known that the mechanical properties of rocks, such as Young's modulus (Heuze, 1983; Gautam et al., 2018) and yield stress (Griggs et al., 1960 as cited in Jaeger et al., 2007), decrease with increasing temperature, resulting in higher rock deformability and increasing degrees of permanent deformation. This explanation also opens the possibility that the actual number of fractures is not positively correlated with temperature.

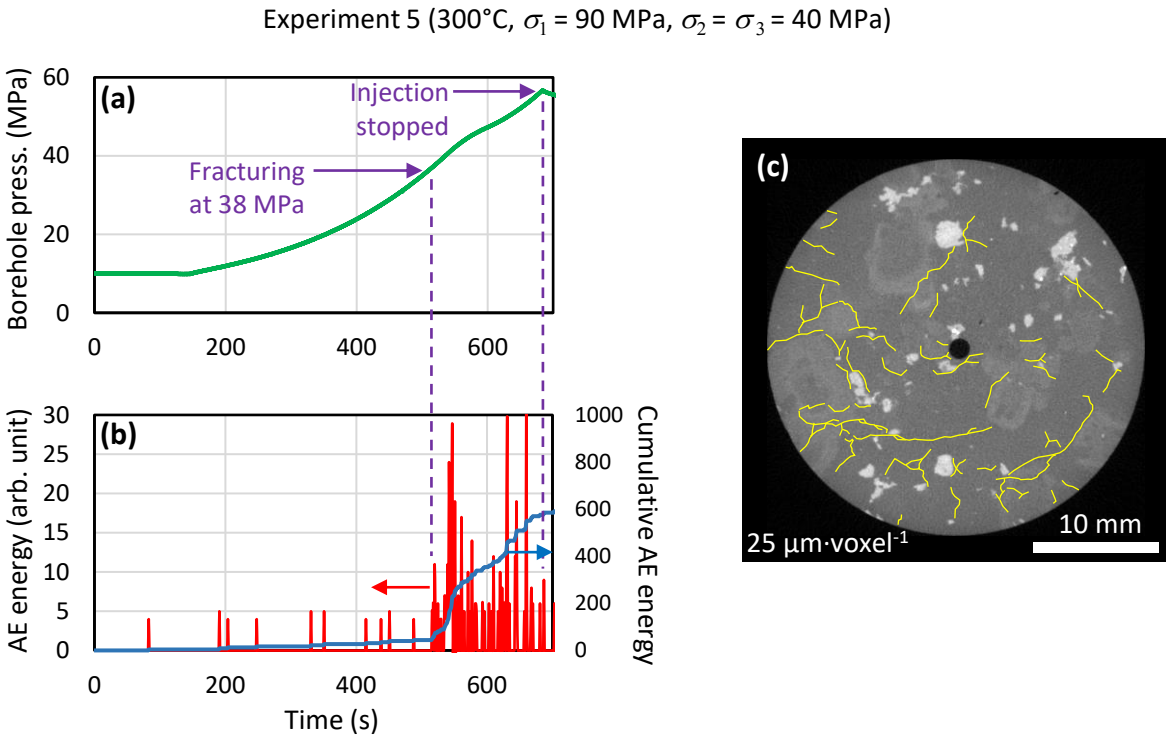

Figure 2.10. (a) Borehole pressure, (b) AE energy (red line) and cumulative AE energy (blue line) during Experiment 5, and (c) post-experimental X-ray CT image of the sample. Relatively small apertures are highlighted in yellow to increase gray scale visibility

Several differences from the results of this study can be observed in those of CO_2 fracturing in previous research. Fracturing resulted in several major radial fractures with many branches (Ishida et al., 2016; Isaka et al., 2019), whereas in this study, a higher number of shorter, wavy shaped fractures were formed (i.e., lacking distinct main fractures). Next, this study demonstrated an increase in fracture aperture with increasing temperature, whereas Isaka et al. (2019) reported a decrease in fracture density (directly translating to fracture aperture) with increasing temperature. These differences were ultimately attributed to the different stress states between the studies.

Experiments in both Ishida et al. (2016) and Isaka et al. (2019) were performed under a relatively low differential stress ($\leq$ 5 MPa), below four times the tensile strength of granite used in their respective studies. Referring to the Griffith failure criterion (Eq. (2.2)), a small differential stress results in fracturing with negligible shear deformation of the fractures. Additionally, Ishida et al. (2016) oriented the rift plane of granite parallel to the σ_1-σ_2 plane; thus, even though complex fracture patterns were formed, the fractures relaxed (i.e., closed) and maintained a narrow aperture. Conversely, the large differential stress values in this study allowed for effective shear deformation on the fractures; hence, the preservation of fracture dilation was observed at several locations.

The observation of opposing conclusions on the effects of temperature on fracture aperture can be attributed to the differences in differential stress. The major cause of fracture dilation in (Isaka et al., 2019) was tensile opening of the fractures oriented parallel and sub-parallel to σ_1, due to fluid pressure

inside the fractures. Hence, when the pressure dropped after the fracture formation in the high-temperature experiments, the fractures closed more easily at higher temperatures, and any permanent deformation did not enhance the preservation of dilation. In this study, fracture dilation was predominantly caused by the shear deformation of inclined fractures; thus, even when fluid pressure dropped, a certain degree of fracture dilation persisted from permanent deformation.

2.3.3. CO_2 Fracturing at a Large Scale and Realistic Stress Condition

To reveal the detailed characteristics of fracturing, a CO_2 fracturing experiment was performed at 300 °C under a true triaxial stress state (Experiment 6). Figure 2.11 depicts the changes in fluid pressure in the borehole and five production pipes, sample deformation for each principal stress direction, and AE energy throughout experimentation.

There was no significant deformation (<5 μm relative to the initial value), and AE energy was relatively low prior to a borehole pressure of 6 MPa. Several peaks in AE energy, depicted by green arrows in Figure 2.11c, were related to compressional waves produced by CO_2 as the stepwise pressure increased, whereas small peaks may have been caused by some deformation of pre-existing microfractures (Knill et al., 1968). Significant deformation started to occur, and the AE energy began to increase when the borehole pressure reached 6 MPa. Accordingly, 6 MPa was the observed breakdown pressure, lower than predicted (11.6 MPa for a σ_t of 7 MPa; Figure 2.5). Nevertheless, these differences can likely be explained by the variation in σ_t, (see discussion of Experiment 4 results).

At this borehole pressure (6 MPa), the deformation in the σ_3 direction demonstrated the largest positive change (dilation), followed by σ_2, while deformation in the σ_1 direction demonstrated negligible dilation. Additionally, AE energy remained high, while the borehole pressure was maintained. The continuous deformation and AE activity demonstrated that the fracturing process occurred gradually via flow-induced micro-fracturing (Watanabe et al., 2019; Goto et al., 2021).

The fluid pressure in the production pipes significantly increased even at bore hole pressures below the breakdown pressure. This response was quite different from the results of hydraulic fracturing on granite under superhot geothermal conditions (Watanabe et al., 2019; Goto et al., 2021) where a significant pressure increase in production pipes normally occurred after the breakdown point. This difference was apparently caused by the phase difference between water and CO_2 when they reached pressure transducers attached to the production pipes. Pressure transducers were located on the outside of the pistons, hence the fluid temperature dropped when reaching the transducers. Water turned into a liquid, and a longer time was required to fill and pressurize the production pipes, whereas CO_2 remained in the gaseous phase; hence, it could pressurize the production pipes faster. Owing to the fast increase, the pressure in the production pipes (i.e., sample surface) reached 4 MPa (equal to PE melt pressure), and therefore, borehole pressure was reduced before complete CFN formation, which would be indicated by a decrease in the AE energy (Goto et al., 2021).

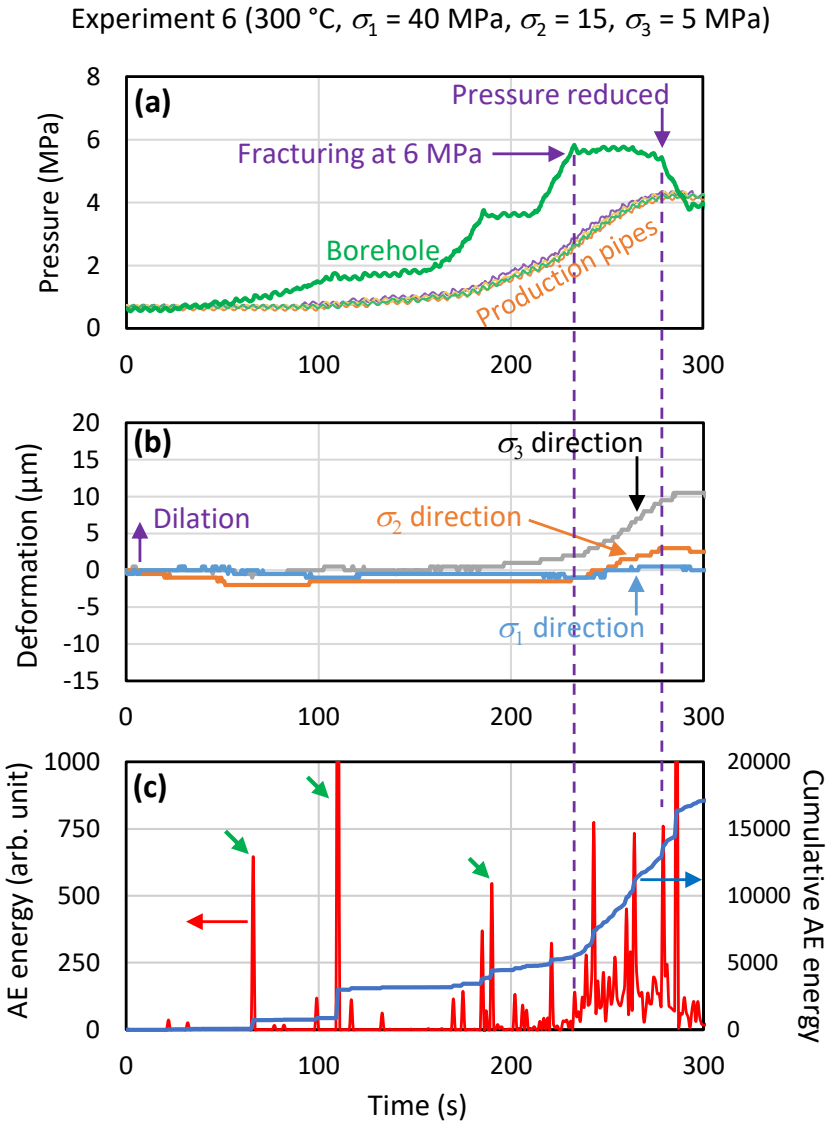

Figure 2.11. (a) Pressure at the borehole and five production pipes, (b) deformation of the sample for each principal stress direction, and (c) AE energy (red line) and cumulative AE energy (blue line) during Experiment 6. Note that there was no pressure change in one of the production pipes in the σ_3 direction due to setup error (the corresponding data is not shown)

The formation of a complex fracture pattern in the sample was first verified by P-wave velocity reduction (Watanabe et al., 2019; Goto et al., 2021). Table 2.3 summarizes the initial and final average P-wave velocities, and Figure 2.12 depicts the P-wave velocity distribution at all voxels pre- and post-experiment. The largest average reduction percentage was observed in the σ_3 direction (21.9%), while the σ_1 direction exhibited the lowest (11.4%) (Table 2.3). The average reduction percentages in this study were smaller than those in the hydrofracturing experiments performed at 400 and 450 °C (Watanabe et al., 2019; Goto et al., 2021), possibly related to a reduction in the number of wide-aperture fractures, as suggested above, and the incomplete CFN formation in the sample body. The resulting P-wave velocity distributions from the previous water fracturing experiments were relatively uniform

throughout the sample (Watanabe et al., 2019; Goto et al., 2021). Conversely, the present post-experimental distribution of P-wave velocities demonstrated some degree of heterogeneity, suggesting that the initial distribution of pre-existing microfractures still significantly affected the final distribution of induced microfractures.

Optical microphotographs of thin sample sections obtained in the σ_1-σ_3 plane post-experimentation and resin impregnation were taken under parallel polarized, cross-polarized, and UV light (Figure 2.13). The fractures are seen as dark lines under parallel-polarized light. Under cross-polarized light, some of those fractures crossed grain boundaries (i.e., intergranular fractures) and were likely induced fractures. The fractures appear as light blue lines under UV light, as they were infiltrated by the fluorescent resin. These microphotographs further verified the development of an interconnected CFN within the sample.

The microphotographs captured under UV light demonstrated that fractures with wider apertures (distinct, brighter light blue; Figure 2.13c) were mostly found in quartz (including those at grain boundaries), approximately 300–400 fractures per cm^2 in the highly fractured parts; whereas there were only approximately 20 wider fractures per cm^2 in feldspar minerals (including those at grain boundaries). Several of these wider fractures tend to be parallel and sub-parallel to σ_1. This finding appeared to be consistent with the P-wave velocity data, where the largest reduction percentage was observed in the σ_3 direction. Elastic waves travel slower when perpendicular to the discontinuity planes compared to parallel (Hsu and Schoenberg, 1993). Orientations of some wide fractures, however, still appear to be controlled by the orientation of the pre-existing microfractures; some wide fractures appeared almost perpendicular to the σ_1 direction. Meanwhile, fractures with thinner apertures (less contrasty, dimmer light blue lines under UV light) appeared in quartz, but more so in feldspar grains. These thin fractures also seemed to coincide with the cleavages in the feldspar grains. Alternatively, biotite crystals do not demonstrate clear evidence of fracturing, possibly because they are more ductile than quartz and feldspars.

Table 2.3. Pre- and post-experimentation average P-wave velocities, and the average velocity reductions in the three principal stress directions

Direction	P-wave velocity ($m \cdot s^{-1}$)		Decrease (%)
	Before fracturing	After fracturing	
σ_1 direction	3048.0	2700.9	11.4
σ_2 direction	3543.7	2883.6	18.6
σ_3 direction	3378.7	2638.0	21.9

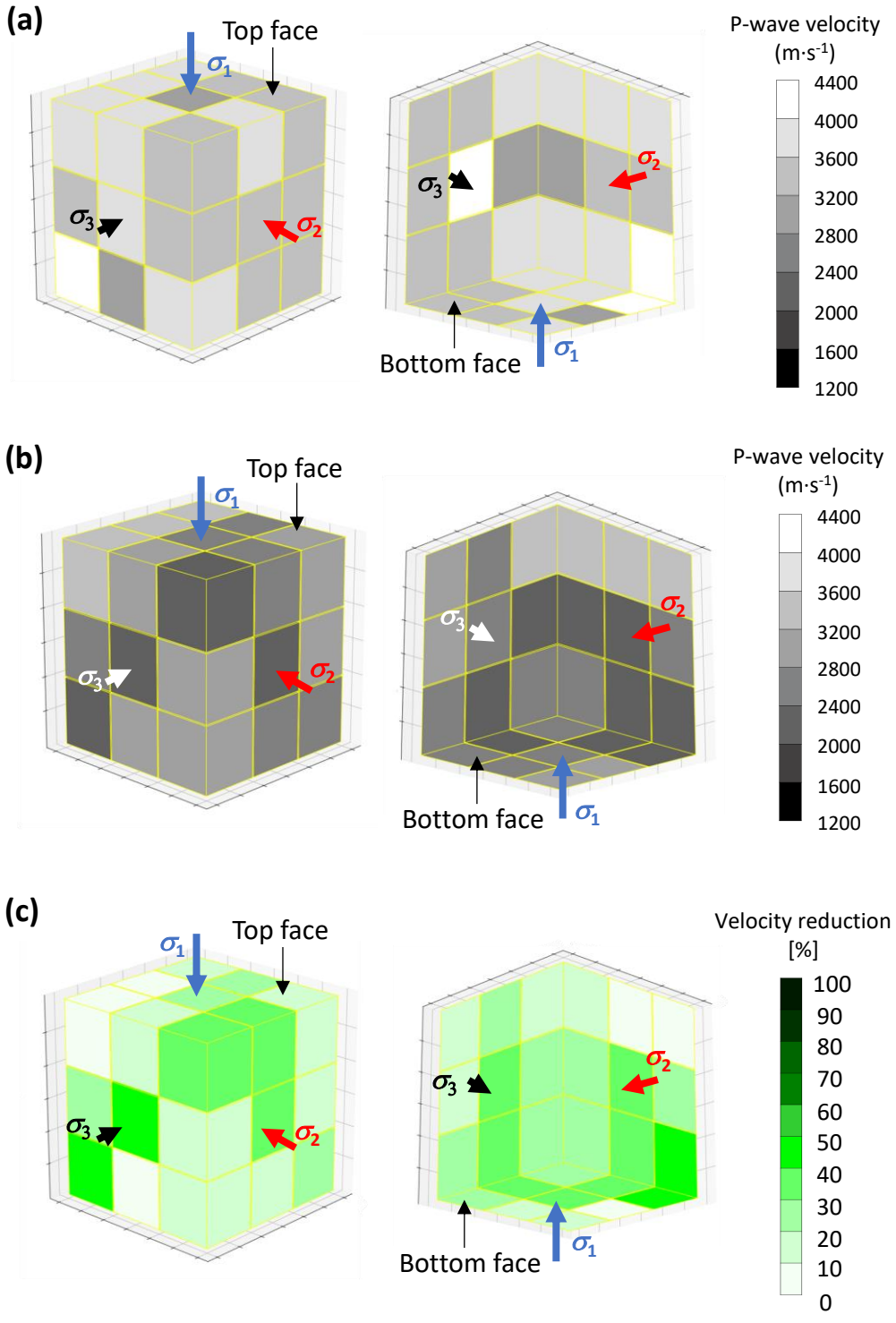

Figure 2.12. Distributions of estimated P-wave velocities for the sample (a) pre- (b) post-Experiment 6, and (c) the percentage of velocity reduction, where the left and right cubes, respectively, show each other's invisible faces

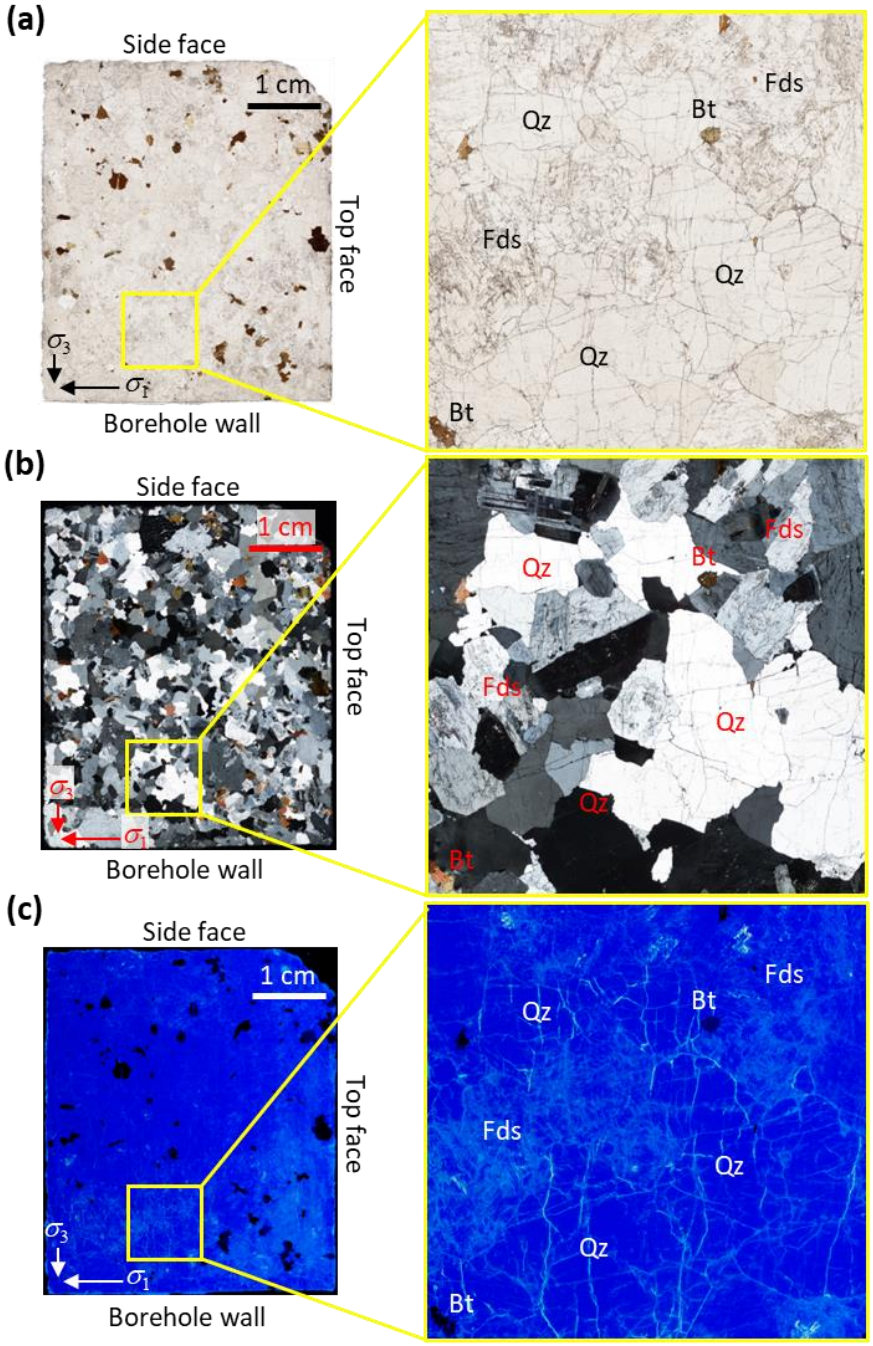

Figure 2.13. Optical microphotograph of a post-experiment, thin section of the σ_1-σ_3 plane using: (a) parallel polarization light, (b) cross polarization light, and (c) ultraviolet light. Bt, biotite; Fds, feldspars; Qz, quartz

This phenomenon marked the different responses of mineral types to stimulation of low-viscosity fluid and deformation, at least in the beginning of CFN formation, and simultaneously suggest that the actual number of induced fractures did not decrease with decreasing temperature. In minerals where cleavages were absent (e.g., quartz), stimulation and deformation were responded with a smaller number of fractures; thus, individual fractures exhibited larger deformation, and fractures oriented parallel or sub-parallel to σ_1 exhibited wider dilation. Alternatively, in minerals where cleavages were present (e.g.,

feldspars and biotite), stimulation and deformation were responded with a larger number of smaller fractures that coincided or originated from cleavages; thus, a smaller deformation occurred in each fracture. In special circumstances, wide dilation may occur in feldspars on the plane separating the two Carlsbad twins.

2.4. Implications for Enhanced Geothermal System

Previous studies (Watanabe et al., 2017b; Watanabe et al., 2019; Goto et al., 2021) have demonstrated the formation of a complex fracture pattern called a CFN at lower pressures (vs. conventional hydraulic fracturing) in granite by injecting water near and at its supercritical temperatures. Then, (Goto et al., 2021) also revealed the applicability of the Griffith failure criterion for CFN formation because the fracture network was formed through the stimulation of pre-existing microfractures by low-viscosity water.

Nevertheless, in addition to the challenges related to water reactivity and the environment, water utilization may face technical challenges in field-scale fracturing operations for superhot EGS development. First, (Goto et al., 2021) indicated that in a field-scale scenario, a high flow rate may be employed, possibly resulting in the temperature drop of water. In such cases, water viscosity would increase and CFNs could not be created. Next, Cladouhos et al. (2018) found that fracturing in superhot environments soon will likely be performed in open-hole intervals, owing to the lack of cements and casings capable of withstanding temperatures >350 °C. Furthermore, open-hole packers capable of operating at superhot temperatures are not yet available. In this case, even though it is possible to first cool down the open-hole interval and use the available high-temperature packers, water injection should also be performed at the lowest possible temperature, making CFNs difficult to achieve.

CO_2 injection provides potential solutions to the above scenarios because it maintains a low viscosity over a vast range of temperatures (Heidaryan et al., 2011). Thus, CFNs could still be achieved even if the fluid temperature dropped during injection. In instances where the borehole environment temperature should be kept low so it is possible to use available packers, CO_2 could be injected at low temperatures while still achieving a CFN. The same holds true for conventional geothermal environments, where CO_2 injection could produce a CFN, whereas water injection would normally result only in planar conventional hydraulic fracturing owing to its high viscosity. However, the feasibility of pressurizing CO_2 to form a CFN in a sufficiently large rock volume for an EGS reservoir remains obscure and should, therefore, be addressed in future studies. Additionally, future studies should address the potentially high risk of induced seismicity during low-temperature CO_2 injection in superhot geothermal environments due to the occurrence of thermal stress, which, alternatively, would be beneficial for fracturing.

Additionally, CO_2 fracturing may be highly advantageous in conventional geothermal environments where sizable natural fractures are present. It is conventionally believed that in the presence of natural fractures, the development of new induced fractures is less likely (Pine and Batchelor, 1984); therefore, hydroshearing of natural fractures has been the primary hydraulic stimulation mechanism (Rinaldi et al., 2015). However, numerous studies (Wallroth et al., 1999; Tester et al., 2006;

see also Law, 2011 and Kaieda 2015, as cited in Lu, 2018) have indicated poor hydraulic conductivity between injection and production wells, despite hydroshearing of the natural fractures. It is, thus, expected that a CFN will be formed via CO_2 injection, potentially increasing the probability of a strong hydraulic connection between the injection and production wells. However, there is concern about the difficulty to recover the fluid injected into a CFN from production wells as the fluid may flow in many directions in the CFN. This topic, along with the respective seismicity hazard, should be addressed in future studies.

The experiments in this chapter also revealed a challenge in CO_2 fracturing: narrow apertures in the resulting CFNs under conventional geothermal conditions. These CO_2-induced CFNs, especially those formed under low differential stress, also contributed to a decreased permeability enhancement compared to CFNs formed at superhot geothermal conditions. Alternatively, a chemical simulation work on granite at 100 °C reported that Na_2CO_3 dissolved SiO_2, primarily in quartz (Sarda, 1977, as cited in Portier et al., 2007). Furthermore, Rose et al. (2010) demonstrated silica and calcite minerals dissolution by injecting nitrilotriacetic acid, a chelating agent, in experiments performed at 150–300 °C. Therefore, it was expected that chemical stimulation will improve CO_2-injection fractured granite permeability under conventional geothermal conditions. This topic is discussed later in chapter 4.

2.5. Conclusions of this Chapter

Previous studies have demonstrated CFN formation in granite via water injection under superhot geothermal conditions and revealed the applicability of the Griffith failure criterion for governing the fracturing process; however, several challenges regarding its reactivity to rock-forming minerals and its environmental footprint hinder water utilization at field-scale operations. Among potential fracturing fluid alternatives, CO_2 demonstrates promise by overcoming the challenges posed by water and is potentially capable of creating CFNs under conventional and superhot geothermal conditions. Ultimately, CFN formation in granite via CO_2 injection had not yet been demonstrated.

The experimental-results presented in this chapter elucidated that CFNs can also be achieved in granite via CO_2 injection, for both superhot and conventional geothermal environments, through a set of fracturing experiments with AE monitoring performed at 200–450 °C under conventional and true triaxial stress states. The Griffith failure criterion was demonstrated to be applicable to CO_2 fracturing under these conditions. It was revealed that differential stress is an important factor in creating CFNs as it causes shear deformation and fracture dilation at multiple locations and creates an interconnected network of complex fractures. Mineral type was also found to affect the fracturing process, at least in the early stages.

The potential advantages of CO_2 fracturing include lower breakdown pressures (than those in conventional hydraulic fracturing) and induced fracturing (CFN formation) in the presence of pre-existing natural fractures under conventional geothermal conditions, whereas the challenge in CO_2 fracturing is thin fracture apertures at conventional geothermal conditions but may be solved through chemical stimulations. Future studies should address the topics for the extensive use of CO_2-based EGSs globally in the future.

Chapter 3 : Shearing and Fracturing in Naturally Fractured Environments

3.1. Introduction

As presented in the previous chapter, CO_2 injection can achieve cloud-fracture networks (CFNs) in granite at conventional and superhot geothermal conditions via the stimulation of pre-existing microfractures. The findings suggest that CO_2 injection could also induce CFN in the unfractured rock (matrix) of naturally fractured geothermal environments, i.e., environments with meter scale pre-existing fractures, as implied by Tester et al. (2006). The hypothesis was essential to be elucidated as the CFNs could potentially provide additional connections to the stimulated natural fractures. This chapter discusses experiments that were performed to elucidate the possibility and characteristics of CFN formation in naturally fractured conventional and superhot geothermal environments, along with the shearing-characteristics of the natural fractures due to CO_2 injection. A set of experiments was performed on cylindrical granite samples with sawcut inclined form the sample axis, without fluid injections at 200 and 450 °C, where the sawcut shear-slip was induced by increasing differential stress, to elucidate the friction coefficients of the sawcut and the shear-slip characteristics with respect to temperature difference. CO_2 injection experiments were performed on the samples of the same type at 200 and 450 °C to elucidate the possibility and characteristics of CFN formation in the rock matrix and the characteristics of the injection-induced shearing of the sawcut with respect to temperature variation. An experiment with water injection was performed to examine advantages and challenges of CO_2 injection in naturally fractured environments, as compared to water injection. A discussion was made on the potential implications of the present-experimental results for creating granitic-geothermal reservoirs in naturally fractured geothermal environments. The contents of this chapter have been published as Pramudyo et al. (2022).

3.2. Material and Methods

Experiments were performed on different 40-mm long and 30-mm diameter cylindrical Inada granite samples (Figure 3.1a), the same type of granite used in Chapter 2. A sawcut inclined at 45° from the axis of the sample was made in each sample using a diamond disk saw with 80-grit diamond particles to simulate the presence of a natural fracture. As the sawcut was not bordered by a fracture tip, the shear-displacement could be assumed to represent that in natural fractures. Fracture surface roughness is known to affect the hydro-mechanical behavior of a fracture during injection-induced shear slip (Ye and Ghassemi, 2018). To remove the effect of surface roughness, which was irrelevant in these experiments, samples containing sawcut with similar surface roughness were used for all experiments (Figure 3.1a). A 1.5-mm diameter borehole was then drilled parallel to the sample axis on each sample end face, intersecting the sawcut at a 10 mm depth (Figure 3.1a). The two boreholes allowed fluid to be injected into the sawcut and fluid production from the sawcut, including pressure measurements on each end side of the sample.

X-ray computed tomography (CT) scans were performed on each sample before and after the experiments to verify shear slip in the sawcut and observe CFN formation at the voxel scale rather than

obtaining an entire network image, which requires thin-section observation. The computed tomography (CT) scans were performed under dry, room temperature, and atmospheric pressure conditions, at an X-Ray tube voltage of 120 kV, a tube current of 150 μA, and a voxel size of 30 × 30 × 30 μm.

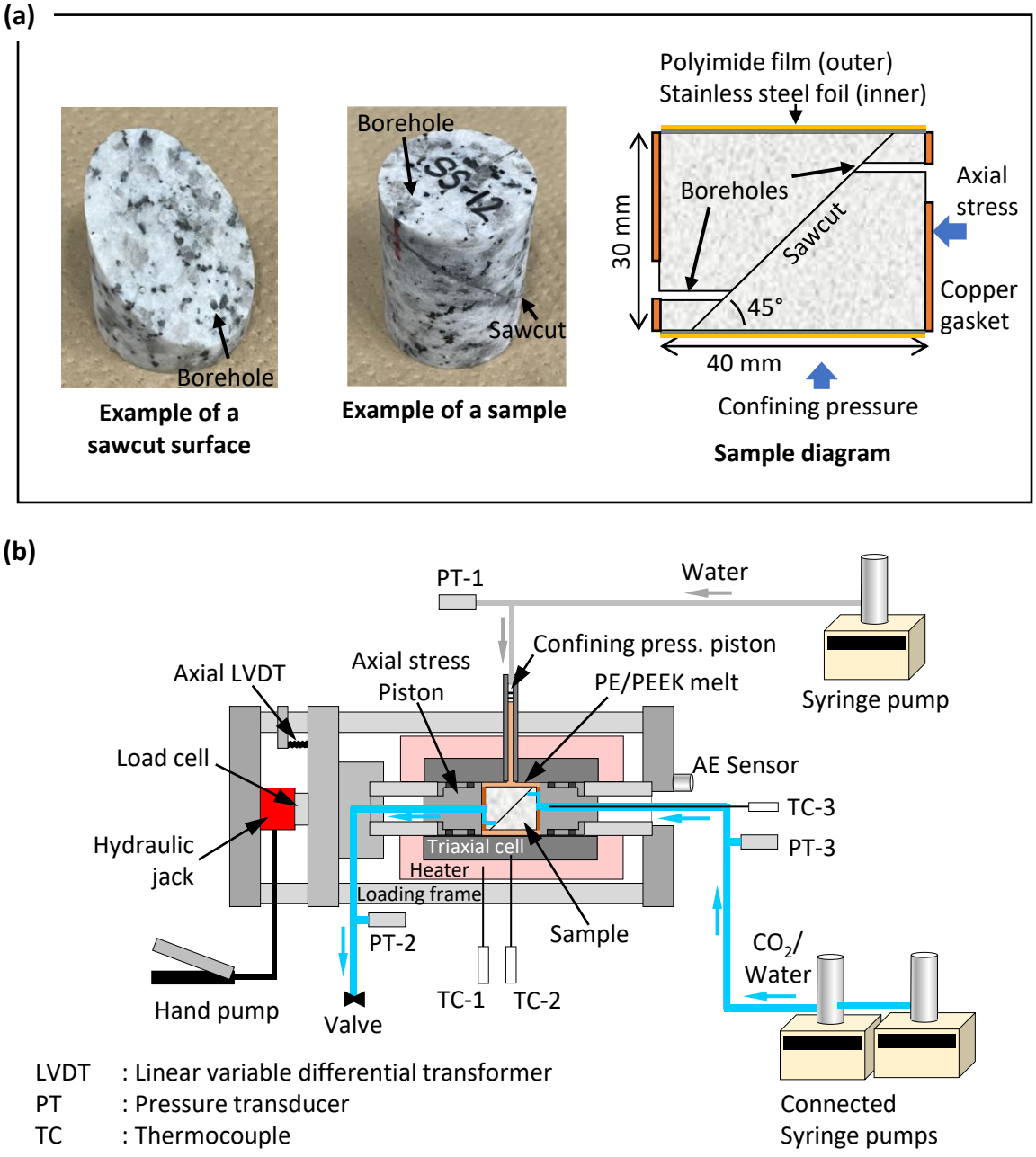

Figure 3.1. (a) Granite sample photographs and the diagram. A sample half shows an example of a sawcut surface. (b) Design of the injection-induced shear-slip experiment. Two connected syringe pumps were used to increase the pumping capacity during CO_2 injections

The experiments were performed using the conventional-triaxial stress experimental system, along with the AE measurement system (Figure 3.1b), which are described elaborately in Chapter 2. Herein, two cylindrical axial stress pistons equipped with a centered (axial) fluid flow-path and pipe at which

injected fluid is heated to the experimental temperature, and a syringe pump to control the confining pressure were used. A hand-pump operated hydraulic jack was used to induce the axial stress, wherein the exerted axial force is not controlled during experiments, allowing for axial-stress drop once deformation occurs in the sample. This strategy was inspired by Ye and Ghassemi (2018) and reasonably simulated stress relaxation due to fracturing or hydroshearing in a geothermal reservoir. Two connected syringe pumps were used to accommodate a large initial volume of gaseous CO_2, as the injection involved large-magnitude volumetric compression during the phase change from a gas to liquid at room temperature within the pump cylinders.

For the experiment, the chipped sawcut edges were first filled with fireproof putty, which has a low strength (thus not affecting the experimental results), to prevent molten-plastic intrusion into the sawcut during the experiment. The sample was then wrapped with a 10-μm-thick stainless-steel foil and with a 50-μm-thick polyimide film that did not melt during the experiments; both acted as sleeves. A copper gasket, with two joined circular holes connecting the centered flow-path of the piston and off-centered borehole, was placed between the end faces of the sample and piston. The wrapped sample was then placed inside a plastic (PE or PEEK) cylinder within the triaxial cell and subsequently heated in an electric furnace. During the heating process, a relatively small axial stress (c.a. 3 MPa) was maintained to prevent the PE or PEEK from flowing into the sample end faces on melting. Above the plastic melting temperature (approximately 120 °C for PE; 343 °C for PEEK), the confining pressure and axial stress were raised (carefully to prevent sawcut deformation) to the experimental stress state.

During CO_2 injection into a naturally fractured geothermal environments, stimulation of natural fractures and CFN formation are expected. The stimulation of natural fractures is commonly described using the Mohr–Coulomb (MC) failure criterion (Cox, 2010). Accordingly, the total normal (σ_n, MPa) and shear stress (τ, MPa) on a fracture are computed as follows:

$$\sigma_n = \left(\frac{\sigma_1+\sigma_3}{2}\right) - \left(\frac{\sigma_1-\sigma_3}{2}\right) cos2\theta_r \tag{3.1}$$

$$\tau = \left(\frac{\sigma_1-\sigma_3}{2}\right) sin2\theta_r \tag{3.2}$$

Fracture failure occurs as follows:

$$\tau = C + \mu_s(\sigma_n - P_p), \tag{3.3}$$

where σ_1 is maximum principal stress (MPa), σ_3 is minimum principal stress (MPa), C is the cohesive strength (MPa), μ_s is the coefficient of static friction of the fracture, P_p is the pore pressure (MPa), and θ_r is the angle between the fracture plane and σ_1 direction. Then, CFN formation in the rock matrix is expected at pressures in accordance to Griffith failure criterion [Eq. (2.1) and (2.2)] through the penetration and stimulation of pre-existing microfractures by the low-viscosity CO_2 (e.g., 49.4 μPa · s at

150 °C and 40 MPa, and 38.9 μPa · s at 450 °C and 40 MPa), as described in Chapter 2.

Table 3.1 lists the temperature, initial stress state, and type of experiments performed. To clarify the sawcut μ_s and shear-slip characteristics, two experiments were first performed at 450 °C (Experiment 1) and 150 °C (Experiment 2), both with an initial axial stress (corresponding to σ_1) and confining pressures (corresponding to the intermediate principal stress, σ_2, and σ_3) of 55 and 30 MPa, respectively. In these experiments, the differential stress was increased step-by-step; each step was maintained for approximately 120 s. The differential stress was increased until several dynamic shear slips were observed, as indicated by the axial shortening and AE activities.

Table 3.1. Experimental conditions

Experiment	Temp. (°C)	Initial stress (MPa)			Experiment type
		σ_1	σ_3	σ_1-σ_3	
Experiment 1	450	55	30	25	Increase of differential stress
Experiment 2	150	55	30	25	Increase of differential stress
Experiment 3	450	90	40	50	CO_2 injection
Experiment 4	150	90	40	50	CO_2 injection
Experiment 5	150	90	40	50	Water injection

In this study, the sawcut slip shear displacement (d_s, μm) and average shear velocity (v_s, μm · s^{-1}) were estimated from the axial deformation data using the following equations (3.4) and (3.5):

$$d_s \approx \frac{-d_x}{cos\theta_r}, \tag{3.4}$$

$$v_s = \frac{d_s}{t}, \tag{3.5}$$

where d_x is the slip-related axial deformation (μm) and t is the slip duration (s). Note that the axial deformation data should include rock matrix contraction or dilation (several micrometers, depending on the temperature, stress state, and state of the rock matrix); hence, the d_s and v_s values reported in this study are approximate values.

Ohnaka (1975) reported an average value of 0.59 for friction at the initiation of slip (i.e., μ_s) and 0.76 (i.e., coefficient of dynamic friction, μ_d) at a displacement of 1.8 mm for the ground surface of the Inada granite near room temperature, indicating a slip-hardening behavior. However, an average of 0.53 for μ_d at the ground surface of the Inada granite was obtained by Hirose et al. (2012), implying low μ_s values. Mitchell et al. (2013) reported an increase of c.a. 0.04 in μ_s from 150 to 450 °C in the ground surface of the Westerly granite; a similar magnitude of variation in μ_s also occurred among the samples at the same temperature. Therefore, a μ_s value of approximately 0.5 was expected in Experiments 1 and 2. Continuous (stable) sawcut slip was expected in the experiments as the differential stress increased,

considering the slip-hardening behavior (Cornet, 2016).

Experiments with CO_2 injection were first performed at 450 °C (Experiment 3) with initial axial stress and confining pressures of 90 and 40 MPa, respectively, to determine the possibility of CFN formation along with the shearing of the natural fractures in superhot geothermal environments with existing natural fractures. The initial stress state in this experiment was used in the experiments performed by Watanabe et al. (2017b) and some of the experiments in Goto et al. (2021) and Pramudyo et al. (2021), thus allowing comparisons of the characteristics of the resulting CFNs. This allows for the identification of the differences (advantages and challenges) with respect to the presence of natural fractures. CO_2 injection was initiated with a 30-ml $\cdot$ min^{-1} flow rate at room temperature until 8-MPa injection pressure, continuing with a 1-ml $\cdot$ min^{-1} rate to avoid a large acceleration in the pressure increase that could lead to unnecessary AE noises during the CO_2 phase change from gas to liquid at c.a. 7.3 MPa in cylinder of the pump. All fluid injections in this study were performed at relatively low flow rates to allow the injected fluid temperature to reach the experimental temperature before it arrived at the sample surface. The injected fluid temperature was measured using a thermocouple inside the injection pipe (TC-3, Figure 3.1). Preventing the injection of cold fluids was essential because it can significantly cool the fracture surface and result in the reduction of effective normal stress, thus promoting fracture slip (Bauer et al., 2016; Huang et al., 2019; Hu and Ghassemi, 2020).

The sawcut in this study was assumed to be cohesionless ($C = 0$ MPa). Therefore, dynamic shear slip was expected at a P_p value of approximately 15 MPa for μ_s of approximately 0.5 in Experiment 3 based on Eqs. (3.1)–(3.3). A pressure gradient was expected inside the sawcut, as CO_2 flowed from the injection to the production borehole through a narrow aperture sawcut, as observed by Ye and Ghassemi (2018). In this study, to simplify the computation, P_p was assumed to be the average between the injection and production pressure values, following Ye and Ghassemi (2018). The shear slip was also predicted to cause axial stress drops, increasing fracture formation pressure ($P_{p,frac}$) and causing a narrow aperture in the resulting CFN (Pramudyo et al., 2021). This was because the axial stress was applied using a hydraulic jack. Based on Eqs. (2.1) and (2.2), $P_{p,frac}$ in Experiment 3 was between 42.7 and 47 MPa for a tensile strength (σ_t) value of 7 MPa and a 10–20-MPa differential-stress drop (Goto et al., 2021; Pramudyo et al., 2021). In this chapter, the $P_{p,frac}$ values were taken from the injection borehole pressure, similar to Watanabe et al. (2017b), Watanabe et al. (2019), Goto et al. (2021), and Pramudyo et al. (2021). They considered the flow-induced micro-fracturing process (Goto et al. 2021), where CFN formation began and propagated from an area with sufficient pressure. CO_2 injection continued until the injection pressure reached 55 MPa to ensure CFN visibility in the X-ray CT observation. A pressure higher than the predicted $P_{p,frac}$ would increase the fracture aperture in the resulting CFN (Goto et al. 2021).

To determine the shear-slip characteristics of the natural fractures induced by CO_2 and water injection and to elucidate CFN formation possibility in naturally fractured rock in conventional geothermal environments, two experiments were performed at 150 °C: one with CO_2 injection (Experiment 4) and the other with water injection (Experiment 5). Both experiments were performed under an initial axial stress and confining pressures of 90 and 40 MPa, respectively. Experiment 4 used

the same injection method as Experiment 3. In Experiment 5, water was injected at 1 ml · min^{-1} because no phase change was expected within the pump cylinder during pressurization. Dynamic shear slip was predicted to occur at a P_p value of approximately 15 MPa in both experiments based on a μ_s value of c.a. 0.5 (Eqs. 3.1–3.3). Nonetheless, differences in the slip characteristics were expected because water has higher viscosities than CO_2 at this temperature (e.g., 184.8 μPa · s versus 22.3 μPa · s for CO_2 at 10 MPa). The CFN was only expected in Experiment 4 at $P_{p,frac}$ values from 42.7 to 47 MPa for a σ_t of 7 MPa (Eqs. 2.1 and 2.2).

3.3. Results and Discussion

3.3.1. Shear-slip at Conventional and Superhot Geothermal Conditions

Figure 3.2 depicts the time evolution of the stresses, axial deformation, and AE energy in Experiment 1. The dynamic slip of the sawcut initiated at a differential stress of 43 MPa, as indicated by large axial shortening, an AE energy peak (c.a. 5×10^2 arb. Units), and an increase in the cumulative AE energy. The dynamic slip corresponded to $\mu_s = 0.54$ (Eqs. 3.1–3.3), which was similar to the predicted value of c.a. 0.5. The dynamic slip appeared to occur continuously, as indicated by the continuous AE activity, with a v_s value of c.a. 3.9×10^{-1} μm · s^{-1} during the first second post initiation. The slip decelerated to a non-dynamic slip (e.g., v_s of approximately 5×10^{-3} μm · s^{-1} between an elapsed time of 650–700 s) when the differential stress was held constant in a step of differential stress. The next step of the increase in the differential stress raised the velocity again so that the slip velocity acceleration and deceleration occurred as the differential stress was increased stepwise. This behavior suggests an approximately 0.08 increase in μ_s for each increase in the differential stress, which is also supported by the ratio of shear to effective normal stress on the sawcut (Figure 3.2b).

Slip hardening, where $\mu_d > \mu_s$ and μ_d increases as slip progresses, has been proposed due to an increase in the actual contact area of the fracture by slip-induced flattening of the fracture surfaces (asperity degradation) (Byerlee, 1970; Biegel et al., 1992). Visual observation of the sawcut surfaces post-experimentation in this, and all subsequent experiments, generally revealed the presence of wear materials as evidence of slip-induced flattening of sawcut surfaces. This implies that slip behavior may be altered after several millimeters of displacement because wear materials built up within the fracture, as suggested by Byerlee (1967).

Figure 3.3 depicts the time evolution of the stresses, axial deformation, and AE energy from Experiment 2. Here, small axial shortening (approximately 8 μm) with sparse and low-energy AE activity (< c.a. 60 arb. Units) were initially observed as the differential stress was increased to 30 and 35 MPa, possibly due to non-dynamic slip in the sawcut. The sawcut dynamic slip initiated when the differential stress reached 39 MPa, as indicated by a large axial shortening (correlating to a d_s of approximately 33.3 μm) within 0.5 s (v_s of approximately 66.7 μm · s^{-1}) and an AE energy peak with a magnitude of two orders higher (c.a. 4.7×10^4 arb. Unit) than that in Experiment 1 at the initiation, which corresponds to a μ_s of 0.48. The dynamic slip decelerated to a non-dynamic slip when the differential stress was held constant at a step. The observed μ_s value, although slightly lower, agreed with the predicted value of 0.5. The μ_s value in this experiment was also slightly lower than that in Experiment

1, which was likely caused by a higher Young's modulus (i.e., lower deformability of sawcut asperities, where the stresses were concentrated), resulting in a smaller contact area within the sawcut at this temperature (Mitchell et al., 2013) as compared to that at 450 °C. The same factor also appeared to cause the higher velocities and AE energies during the dynamic slip at this temperature than those at 450 °C. Other dynamic slips with similar characteristics to the first slip (v_s of approximately 86–138.8 $\mu m \cdot s^{-1}$) were then observed when the differential stress was increased to 42 and 50 MPa, corresponding to μ_s values of 0.54 and 0.68, respectively.

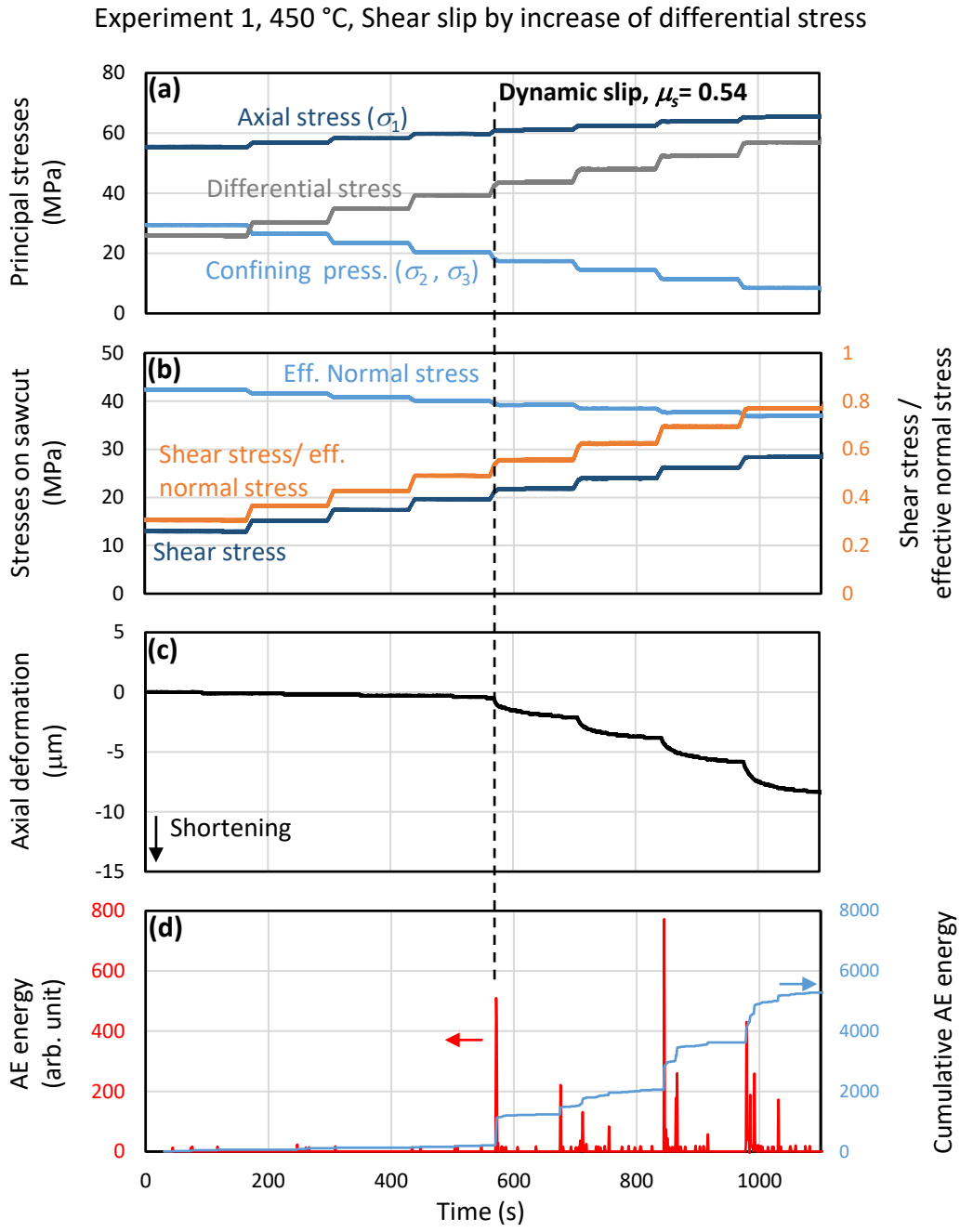

Figure 3.2. (a) Principal stresses, (b) stresses on sawcut, (c) axial deformation, and (d) AE energy (red line) and cumulative AE energy (blue line) during Experiment 1

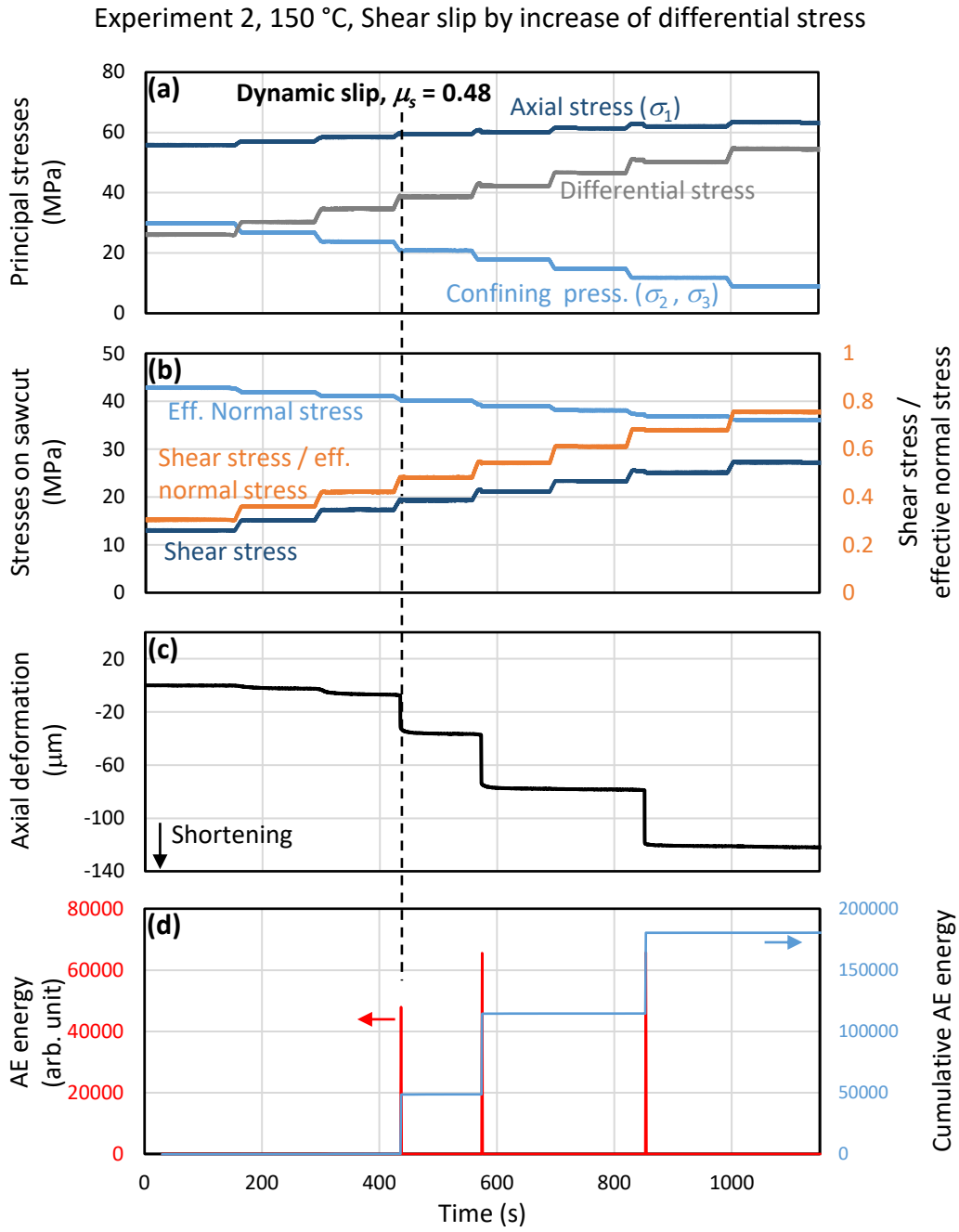

Figure 3.3. (a) Principal stresses, (b) stresses on sawcut, (c) axial deformation, and (d) AE energy (red line) and cumulative AE energy (blue line) during Experiment 2

Although slip hardening was observed in Experiments 1 and 2, significant differences in the dynamic-slip characteristics were observed. In Experiment 1, sawcut dynamic slip occurred continuously with velocities of approximately 10^{-1} μm · s^{-1}. Meanwhile, in Experiment 2, dynamic slips occurred within approximately 1 s with 10^{1}–10^{2} μm · s^{-1} velocities. Therefore, the dynamic-slip characteristics in Experiment 1 were called continuous slow slip, whereas the dynamic slips observed in Experiment 2 were called rapid slips. These results may imply that the shearing of natural fractures in superhot geothermal conditions could yield smaller displacements than shearing under conventional

geothermal conditions, assuming the same stress state.

3.3.2. CO_2 Injection in Naturally Fractured Geothermal Environments

Figure 3.4 depicts the stresses, pressures, axial deformation, and AE energy against time during Experiment 3. In the beginning, low energy (approximately 10 arb. units) AE activity and negligible axial deformation occurred, possibly due to non-dynamic slips within the sawcut (Ye and Ghassemi, 2020). Small increase in aperture (which were unmeasurable by the axial LVDT) likely occurred in the sawcut due to the pressurized CO_2, as indicated by acceleration in the increase of production pressure and deceleration in the increase of injection pressure at an elapsed time of approximately 1700 s. The small increase in aperture resulted in a smaller differential pressure between the injection and production sides, and subsequently a more homogeneous reduction in effective normal stress on the sawcut, allowing for a rapid slip at $P_p = 29$ MPa (time *T1*, Figure 3.4), with a v_s of approximately 24 $\mu m \cdot s^{-1}$ and AE activity (energy of approximately 4×10^2 arb. Unit). The slip velocities and energies of the AE activities decreased as it progressed.

Stress state on the sawcut at rapid-slip initiation corresponded to a μ_s of 0.69, which was higher than expected. Nonetheless, this was due to large heterogeneity in the sawcut-effective normal stress before the rapid slip. The sawcut dynamic slip resulted in cumulative differential-stress drop of approximately 7 MPa at $P_p = 55$ MPa. The changes in the sawcut permeability could not be determined experimentally in this study. Nonetheless, permeability could increase in natural fractures due to dynamic shear slip (e.g., Tester et al., 2006; Ghassemi, 2012; Ye and Ghassemi, 2018).

A continuous AE activity with an increasing energy (maximum of c.a. 2×10^2 arb. Unit) was then observed, starting at an injection pressure of 43 MPa (time *T2*, Figure 3.4), indicative of CFN formation. Additionally, there was a slight increase in the axial shortening rate at 43-MPa injection pressure, likely due to axial contraction in the rock matrix with gradual CFN formation. Hence, 43 MPa was considered the fracture pressure, which is similar to that predicted by Eq. (2.1) for the corresponding differential stress, with $\sigma_t = 7$ MPa. Post-experimentation X-ray CT images (Figure 3.5a) verified sawcut shearing, with the amount of deformation on the same (10^2-μm) order as that derived from the LVDT data. The CT images also revealed a CFN, which was inferred to contain narrower fractures (i.e., less contrasty, and comprised approximately 3 visible fractures per cm^2, or 70% less visible fractures per cm^2) than those formed at 450 °C and the same initial stress state reported by Pramudyo et al. (2021). This may have been the result of decreasing differential stress during CFN formation, as demonstrated by Goto et al. (2021) and Pramudyo et al. (2021). The general processes occurring in the sample from the beginning of CO_2 injection until CFN formation are illustrated in Figure 3.6.

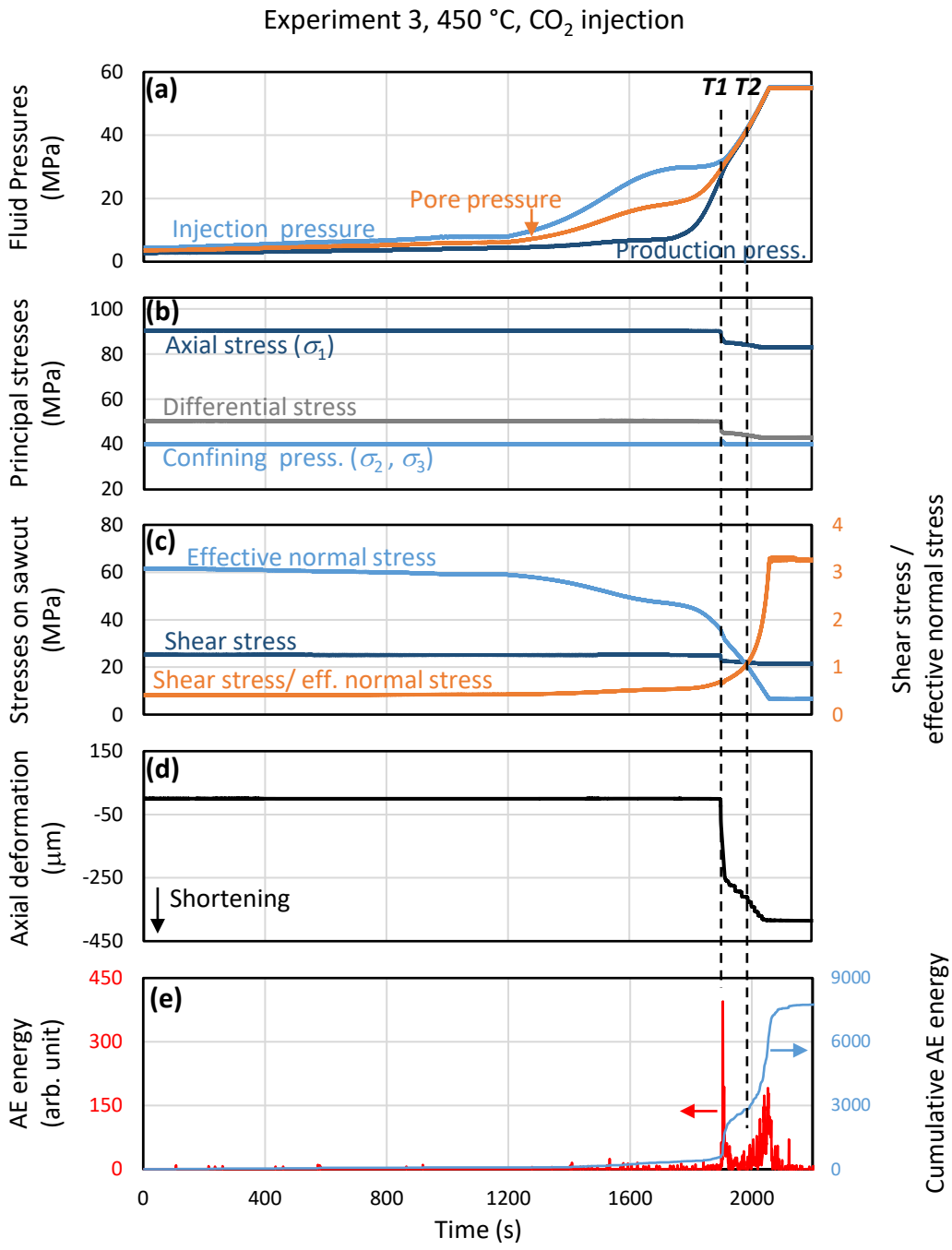

Figure 3.4. (a) Fluid pressures, (b) principal stresses, (c) stresses on sawcut, (d) axial deformation, and (e) AE energy (red line) and cumulative AE energy (blue line) during Experiment 3. *T1*: dynamic slip, *T2*: initiation of CFN formation

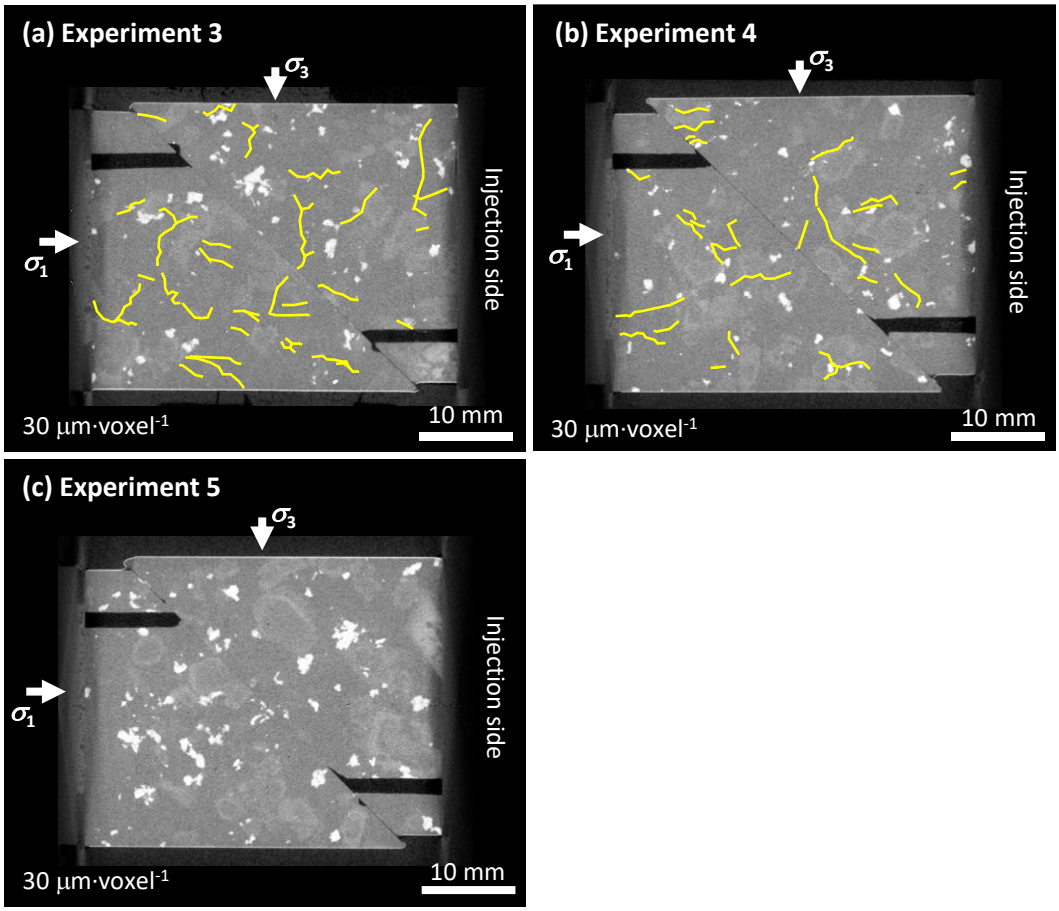

Figure 3.5. X-Ray CT of the sample post-experimentation (a) Experiment 3, (b) Experiment 4, (c) Experiment 5. Fractures are highlighted in yellow to increase gray-scale visibility. Cloud-fracture networks were induced only in Experiment 3 and 4 by CO_2 injection

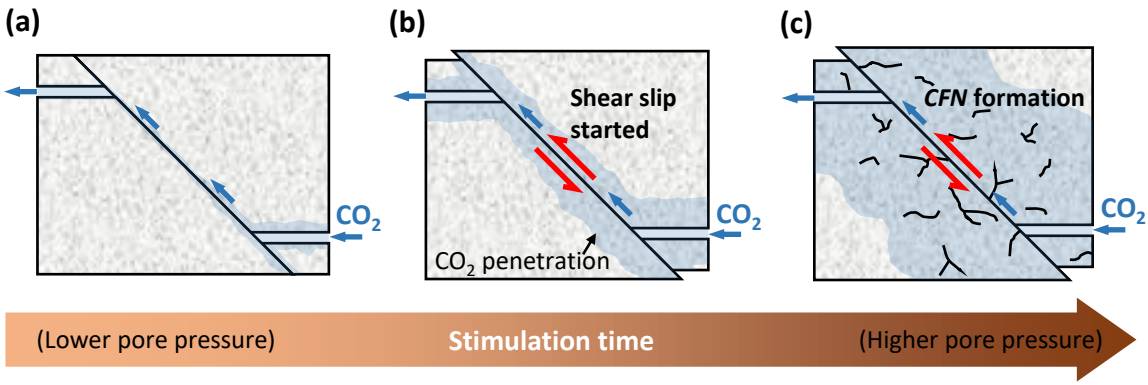

Figure 3.6. Illustration of processes in experiments with CO_2 injection: (a) beginning of CO_2 injection, (b) sawcut dynamic shear-slip occurs when the pore pressure satisfies Coulomb failure criterion, and (c) CFN started to form when the pore pressure satisfies Griffith failure criterion

Figure 3.7 depicts the time evolution of the pressures, stresses, axial deformation, and AE energy in Experiment 4. As the injection pressure increased, sparse and low energy (< 50 arb. units) AE activity occurred without significant axial shortening, likely due to non-dynamic sawcut slips. Subsequent

sawcut deformation was characterized by multiple rapid slips (v_s of approximately 36–88 μm · s^{-1}), which gradually turned into a mostly continuous slow slip. The rapid slips first started at P_p = 14.9 MPa (time *T1*), which corresponds to μ_s = 0.5. Each rapid slip was accompanied by high energy (up to approximately 6.6×10^4 arb. units) AE activity. The continuous slow slip started at P_p of approximately 40 MPa and generated continuous AE activity with energies of approximately 50 arbitrary units. Relatively small (< 10 MPa) differential pressures were observed throughout the injection, which likely caused the multiple rapid slips. Cumulative differential-stress drop of approximately 12 MPa was observed at a P_p of 55 MPa due to the dynamic shear slip.

The higher Young's modulus of the rock in this Experiment 4 likely suppressed the normal deformation of sawcut asperities, causing slightly wider apertures within the sawcut throughout the injection experiment compared to those at 450 °C and leading to relatively small differential pressures most of the time. Furthermore, the relatively constant differential pressure also suggested that the CO_2 pressure-induced increase in the sawcut aperture was negligible. Ultimately, the amount of sawcut shear displacement in this experiment was larger than that observed in Experiment 3 within the same interval of increasing injection pressure. This implies that the injection-induced shearing of natural fractures could produce a larger shear displacement under conventional geothermal conditions than that under superhot geothermal conditions.

The CFNs formed at an injection pressure of 43 MPa (time *T2*, Figure 3.7), following the onset of an increase in the AE energy (0.5 to 3×10^2 arb. unit) during the continuous slip. Additionally, there was an increase in the axial shortening rate, likely due to both contraction in the rock matrix during CFN formation and the temporal acceleration of sawcut shear slip due to injection-production pressure homogenization. Post-experimentation X-ray CT images (Figure 3.5b) verified CFN formation, including shear displacement of the sawcut with the amount of deformation on the same order as that revealed by the LVDT data. The X-ray CT images suggested that the CFN had narrow aperture fractures (less contrasty, and comprise approximately 2 – 3 visible fractures per cm^2, or about 10% less visible fractures than those in Experiment 3), likely due to formation at both low temperatures and differential stresses (Pramudyo et al., 2021) as a result of ineffective shear deformation of microfractures in the presence of the continuously sliding sawcut.

Figure 3.8 depicts the time evolution of the stresses, pressures, axial deformation, and AE energy in Experiment 5. The high viscosity of water at this temperature (e.g., 184.8 μPa · s versus 22.3 μPa · s of CO_2, at 10 MPa) caused a large pressure gradient within the sawcut; parts of the sawcut near the injection borehole rapidly approached the slip condition. This situation apparently led to a continuous slow slip that started at a P_p of approximately 17 MPa, yielding a μ_s of 0.51 [Eqs. (3.1)–(3.3)]. However, as suggested by the results of Experiment 3, the computed μ_s value could be inaccurate in an experiment with large differential pressure. The continuous slip only generated AE activity with an energy of 20–80 arbitrary units and caused a cumulative differential-stress drop of approximately 5 MPa as injection pressure reached 55 MPa. These results elucidate that under conventional geothermal conditions, water injection was less effective at inducing shear slip, especially with a large displacement, on natural fractures compared with CO_2 injection. X-ray CT images of the sample from Experiment 5 (Figure 3.5c)

verified the sawcut shear slip, with an amount of deformation of the same order as that of the LVDT data; as expected, no CFN was observed.

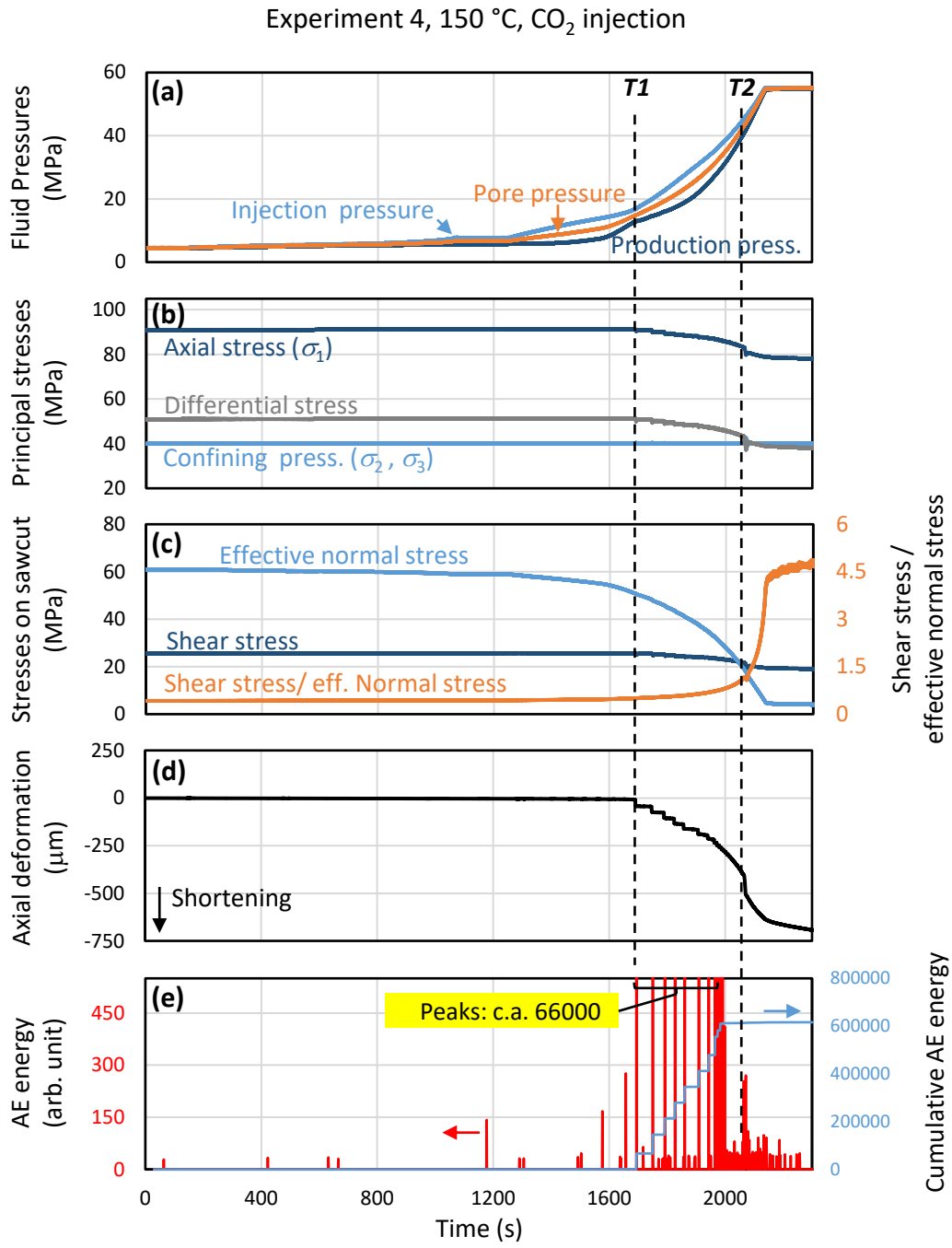

Figure 3.7. (a) Fluid pressures, (b) principal stresses, (c) stresses on sawcut, (d) axial deformation, and (e) AE energy (red line) and cumulative AE energy (blue line) during Experiment 4. Vertical scale for AE energy is limited to 550 to emphasize the AE activity produced by CFN formation. *T1*: dynamic slip, *T2*: initiation of CFN formation

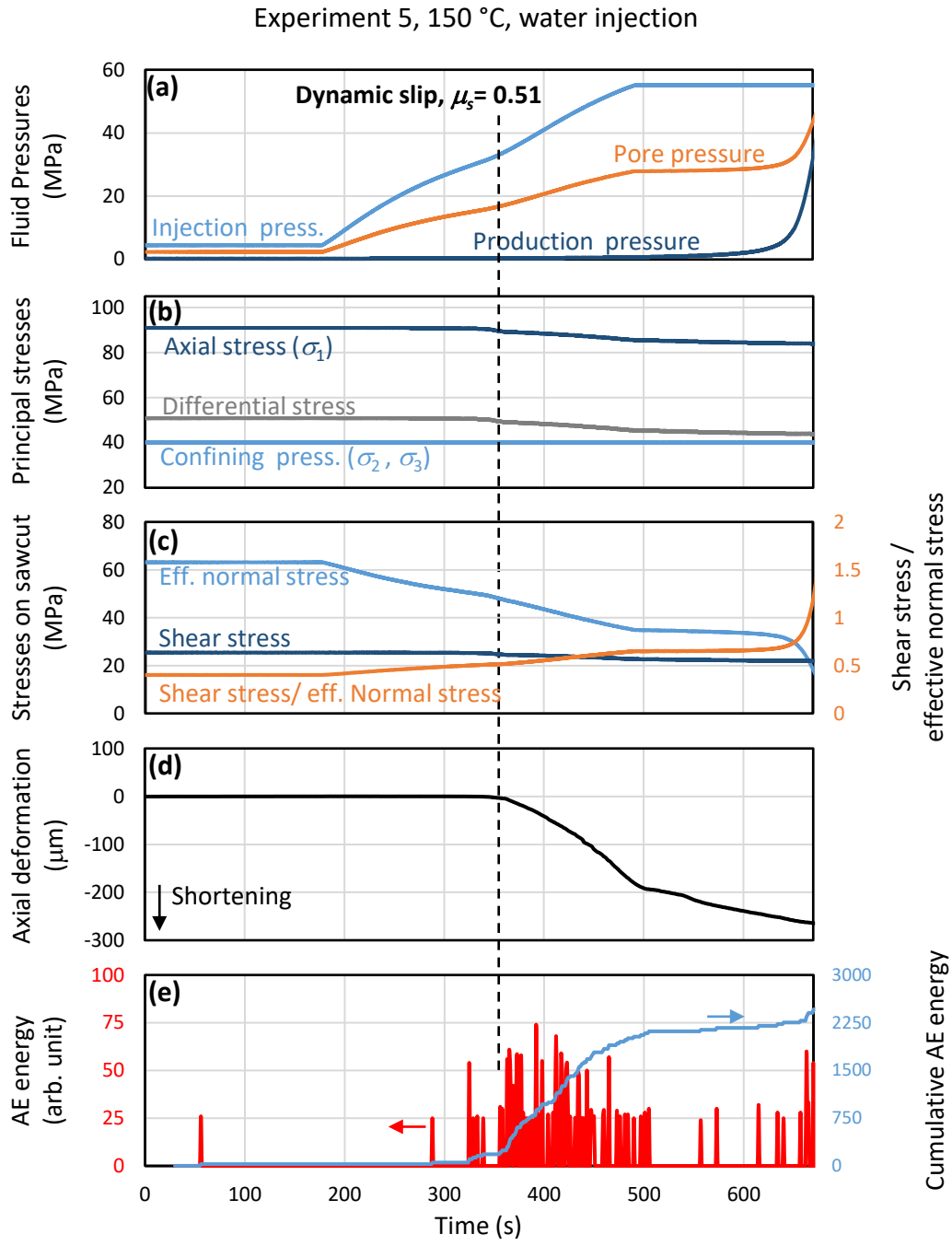

Figure 3.8. (a) Fluid pressures, (b) principal stresses, (c) stresses on sawcut, (d) axial deformation, and (e) AE energy (red line) and cumulative AE energy (blue line) during Experiment 5

3.4. Implication for Enhanced Geothermal System Development

The permeability enhancement and thermal extraction of an EGS in naturally fractured geothermal environments are predominantly dependent on stimulated natural fractures (Pine and Batchelor, 1984; Batchelor, 1986; Rinaldi et al., 2015); therefore, environments with closely spaced natural fractures are preferable (Tester et al., 2006). Nevertheless, previous studies have reported poor connectivity between the injection and production wells in networks of natural fractures stimulated by water injections (e.g., Wallroth et al., 1999; Tester et al., 2006; Lu, 2018).

The experimental results in this chapter suggest that the injection of lower viscosity CO_2 into naturally fractured rock, assuming the absence of faults, could be more advantageous than water injection. Under conventional geothermal conditions, CO_2 injection was experimentally shown to produce a larger shear displacement on a larger fracture surface area, which potentially leads to a higher fracture permeability based on the association between the magnitude of the induced micro-earthquake and permeability enhancement (Ishibashi et al., 2016). Moreover, the injection of low-viscosity CO_2 may require a lower injection pressure to stimulate the same volume of reservoir compared to that when using water. Under superhot geothermal conditions, CO_2 is advantageous over water for being capable of maintaining low viscosities and inducing large shear displacement (i.e., in the event of an injection-temperature drop or when the injection borehole must be maintained as cool as possible for engineering reasons). The formation of a CO_2 injection-induced CFN within naturally fractured geothermal environments, of which the possibility was elucidated in this study, would also be beneficial at EGS sites where natural fractures are sparse; the numerous permeable microfractures within the CFN could provide additional connecting flow paths between the natural fractures and thus potentially contribute to permeability enhancement (Ye and Ghassemi, 2019). These hypotheses require elucidation in future research.

Nevertheless, CO_2 injection in a naturally fractured geothermal environment presents challenges, as revealed by the experimental results of this study. Excessive dynamic shear slip on natural fractures could also impair fracture permeability due to wear-material built up, as implied by Byerlee (1967). The resulting fractures within the CFN have narrow apertures in both conventional and superhot geothermal environments, reducing their potential to provide additional connections for the natural fractures. Therefore, further stimulation, such as a long pressurization duration (Goto et al. 2021) or the use of chemical stimulation to dissolve rock-forming minerals at conventional geothermal temperatures (Watanabe et al., 2021b), may improve CFN permeability. The low CO_2 viscosity may also impose challenges during field-scale operation: CO_2 could flow far within the natural fracture network, especially under conventional geothermal conditions, such that increasing the pressure is difficult. These points require further elucidation in future studies.

3.5. Conclusions of this Chapter

The experiments elucidated that CO_2 injection into granite with natural fractures under conventional and superhot geothermal conditions potentially results in CFN formation, along with the shearing of the natural fractures.

The author first elucidated that the higher deformability of the rock (owing to a lower Young's modulus) at 450 °C increased the actual contact area between the microscopically rough sawcut surfaces, leading to a slight increase in the coefficient of static friction (μ_s) and lower dynamic-slip velocities compared to those at 150 °C. CO_2 injection produced small increase in sawcut aperture in the experiment performed at 450 °C, allowing for faster slip velocities once dynamic slip progressed, as compared to that without a pressurized fluid. Nonetheless, CO_2 injection did not increase the sawcut aperture at 150 °C, which could be attributed to the high Young's modulus at this temperature; instead, it caused

multiple rapid slips and an even larger shear displacement than the dynamic shear slip without fluid injection and those in the experiments performed at 450 °C. This may imply that the amount of injection-induced dynamic shear slip in natural fractures under superhot geothermal conditions is more restricted than that under conventional geothermal conditions.

Based on the existing studies, experiments performed at 150 °C implied that CO_2 injection potentially produce a large magnitude permeability enhancement within the stimulated natural fractures under conventional geothermal conditions; it induced a larger shear displacement over a larger fracture area, owing to lower CO_2 viscosity under these conditions, as compared to water. Moreover, lower CO_2 viscosity potentially allows for the stimulation of the same volume of rock as water at lower injection pressures.

The dynamic sawcut shear slip caused a differential-stress drop during injection in this study, increasing the formation pressure of the CFNs, following the Griffith failure criterion. The resulting CFNs also had narrower apertures than those formed in intact rocks under the same or similar initial conditions owing to the decreasing differential stress during formation and perhaps the less effective shear deformation within the microfractures in the presence of pre-existing fractures. Therefore, further stimulation methods, such as a high and long pressurization duration or chemical stimulation in conventional geothermal environments, could be considered. Additionally, low-viscosity CO_2 may flow far from the borehole in field-scale operations, such that pressurizing the reservoir becomes difficult; hence, further considerations are required.

Chapter 4 : Creating Geothermal Reservoirs by CO_2 Injection and Chemical Stimulation

4.1. Introduction

Experiments discussed in the previous chapters suggested that CO_2 injection-induced cloud-fracture network (CFNs) comprise narrow fractures for those formed at conventional geothermal temperatures, at small-differential stress conditions, and in the presence of pre-existing fractures. Goto et al. (2021) suggested that fracture aperture in the CFN can be improved via longer duration pressurization at pressures higher than the CFN-formation pressure. Nonetheless, alternative additional stimulation through chelating agent injection at conventional geothermal conditions was considered to reduce the risk of large induced seismicity.

Watanabe et al. (2021b) suggested and demonstrated permeability enhancement using injection of *N*, *N*-bis(carboxymethyl)-L-glutamic acid (GLDA), a chelating agent, for EGS-application because previous studies had suggested that GLDA is readily biodegradable (Pinto et al. 2014) and relatively stable up to approximately 200 °C (Sokhanvarian et al., 2016). It was demonstrated in flow-through experiments using GLDA solutions at pH 4 (weakly acidic), continuous permeability enhancement occurred through void formations due to selective dissolution of biotite, in fractured granite sample at 200 °C and a hydrostatic stress state (Watanabe et al., 2021b). Takahashi et al. (2023) later clarified that under the same condition, the highest permeability-enhancement factor was achieved at pH 4. Accordingly, this was not only due to void formation but also due to the formation of preferential flow-paths connecting the voids through dissolution of minerals other than biotite. Meanwhile, optimal-permeability enhancement was achieved by subsequent injection at pH 4 and 8, whereas at pH 8 (i.e., weakly alkaline condition), quartz dissolution dominated under a slow dissolution-rate of other minerals. Nevertheless, permeability enhancement process under differential stress, at which the fractures have the potential to deform and affect the permeability enhancement process, was yet to be elucidated. Moreover, the permeability-enhancement characteristics under radial-flow geometry and in large rock body was also necessary to be elucidated.

In this chapter, the author discussed experimental results on permeability enhancement process using GLDA solutions in CO_2 injection-induced CFNs, considering the effect of differential stress. Experiments under conventional-triaxial stress conditions were performed to demonstrate the effect of differential-stress variation to the permeability enhancement characteristics by chelating agent injection at weakly acidic and alkaline conditions. An experiment was also performed on a large cubic granite sample subjected to a true-triaxial stress condition to elucidate the permeability-enhancement characteristics under radial-flow geometry on a large rock body using successive GLDA solution injection at pH 4 and 8 (which was suggested for optimum permeability enhancement). A discussion on possible schemes to create granitic-geothermal reservoir via CO_2 injection and the additional stimulation methods was then made based on experimental results in Chapter 2 – 4 and some literature reviews.

4.2. Material and Methods

4.2.1. Experiments under Conventional Triaxial Stress States

Experiments were performed on cylindrical Inada granite (diameter, 30 mm; length, 25 mm) with a single borehole (diameter, 1.5 mm; length, 10 mm), the same type of granite and geometry to those used in Chapter 2 for experiments under conventional triaxial stress conditions. Inada granite, by volume, comprises 33.7% quartz (ideal chemical formula: SiO_2), 32.1% K-feldspar (ideal chemical formula: $kAlSi_3O_8$), 30.3% plagioclase-feldspars (chemical formula for each end-member: $NaAlSi_3O_8$ and $CaAl_2Si_2O_8$), 3.8% biotite (ideal chemical formula: $K(Mg,Fe)_3AlSi_3O_{10}(OH,F)_2$), and 0.1% other minerals (Ishihara, 1991; Sasada, 1991; Takahashi et al., 2011; Takaya, 2011).

The experiments would comprise CO_2 fracturing and chelating-agent flow-through experiments on the fractured samples. Therefore, X-ray computed tomography (CT) scan was performed on the samples before CO_2 fracturing, after CO_2 fracturing, and after chelating-agent flow-through experiments. The X-ray CT was performed under atmospheric pressure and temperature of c.a. 23 °C, at an X-ray tube voltage of 120 kV, a tube current of 150 μA, and a voxel size of 16.6 μm to verify the formation of CFNs and mineral dissolutions. Additionally, porosity of the samples post-experimentation was estimated from the X-ray CT data using Molcer Plus 3D image visualization and processing software (White Rabbit Corporation) to provide insight into mainly the degree of void formations in the experiments. The porosity was defined as the sum volume of voids larger than 27 voxels (i.e., visible voids) divided by bulk volume of rock.

The chelating agent solutions were prepared from a 40 wt% aqueous solution of GLDA-Na_4 ($C_9H_9nNa_4O_8$), purchased from Tokyo Chemical Industry Co., Ltd. Wang, et al. (2022) computed the molar concentration of the GLDA-Na_4 in this initial solution to be approximately 1.3 $mol \cdot L^{-1}$. Dilutions were prepared to make 20-wt% GLDA-Na_4 solutions, where the pH was adjusted to 4 or 8 by incorporating nitric acid accordingly. These solutions were the same as those used in Watanabe et al. (2021b) and Takahashi et al. (2023); as the studies demonstrated, the GLDA solutions are more viscous than water. At 5 MPa and 200 °C, the GLDA solution viscosity at pH 4 and 8 are 304.2 and 286.6 $\mu Pa \cdot s$, respectively. The higher viscosities implied that the GLDA solution penetration and the mineral dissolution would occur effectively only in certain wider fractures within CFNs. Thus, under differential stress condition, significant rock deformation may not be promoted even at considerable pore pressure; significant deformations would be likely in the injection of low-viscosity CO_2 (<100 $\mu Pa \cdot s$).

The experiments were performed using the conventional triaxial-stress experimental and AE measurement system (Figure 4.1), as described in Chapter 2 and 3. For CO_2 fracturing, the sample and the experimental system were configured the same as those in Section 2.1.1. Meanwhile for the later chelating-agent flow-through experiment, the fractured sample was sleeved using stainless-steel foil (10-μm thick) and polyimide film (50-μm thick). Copper gaskets with centered hole were placed on the sample end-faces; the gasket on the injection side also contained concentric and radial grooves to channel the produced fluid to production pipe. In both CO_2 fracturing and chelating agent flow-through experiments, the sleeved sample was placed in a polyethylene (PE) cylinder inside the triaxial cell and subsequently heated to the experimental temperature. Axial stress (corresponds to maximum principal

stress, σ_1) and confining pressure (corresponds to both intermediate, σ_2, and minimum principal stress, σ_3) were raised once the sample reached the experimental temperature.

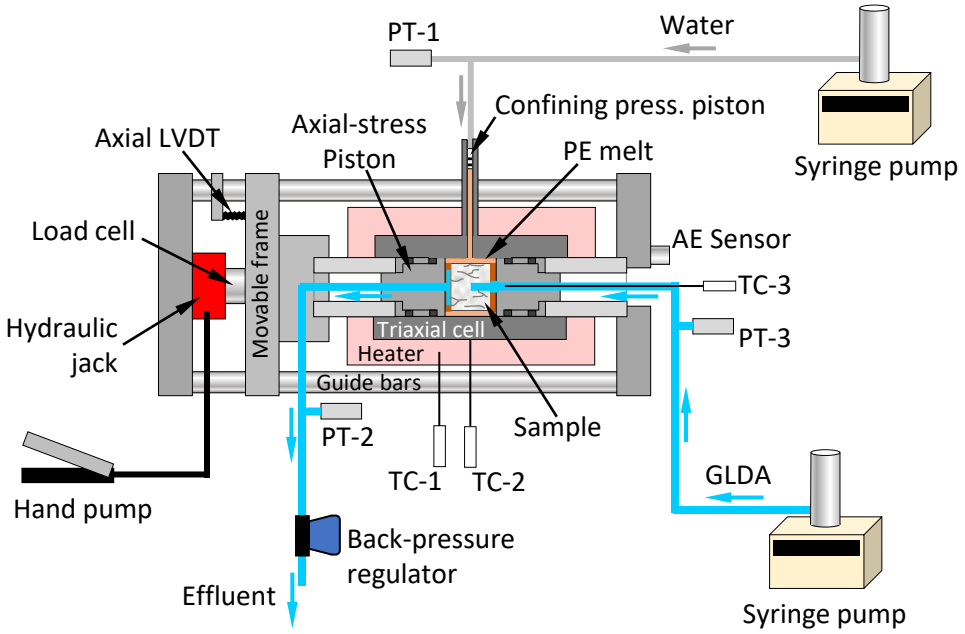

LVDT : Linear variable differential transformer
PT : Pressure transducer
TC : Thermocouple

Figure 4.1. Design for the chelating agent-flow through experiments under conventional-triaxial stress conditions

To elucidate the permeability enhancement process by CO_2 fracturing and injection of a weakly acidic chelating agent under a variation of differential stress, two experimental runs (Run 1 and Run 2) were performed at 200 °C (Table 4.1). In Run 1, CO_2 fracturing was performed first at axial stress and confining pressure of 70 and 30 MPa, respectively (i.e., differential stress = 40 MPa); then, under the same stress state and temperature, chelating agent flow through was performed. In Run 2, CO_2 fracturing and the later flow-through experiment were performed at an axial stress and confining pressure of 100 and 30 MPa, respectively (i.e., differential stress = 70 MPa). To elucidate the permeability enhancement process by CO_2 fracturing and injection of a weakly alkaline chelating agent under a differential stress condition, an experimental run (Run 3) was performed at 200 °C and axial stress and differential pressure of 100 and 30 MPa, respectively (i.e., differential stress = 70 MPa).

CO_2 fracturing was performed using the same injection-strategy to that in Chapter 2 for experiments under conventional triaxial-stress state; CO_2 was injected at a constant flow rate of 1 ml $\cdot$ min^{-1} at room temperature, using a syringe pump, from an initial borehole pressure of 10 MPa. To increase CFN visibility in the post CO_2 fracturing X-ray CT measurement based on the flow-induced micro-fracturing process (Goto et al., 2021), CO_2 injection pressure was increased to 30 MPa in Run 1 and 3 and increased to 45 MPa in Run 2. Those maximum pressures were higher than the expected values of fracture

formation pressure ($P_{p,frac}$; 21.25 MPa for Run 1 and 3; 35.7 MPa for Run 2), based on Griffith failure criterion with tensile strength (σ_t) of 7 MPa [Eqs. (2.1) and (2.2)].

Table 4.1. Conditions for CO_2 fracturing and chelating agent-flow through experiments

Run	Experiment type	pH of GLDA	Temp. (°C)	Stress state			
				σ_1	σ_2	σ_3	$\sigma_1-\sigma_3$
Run 1	CO_2 fracturing, then GLDA injection	4	200	70	30	30	40
Run 2	CO_2 fracturing, then GLDA injection	4	200	100	30	30	70
Run 3	CO_2 fracturing, then GLDA injection	8	200	100	30	30	70
Run 4	GLDA inj. on thermally frac. sample	4, then 8	200	45	20	10	35

Meanwhile, in chelating agent flow-through experiments, GLDA solution was first injected from both injection and production sides at a constant pressure of 26 MPa for approximately 20 min to saturate the sample with the GLDA solution. The procedure was performed to avoid GLDA-solution evaporation in the sample that otherwise would occur if the solution was injected from one side. The injection and production pressures were then set to 28 and 26 MPa, respectively, and maintained constant for 5 h, during which GLDA solution flowed in the sample. The injection and production pressures were close to the confining pressure value to optimize GLDA solution penetration into the CFN. Nonetheless, those pressures were lower than the maximum injection-pressure values during CO_2 fracturing to prevent fracture propagation due to increase in pore-pressure.

Permeability values of the sample were not obtained during these experiments because the flow-geometry in the sample would have been the combination of first radial flow from borehole and then the flow towards the production surface of the sample. The combined flow-geometries would make permeability computations too complex for the objective of the experiments. Nonetheless, the permeability-changes in the sample could be assessed by changes in injection-flow rates, based on Darcy's law. All effluent from each experiment were collected to be analyzed for the concentrations of elements eluted from the minerals: aluminum (Al), calcium (Ca), iron (Fe), potassium (K), magnesium (Mg), and silicon (Si). The analysis was performed using inductively coupled plasma optical emission spectrometry (ICP-OES).

4.2.2. Experiment under True Triaxial Stress State

An experiment under true-triaxial stress state (Run 4, Table 4.1) was performed to elucidate permeability enhancement process by GLDA solution injection on a large scale and under radial flow geometry. It was performed on a 100 × 100 × 100 mm cubic Inada granite, which had been thermally treated at 500 °C and atmospheric pressure for 10 h to induce a dense network of microfractures. The thermally induced network of microfractures is analogous to cloud-fracture network (Goto et al., 2023). The sample also contained a centered borehole (diameter = 10 mm), connecting two opposite faces of the sample. P-wave velocity measurements were performed on the sample before and after the experiment to determine the distribution of voids post the experiment.

The experiment was performed using the true-triaxial stress experimental system (Watanabe et al. 2019), which is described in more detail in Section 2.1.2. Herein, the sample was placed inside the triaxial cell for the borehole to be positioned vertically. Two pistons with centered fluid-flow path were positioned at the top and the bottom of the sample and provided the maximum principal stress (σ_1). Fluid-flow path in the bottom piston was connected to a syringe pump for fluid injection into sample's borehole; the flow-path in the top-position was connected to a closed pipe. The thermocouple in the top flow-path was extended to measure the temperature at the center of the sample.

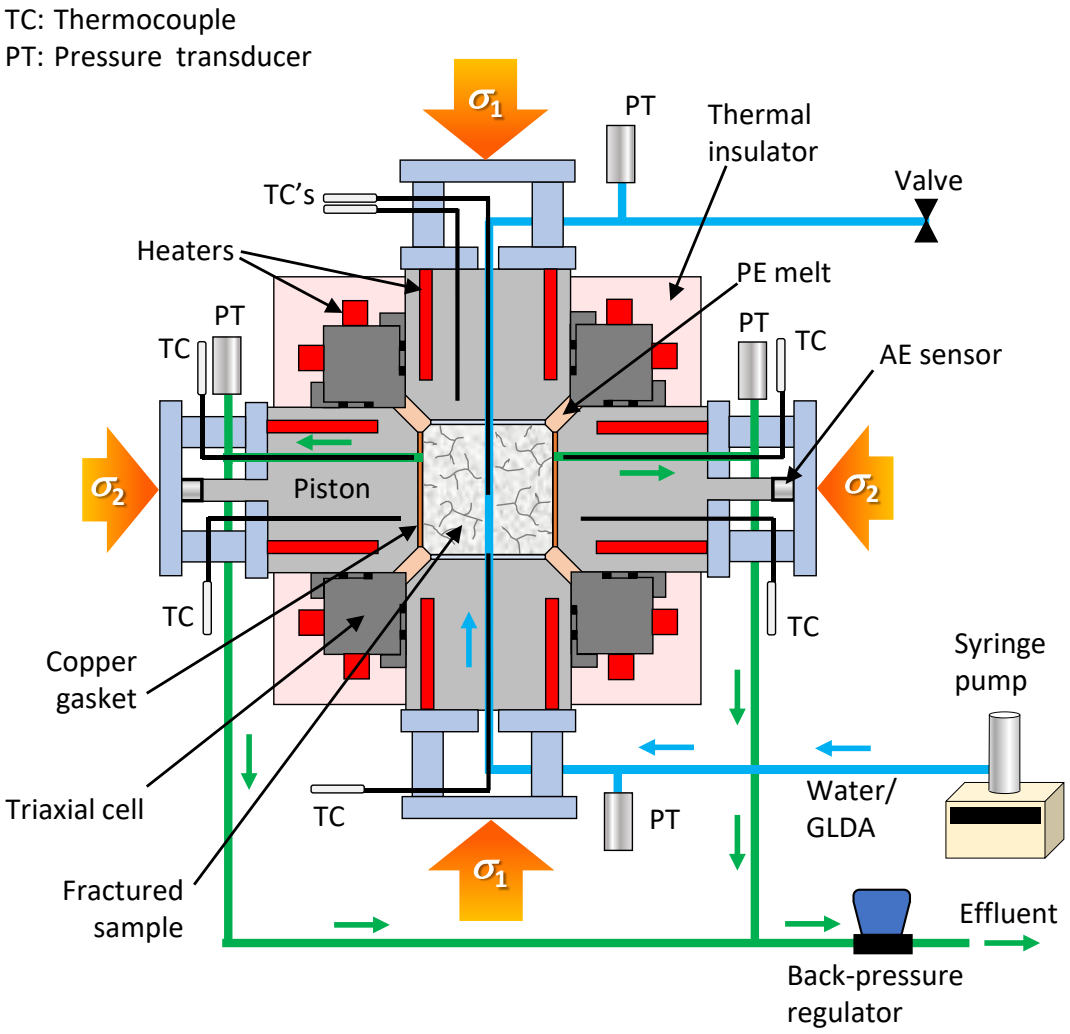

Figure 4.2. Design of the chelating agent flow through experiment at under true-triaxial stress condition

Fluid injections were performed at 200 °C, σ_1 = 45 MPa, σ_2 = 20 MPa, σ_3 = 10 MPa, and production pressure (pressure at sample side faces) = 2 MPa. At first, water was injected into the borehole at 1 ml · min^{-1} to determine AE energy level and deformation rates under negligible chemical reaction condition in the sample (i.e. background condition). GLDA solution at pH 4 was then injected for 2 h, followed

by GLDA solution injection at pH 8 for another 2 h, both using 1-ml · min^{-1} flow rate. In this experiment, the flow of GLDA solution in the sample could be assumed to be a radial flow from the centered borehole. Therefore, permeability changes in the sample could be estimated using the following equations (adapted from Dake, 1983):

$$P_b - P_s = \frac{q\mu}{2\pi hk} ln \frac{r_s}{r_b} \ , \tag{4.1}$$

$$P_b - P_s = \frac{q\mu}{2\pi hk_1} ln \frac{r_1}{r_b} + \frac{q\mu}{2\pi hk_2} ln \frac{r_s}{r_1} \ , \tag{4.2}$$

where P_b is borehole pressure (Pa), P_s is production pressure (Pa), q is flow rate (m^3 · s^{-1}), μ is dynamic viscosity of fluid (Pa · s), r_b is borehole radius (m), r_s is sample radius (in this case, distance from the center to the side face of the sample, expressed in meter), h is the borehole length (m), k is sample average permeability (m^2), k_1 is permeability (m^2) of the zone near the borehole within the radius r_1 (m), and k_2 is permeability (m^2) of the zone between r_1 and r_s. Based on Eq. (4.1), enhancement in the average permeability of the sample would be reflected by a decrease in the differential pressure, if constant flow rate was used.

The produced fluid (effluent) was collected, once during the water injection, and then in 10-min interval from the start of GLDA injection to be later analyzed using ICP-OES. The analysis would provide the evolution of Al, Ca, Fe, K, Mg, and Si concentrations in the effluent, thus providing insights into the mineral dissolution process in the sample. X-ray CT imaging was performed on cores (length: 50 mm, diameter: 25 mm) obtained from the sample post-experimentation to verify the distribution of mineral dissolutions with respect to distance from borehole. Three cores were obtained parallel to the borehole (i.e., σ_1 direction) from around the borehole and from near the sample side faces at centered $\sigma_1 - \sigma_2$ and $\sigma_1 - \sigma_3$ planes. X-ray CT scan was performed under atmospheric conditions at an X-ray tube voltage of 120 kV, tube current of 150 μA, and voxel size of 10 μm. Porosity estimation using Molcer Plus software was also performed based on the X-ray CT data to provide additional insight into the degree of mineral dissolution around the borehole versus near sample side faces.

4.3. Results and Discussion

4.3.1. Influence of Differential Stress on Permeability Enhancement

Figure 4.3–4.5 depict the results of CO_2 fracturing in Run 1, 2, and 3, respectively. The results were generally consistent with the discussion in Chapter 2. CFN formation occurred at 30 MPa in Run 1, as indicated by increase in AE activity and the cumulative AE energy. Meanwhile in Run 2 and 3, CFN formation occurred at 25 and 27 MPa, respectively. The CFN formation pressures were close to those predicted by Griffith failure criterion for σ_t = 7 MPa. Fractures formed in Run 1 (about 1 - 2 visible fractures per cm^2) were narrower than those in Run 2 (about 6 – 7 visible fractures per cm^2) and 3 (about 3 visible fractures per cm^2), which were formed at larger differential stress, as inferred from the number of visible fractures in the X-ray CT section. Fractures formed in Run 3 were inferred to be narrower than

those formed in Run 2, of the same differential stress; the difference was likely due to variation in the Young's modulus, yield strength, and tensile strength amongst samples, as implied by the experimental results in Chapter 2.

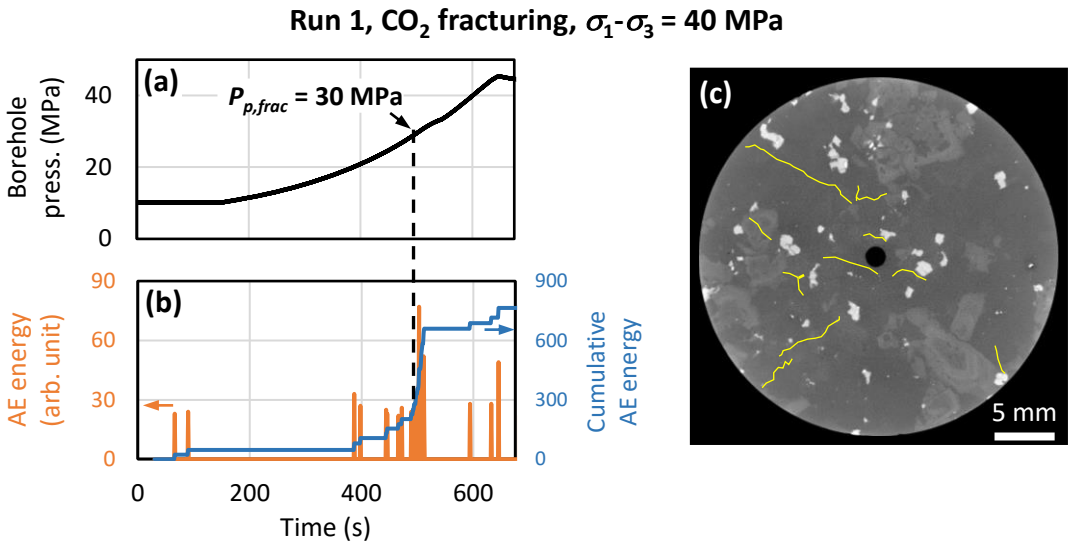

Figure 4.3. Results of CO_2 fracturing in Run 1: (a) borehole pressure, (b) AE energy (orange) and cumulative AE energy (blue), and (c) X-ray CT section of the sample. Fractures are highlighted in yellow to increase grayscale visibility

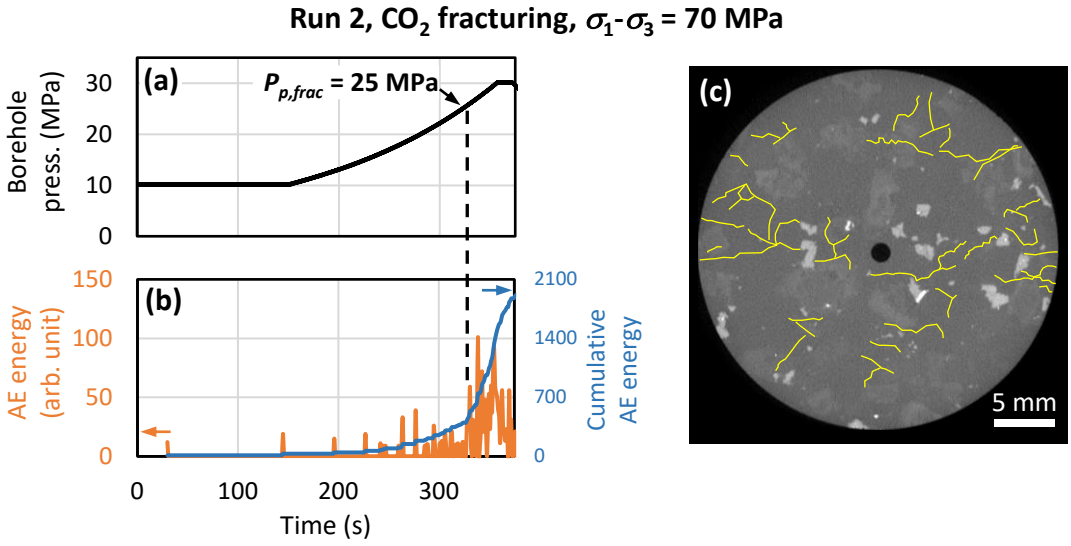

Figure 4.4. Results of CO_2 fracturing in Run 2: (a) borehole pressure, (b) AE energy (orange) and cumulative AE energy (blue), and (c) X-ray CT section of the sample. Fractures are highlighted in yellow to increase grayscale visibility

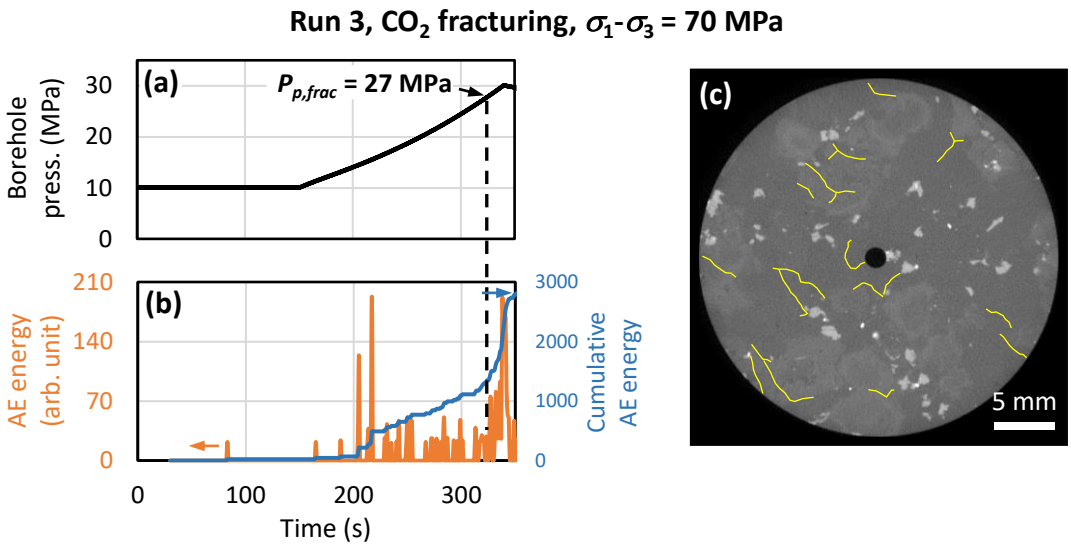

Figure 4.5. Results of CO_2 fracturing in Run 3: (a) borehole pressure, (b) AE energy (orange) and cumulative AE energy (blue), and (c) X-ray CT section of the sample. Fractures are highlighted in yellow to increase grayscale visibility

Figure 4.6 depicts fluid pressures, and the computed injection flow rate of GLDA flow-through in Run 1. Relatively small but continuous axial shortening (approximately 20 μm in 6 h), along with sparse and low-energy (approximately 10 arb unit) AE activity occurred since the beginning (time before GLDA solution injection) of this experiment; similar phenomena were also observed in GLDA-flow through Run 2 and 3 experiments. The axial deformation rate and the corresponding AE activity in the GLDA-flow through experiments were negligible compared to those that occurred in the CO_2 fracturing of the same conditions. It appeared that due to the high viscosities (c.a. 300 μPa · s), the GLDA solutions only effectively penetrated certain wide fractures in the CFNs or penetrated the CFNs in limited locations; thus, the pressure and the void formation and fracture widening due to mineral dissolution did not cause significant changes in the effective stresses within the rock. Ultimately, there was no significant deformation promoted in the rock, as it was expected, that would otherwise potentially occurred if CO_2 (viscosity ≈ 33 μPa · s) was injected at the same pressure values, via CO_2 penetration into most fractures in the CFNs. The mineral dissolutions due to GLDA injections, however, caused a continuous increase in the injection-flow rates throughout GLDA flow experiments. In Run 1, approximately 2.2 times permeability enhancement factor was achieved in 5 h, based on comparison of two flow rate values indicated by red arrows in Figure 4.6.

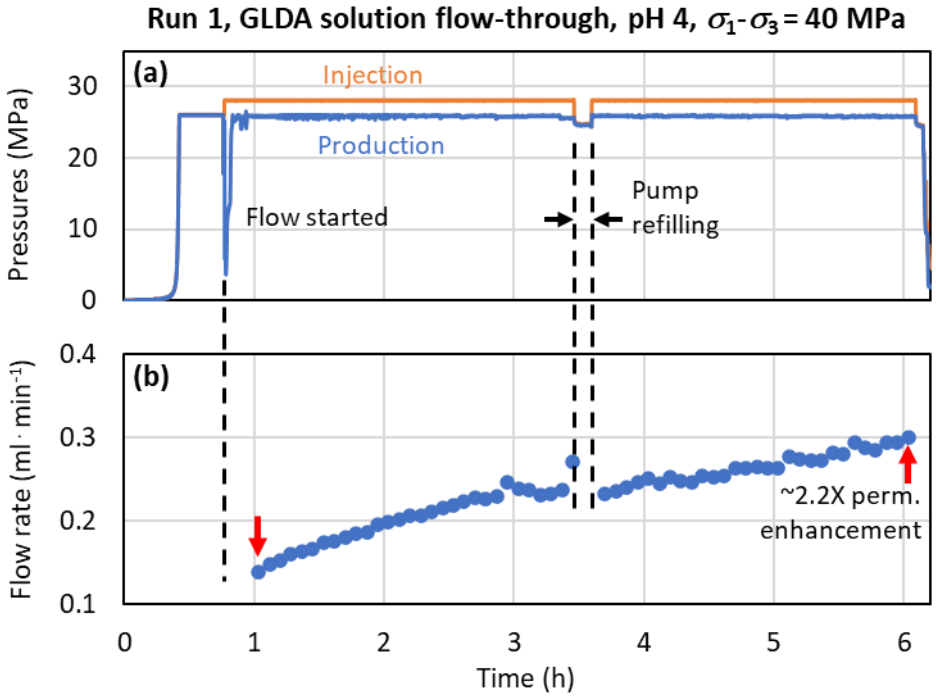

Figure 4.6. (a) Injection and production pressures, and (b) calculated injection flow-rates during GLDA solution flow-through in Run 1. Permeability enhancement factor is obtained based on two flow rate values pointed by red arrows

Permeability enhancement was attributed to void formation due to biotite dissolution and fracture widening, as observed in the X-ray CT images of the sample post-experimentation (Figure 4.7a). Although it was not obvious, the number of voids appears to be higher near the borehole. The estimated porosity of the sample post experimentation was approximately 0.049%. Note that porosity values reported in this chapter were lower than the known porosity values (about 0.5-0.8%, Table 2.1) of intact Inada granite, because the porosity values in this chapter were estimated from X-ray CT data. The elevated Fe concentration in the effluent (Figure 4.8) ascertains biotite dissolution; meanwhile, the considerable Si, Al, and Ca concentrations in the effluent also indicated feldspar minerals dissolution, which were mostly responsible for fracture widening. These results are consistent with those of previous studies on GLDA solution injection into Inada granite at the same temperature and pH conditions (Watanabe et al., 2021b; Takahashi et al., 2023).

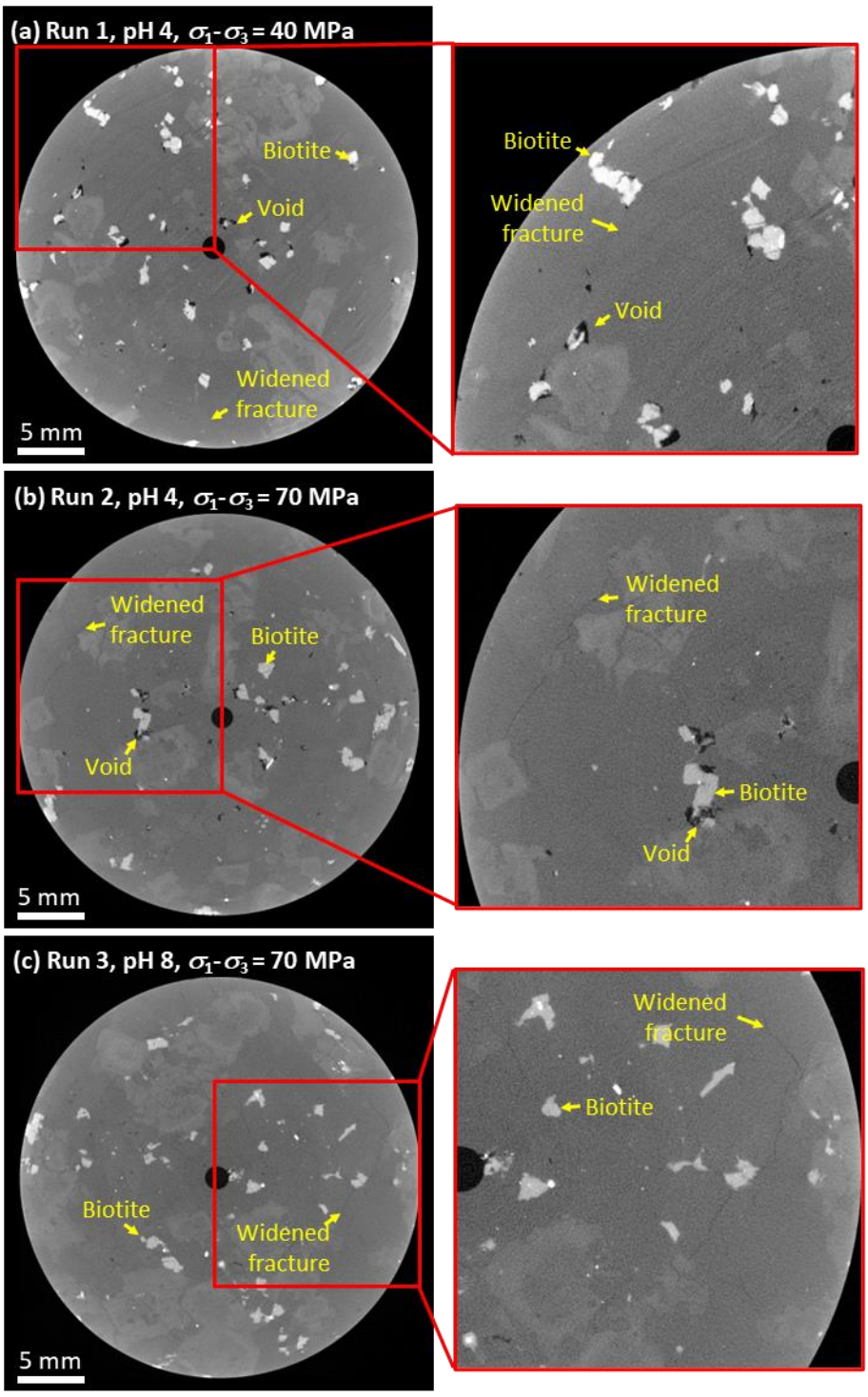

Figure 4.7. X-ray CT images of the rock samples after the experiment at (a) pH 4 and differential stress = 40 MPa, (b) pH 4 and differential stress = 70 MPa, (c) pH 8 and differential stress = 70 MPa. Yellow arrows depict the example biotite, voids, and widened fractures

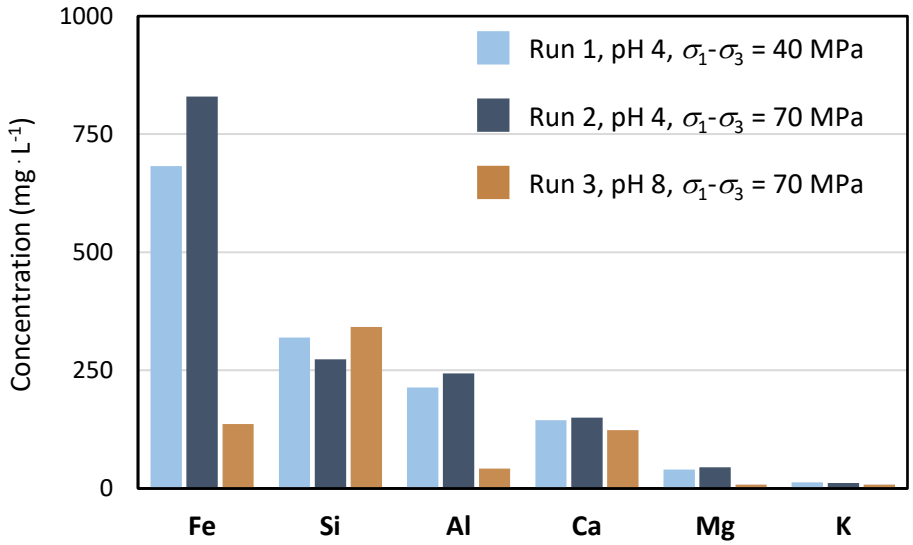

Figure 4.8. Concentration of Fe, Si, Al, Ca, Mg, and K in the effluent from GLDA flow-through experiment in Run 1 (light blue), Run 2 (dark blue), and Run 3 (brown)

Continuous permeability enhancement achieved 2.4-times enhancement factor within 5 h (similar to that in Run 1) in experimental Run 2 (Figure 4.9) of larger differential stress. X-ray CT images post experimental Run 2 (Figure 4.7b) also suggested qualitatively similar degree of void formation and fracture widening to those observed in Run 1. The porosity based on X-ray CT data was about 0.097%, which was in the same order to that in Run 1. Moreover, each element analyzed in the effluent from Run 2 was at similar concentration level to that in the effluent from Run 1 (Figure 4.8).

Fluid pressures and the computed injection flow rate of GLDA-flow through in Run 3 is presented in Figure 4.10. Continuous permeability enhancement was observed; approximately 2.2-permeability enhancement factor was achieved within 5 h, similar to those observed in Run 1 and 2. Post-experimental X-ray CT sections (Figure 4.7c) reveal that biotite dissolution was negligible; meanwhile, fracture widenings were still observed, which should have been contributed to the permeability enhancement. The porosity based on X-ray CT data was 0.0057%, which was one order lower than those in Run 1 and 2. The concentrations of the elements in the effluent, except for Si and Ca, were generally decreased as compared to those in Run 1 and 2 (Figure 4.8). According to Takahashi et al. (2023), the effluent characteristics in Run 3 suggested enhanced quartz dissolution and lower dissolution rate (compared to those at pH 4) in biotite and other minerals, which agreed with the X-ray CT sections.

These results appeared to agree with the negligible axial-shortening rates and the low-energy AE activities in all experimental runs; GLDA solutions might have only effectively penetrated certain number of wide fractures in the CFNs or penetrated in limited location within the rock, so that the pressure and the mineral dissolutions did not promote significant stress-changes and deformation in rock. The results, therefore, suggest that variation in differential stress does not significantly affect the permeability enhancement process in CFNs via GLDA-solution injections in both weakly acidic and alkaline conditions.

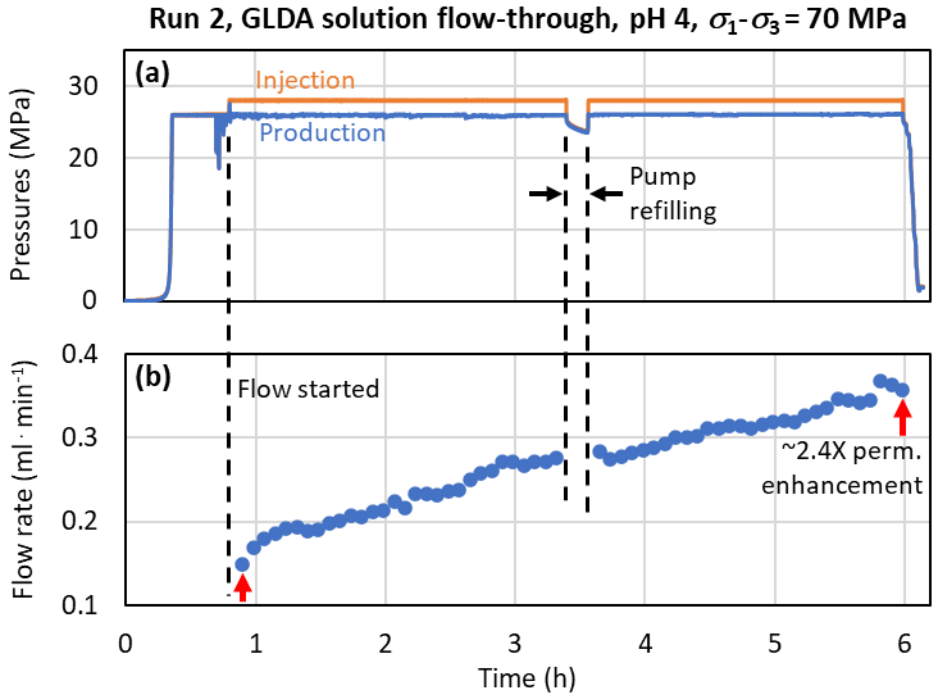

Figure 4.9. (a) Injection and production pressures, and (b) calculated injection flow-rates during GLDA solution flow-through in Run 2. Permeability enhancement factor is obtained based on flow rate values indicated by red arrows

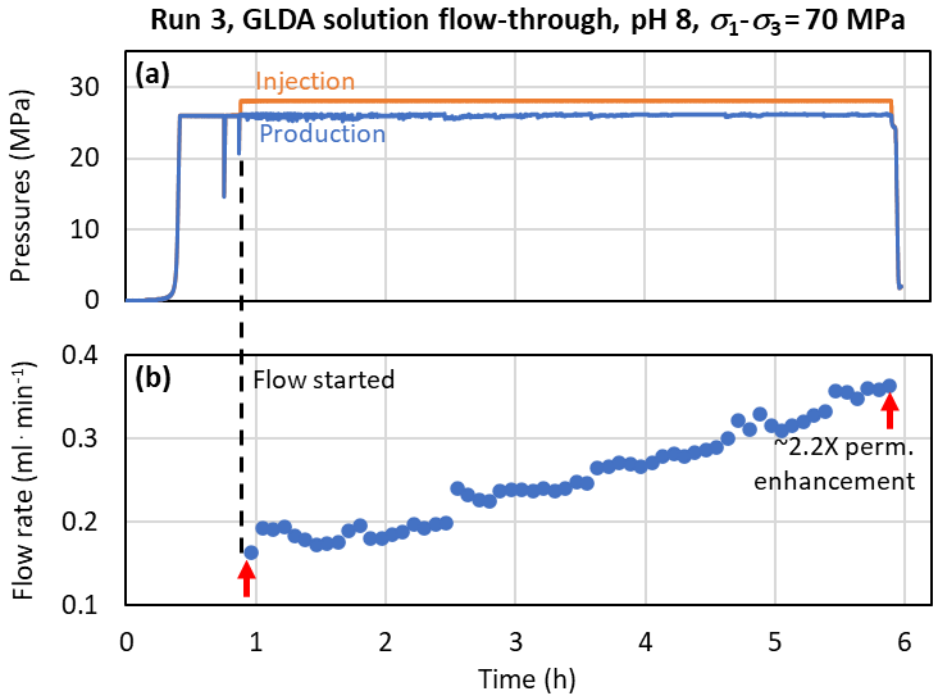

Figure 4.10. (a) Injection and production pressures, and (b) calculated injection flow-rates during GLDA solution flow-through in Run 3. Permeability enhancement factor is obtained based on flow rate values pointed by red arrows

4.3.2. Permeability Enhancement on a Large Scale and under Radial Flow Conditions

Continuous sample shrinkage occurred throughout the Run 4 experiment. Even so, the rock deformation rate, and the acoustic emission activity during the GLDA flow-through in this experiment, were mostly insignificant as compared to those in CO_2 fracturing (Chapter 2) under similar temperature and stress state conditions. Considerable AE-activity occurred only during increase in borehole pressure due to change from water to GLDA injection; pore pressure changes around the borehole caused deformations in some fractures.

Time evolution of differential pressure between borehole and sample side faces, concentration of the elements in the effluent, and pH of the effluent are summarized in Figure 4.11. The initial average permeability of the sample, computed during water injection when both injection and production pressures stabilized (time *T1*, Figure 4.11a), was 1.2×10^{-17} m^2. Increase in the differential pressure to approximately 2 MPa occurred within approximately 20 min after GLDA solution at pH 4 was injected (time *T2*). This was because the GLDA solution had higher viscosity than water. Computed average permeability at time *T2* was 9.3×10^{-18} m^2, slightly lower than that at time *T1*. The lower computed permeability at time *T2* was suspected to be the result of fracture closures as pore pressure near the borehole dropped during the switch from water to GLDA solution injection. It might also because most of the fractures could not effectively contribute to the GLDA solution flow. Increase in the concentration of elements in the effluent was then observed; remarkable increase in Fe indicated biotite dissolution, while significant increase in Ca and Al indicated feldspar minerals dissolution.

After time *T2*, the differential pressure did not drop as it was expected in permeability enhancement based on Eq. (4.1). At the end of GLDA injection at pH 4 (time *T3*), the computed average permeability was 7.3×10^{-18} m^2. Nonetheless, concentrations of elements in the effluent, especially Fe and Al, remained high throughout the injection at pH 4, indicating that biotite and feldspar mineral dissolution continued to occur. This behavior was unlikely to be caused by silica precipitation because the Si concentration in the effluent was generally in between the solubility value of quartz (100 mg $\cdot$ L^{-1}) and amorphous silica (400 mg $\cdot$ L^{-1}) in water at 200 °C and 5 MPa (Manning, 1994; Karásek et al., 2013). Additionally, based on the concentrations of Al, Ca, Fe, and Mg, the computed concentration of unreacted GLDA-Na_4 in the effluents was > c.a. 62% of that (c.a. 0.65 mol $\cdot$ L^{-1}) in the 20-wt% GLDA-Na_4 solutions throughout the experiment; it was ascertained that mineral dissolution would never be suppressed due to lack of GLDA concentration.

Apparently, the slight increase in the differential pressure during GLDA injection at pH 4 was because the high-viscosity GLDA solution was still penetrating more fractures, especially around the borehole due to the higher pore pressure than that near the sample side faces in the radial flow condition. This situation would have resulted in larger permeability enhancement near the borehole than that near the sample side faces. Conversely, GLDA penetration should have occurred in fewer fractures near sample side faces, due to the lower pore pressure conditions. Moreover, as suggested in Section 2.3.3, wider fractures are more common in quartz (less likely to be dissolved at pH 4) than in feldspar minerals (Figure 4.12a); thus, mineral dissolutions would have occurred in even fewer fractures near the sample side faces (Figure 4.12b). If the injection at pH 4 was maintained for a longer time, differential-pressure

drop might eventually be observed due to expansion of the zone with higher permeability enhancement.

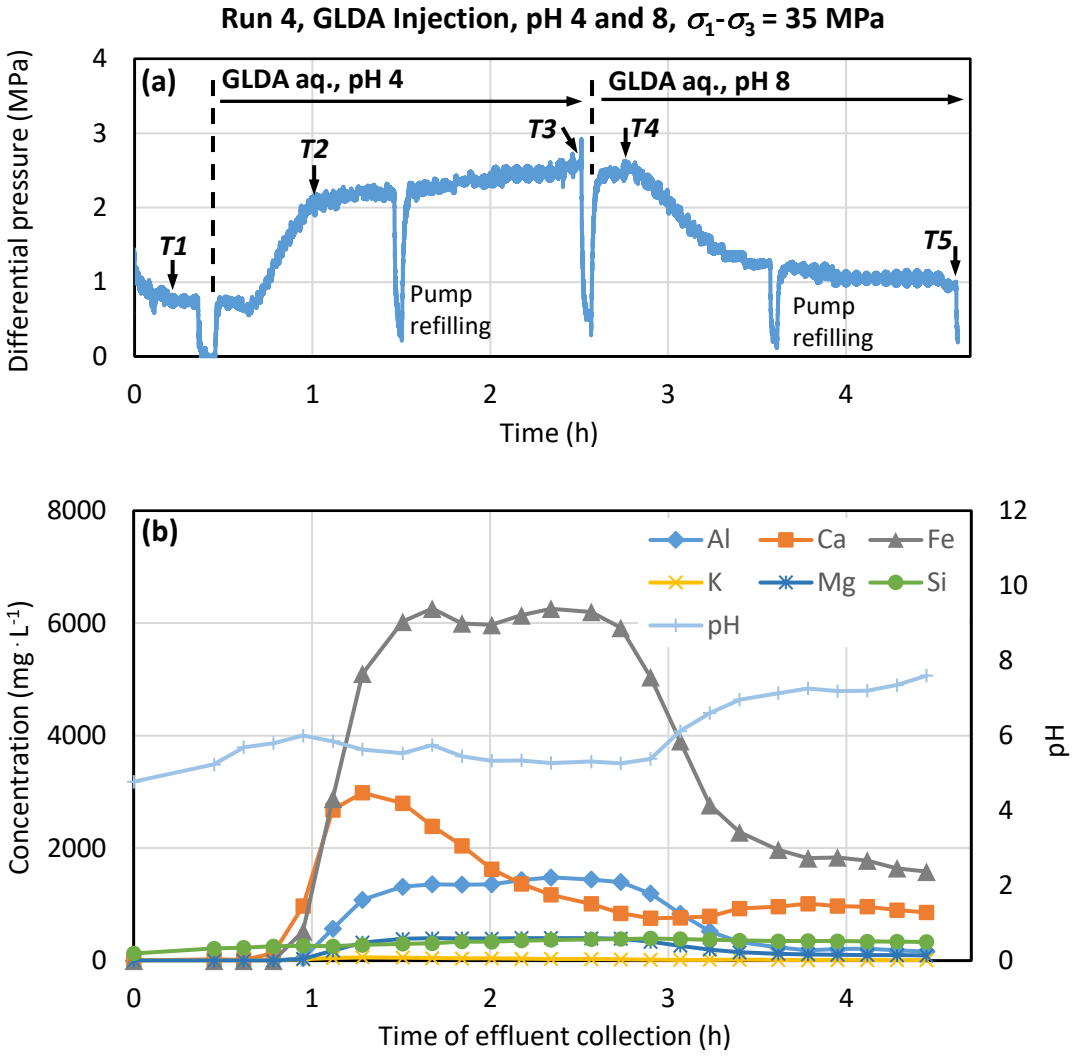

Figure 4.11. Time evolution of (a) differential pressure between borehole and sample side faces, and (b) elemental concentrations in the effluent, and the pH during the GLDA-solution injections with the successive use of pH 4 and pH 8 under a true-triaxial stress condition (Run 4)

At the beginning of GLDA solution injection at pH 8 (time *T4*), the average permeability was 7×10^{-18} m^2, which was similar to that at time *T3*. However, differential pressure drop was observed after time *T4*. Enhanced quartz dissolution (Takahashi et al., 2023), wherein wider fractures are suggested to be more common in granite CFN (see Section 2.3.3; also, can be inferred from thin sections in Takahashi et al., 2023), likely provided considerable enhanced flow-paths. Together with the chemically stimulated fractures in feldspar minerals, the chemically stimulated fractures in quartz created more and enhanced connecting flow-paths between the borehole and sample side faces (Figure 4.12c). As the differential pressure decreased, so did the pore-pressure in the sample; GLDA penetration into more fractures became less likely. The permeability enhancement rate, thus, became slower (reflected in slower decrease in the differential pressure, Figure 4.11a) towards the end of the experiment. At the end of the

injection at pH 8 (time *T5*), an average permeability of 1.85×10^{-17} m^2 was obtained, and it was approximately 1.6-times higher than the initial average permeability.

Based on the average permeability value at time *T5*, assuming the radius of the intense mineral dissolution (higher permeability enhancement) zone was 2 cm from the center (i.e., r_1, based on the diameter of the samples used at conventional-triaxial stress conditions), and assuming permeability enhancement near sample side faces was negligible, the permeability around the borehole should have been approximately 2.9×10^{-17} m^2 or 2.5-times the initial value [Eq. (4.2)]. It would mean that GLDA solution injection at each pH contributed to about 1.57-permeability enhancement factor (i.e., square-root of the 2.5-enhancement factor) near the borehole. The approximately 1.57-permeability enhancement factor for each pH condition was comparable to that from experiments under conventional triaxial stress conditions, considering the shorter injection duration (2 h) for a pH condition in this experiment versus 5 h in the experiment performed at conventional-triaxial stress conditions.

P-wave velocities in the sample exhibited increases compared to the velocities before the experiment (Table 4.2, Figure 4.13). This was due to the decrease in apertures of the thermally induced fractures (having had formed at atmospheric pressure) as the sample was subjected to compression (Watanabe et al., 2021b; Salalá et al., 2022; Takahashi et al., 2023). If the P-wave velocity measurements (before and after GLDA solution injection) could be performed while the sample was under the stressed condition, the mineral dissolutions would apparently result in some degree reduction in the absolute values due to void formations and widening in certain fractures. Nonetheless, the measured average P-wave velocities in the three principal stresses directions of the sample post-experimentation were isotropic (Table 4.2, Figure 4.13), which suggest an isotropic permeability. The distribution of the P-wave velocities, however, did not demonstrate clear distribution of zones with higher number of voids (Figure 4.13) with respect to borehole position.

X-ray CT sections on the cores obtained from the sample post-experimentation verified that there were more voids (due to biotite dissolution) near the borehole than those near the sample side faces (Figure 4.14). There were also approximately 55% more visible fractures (about 14 fractures per cm^2) near the borehole than those (about 9 fractures per cm^2) near the sample side faces; these fractures should have been chemically stimulated by the GLDA solutions. The porosity of the rock around the borehole and near sample side faces were approximately 0.11% and 0.028%, respectively, based on the X-ray CT data. Nevertheless, the X-ray CT images suggested that there was no apparent relationship between stress orientations and the distribution of voids and visible fractures.

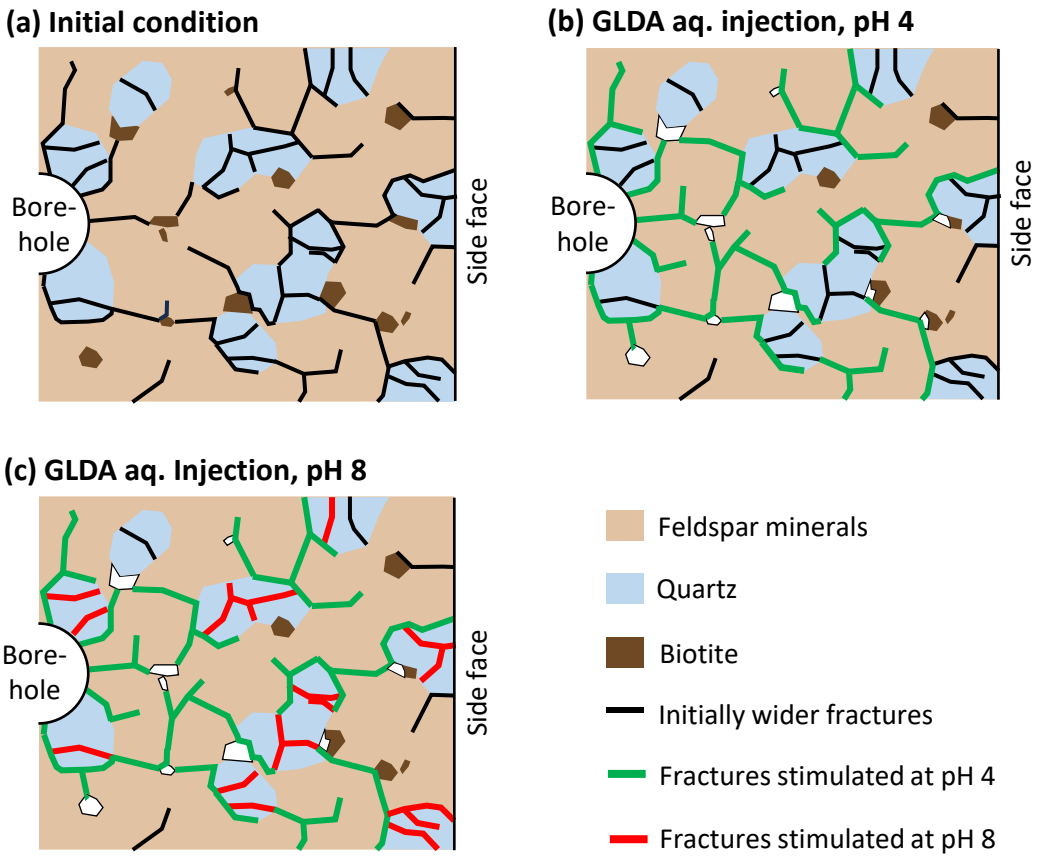

Figure 4.12. Illustration (not to scale) of permeability enhancement process on the sample due to successive injection of GLDA solutions at pH 4 and 8 under radial flow condition in Run 4

Table 4.2. Average P-wave velocities in each principal stress direction before and after the experiment of Run 4

Direction	Average P-wave velocities ($m \cdot s^{-1}$)			
	Before experiment		After experiment	
	Value	% of value at σ_1 direction	Value	% of value at σ_1 direction
σ_1	1819.6	100.0	2402.3	100.0
σ_2	1651.4	90.8	2578.1	107.3
σ_3	2048.5	112.6	2241.6	93.3

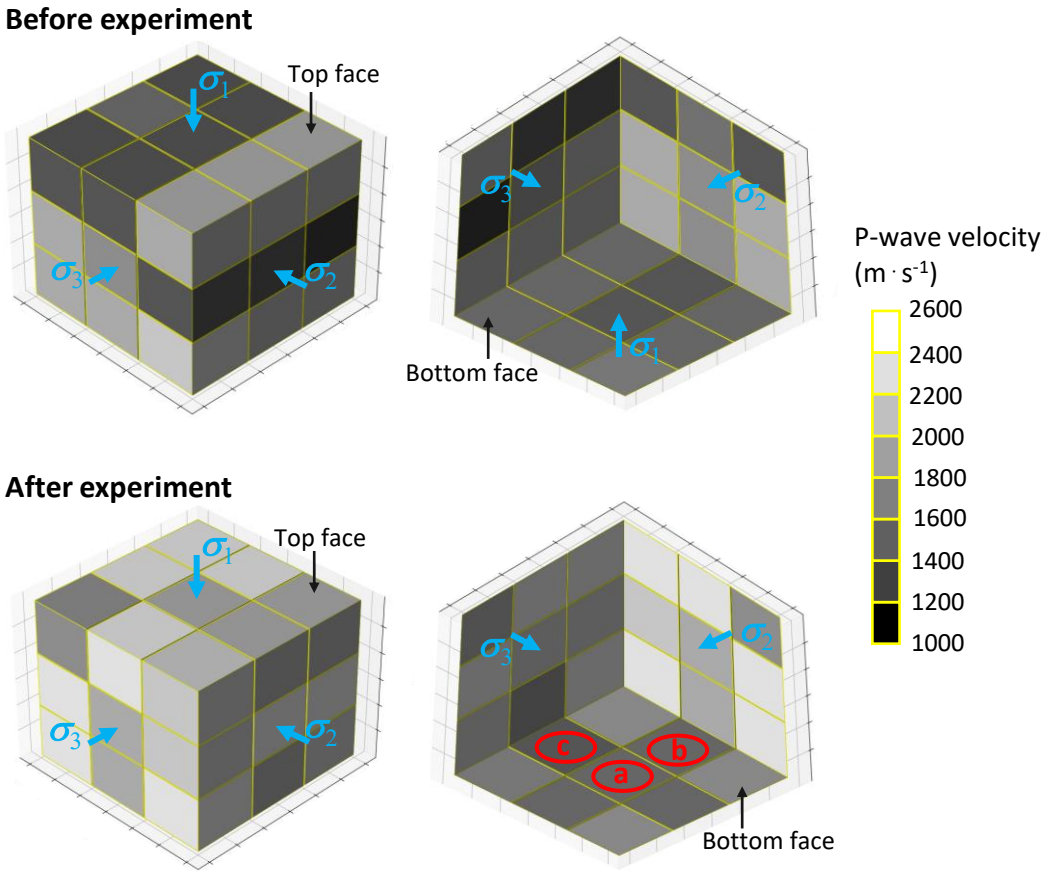

Figure 4.13. Distribution of estimated P-wave velocities for the sample before and after chelating agent-injection Run 4 experiment, where left and right cubes depict each other's invisible faces. Red circles in the bottom face of the after-experiment cube depict the location of cores obtained for X-ray CT scan; (a) around borehole, (b) near sample side face at centered σ_1–σ_2 plane, (c) near sample side face at centered σ_1–σ_3 plane

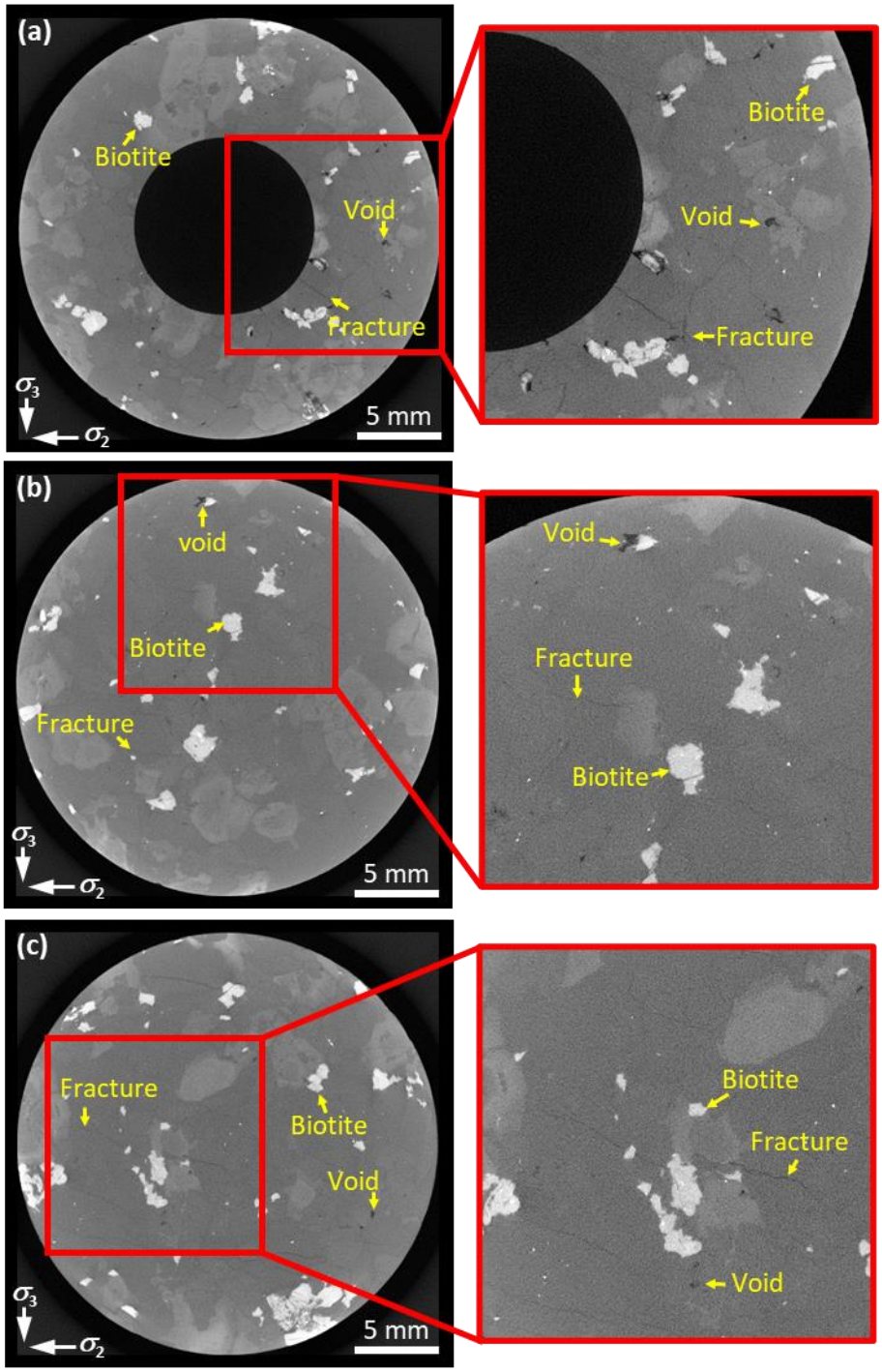

Figure 4.14. Representative X-ray CT images of the rock sample at σ_2-σ_3 planes post injection of GLDA solutions in Run 4: (a) around borehole, (b) near sample side face at centered σ_1-σ_2 plane, (c) near sample side face at centered σ_1-σ_3 plane. Yellow arrows indicate the example of biotite crystals, voids, and fractures

4.4. Field Application of Chelating Agent Injection

These experiments demonstrated that variation in stress state and magnitude does not significantly affect permeability enhancement process by GLDA solution at both pH 4 (weakly acidic) and pH 8

(weakly alkaline) conditions; due to the higher viscosity of GLDA solution than water and CO_2, mineral dissolutions occur effectively only in certain number of fractures or in limited locations in the rock so as not promoting significant rock deformation. Experiments in this chapter suggest that GLDA solution can be injected at pressures close to σ_3 values, even if it is higher than $P_{p,frac}$, to allow efficient penetration into the CFN. In naturally fractured geothermal environments (environments with meter-scale natural fractures, as implied by Tester et al. (2006)), GLDA may be injected just below the pressures required for hydroshearing to prevent shearing on the natural fractures, minimizing excessive induced seismicity.

Due to the characteristics of mineral dissolution in GLDA solution injection at pH 4, the injection at pH 4 may be performed with lower GLDA concentrations to reduce the GLDA solutions viscosity, allowing for penetration into more fractures, and achieving larger chemically stimulated volume than if the solution was more concentrated. The lower concentrations would also reduce the mineral dissolution rates, which are beneficial for achieving larger chemically stimulated volume (Rose et al., 2010; Watanabe et al., 2021b). Even though more fractures would be penetrated in the injection of lower-concentration GLDA solution, excessive deformations and acoustic emissions are still less likely in the injection of fluid more viscous than water, based on the water injection experiment into sawcut (Section 3.3.2). As pressure-gradient will decrease in the chemically stimulated volume, keeping the injection pressure close to constant will allow for optimum chemical-stimulation radius, based on Eq. (4.2); the pressure gradient in the stimulation front will be sufficiently high to keep GLDA flow into the chemically unstimulated volume to enable the expansion of the stimulated radius (which can be expressed by r_1 in Eq. (4.2)).

Subsequent injection of GLDA solution at pH 8 will provide optimum permeability enhancement in the chemically stimulated volume, in agreement with Takahashi et al. (2023); permeability enhancement on fractures in quartz would provide more enhanced connections to the fractures stimulated earlier at pH 4. The subsequent injection at pH 8 should also be performed using constant injection pressure to achieve optimum chemical stimulation radius. Based on these elucidations, GLDA solution injection at single pH of 4 or 8 would not result in optimum permeability enhancement, especially at a greater distance from borehole; at pH 4, the chemically stimulated fractures would be considerably sparse, as initially wider fractures in feldspar minerals are less common than those in quartz. However, at pH 8, the chemically stimulated fractures in quartz would be interconnected to the less chemically stimulated fractures in feldspar minerals.

4.5. Schemes for Creating Geothermal Reservoirs by CO_2 Injection

This study demonstrated that CO_2 injection induced the preferably complex CFNs, including induced large shear displacement on natural fractures if they were present; both have significant potential to contribute to geothermal reservoir creation. Nonetheless, the capability of CO_2 to uniformly pressurize large area of fracture implies an increased risk of large induced seismicity (Rutqvist and Rinaldi, 2019), such as those with moment magnitude (M_W) $\geq$ 2.0 as defined by the authorities in Helsinki, Finland (Kwiatek et al., 2019), especially in the presence of fault. These characteristics imply

that creating geothermal reservoir via CO_2 injection is best to be performed in geothermal environments without faults or reasonably far from faults.

Nevertheless, creating geothermal reservoirs via CO_2 injection should be still performed in accordance with the general suggestion (e.g., Chabora et al., 2012; Kwiatek et al., 2019) to minimize the risk of large induced seismicity; CO_2 injection should be employed to keep the subsurface pressures as low as possible. The concern of insufficient permeability enhancement due to the low-pressures should be addressed using complementary methods, such as chelating-agent injection. Therefore, possible stimulation schemes were made based on findings in this study, combined with knowledge acquired in field studies.

Chabora et al. (2012) described a well-stimulation scheme in a conventional geothermal environment (depth and temperature of approximately 1 km and 190 °C) predominantly using water injection. In general, the scheme comprises hydroshearing, chemical stimulation, and controlled-hydraulic fracturing phase; they are generally progressed from method incorporated low pressures to the ones with high pressures. Each phase also comprised repeats from low to high pressures. The decision to repeat a stimulation method using high pressures, or proceeding to the next phases, was based on whether or not the economic water injectivity (which reflects permeability) of ≥ 0.75 gpm $\cdot$ psi^{-1} (gallon per minute per pound per square inch) or approximately ≥ 6.7 kg $\cdot$ s^{-1} $\cdot$ MPa^{-1} had been achieved.

Similar general scheme to those described in Chabora et al. (2012) may be employed in CO_2 injection into conventional geothermal environment of approximately 150–200 °C; CO_2 fracturing, or hydroshearing using CO_2 in case of environment with considerable number of natural fractures, should be performed to create or recreate complex network of permeable fractures (Figure 4.15). The hydraulic stimulations would allow for deep penetration of GLDA solutions in the later phase if the preceding hydraulic stimulation does not achieve the economic injectivity. If economic injectivity was not achieved post GLDA injection into the hydro-sheared natural fracture network, CO_2 fracturing may be performed and followed by another GLDA injection, as necessary. Recall that CFN formations occurred at fracture formation pressures ($P_{p,frac}$) predictable by Griffith failure criterion (Eqs. 2.1 and 2.2), which were always higher than the pressures required for shear slip of natural fractures (Eqs. 3.1–3.3) for the same rock tensile strength and stress state condition; thus, inducing CFN in naturally fractured environments should be done by increasing the CO_2 pressure to $P_{p,frac}$. Additionally, the threshold for economic injectivity in CO_2-based EGS would be different from the generally accepted value of approximately 0.75–1 gpm $\cdot$ psi^{-1} in water-based EGS. It is because CO_2 has lower specific heat capacity than water, but allows for higher mass flow rate (Brown, 2000; Pruess, 2006). The threshold for economic injectivity in CO_2-based EGS appears to be a subject for more detailed studies.

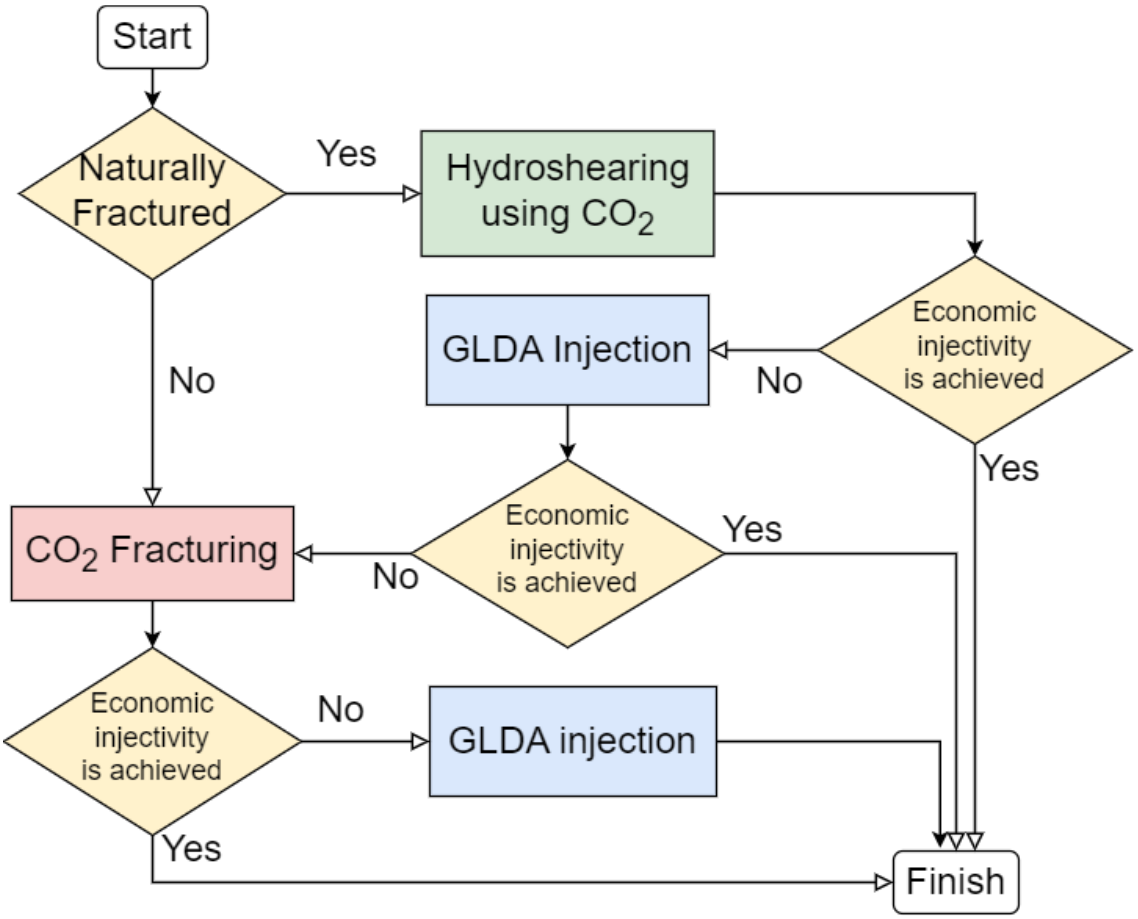

Figure 4.15. General flow chart for stimulation methods may be employed in conventional geothermal environments at temperatures of approximately 150–200 °C

GLDA solution injection is difficult to be implemented in geothermal environment with temperatures >200 °C (including superhot geothermal environments); chelating agents, including GLDA, generally degrade relatively fast at above 200 °C (e.g., Martell et al., 1975; Sokhanvarian et al., 2016). Thus, creating geothermal reservoir at temperatures of >200 °C may be performed in phases described by Figure 4.16. CO_2 fracturing, or hydroshearing using CO_2 when there is substantial number of natural fractures, should be performed first. If hydroshearing is performed first, and the economic injectivity is not achieved, the CO_2 fracturing should be later performed by increasing the CO_2 pressure to CFN-formation pressure ($P_{p,frac}$). Long pressurization duration at above $P_{p,frac}$ may be performed if economic injectivity is still not achieved post CO_2 fracturing, as suggested by Goto et al. (2021).

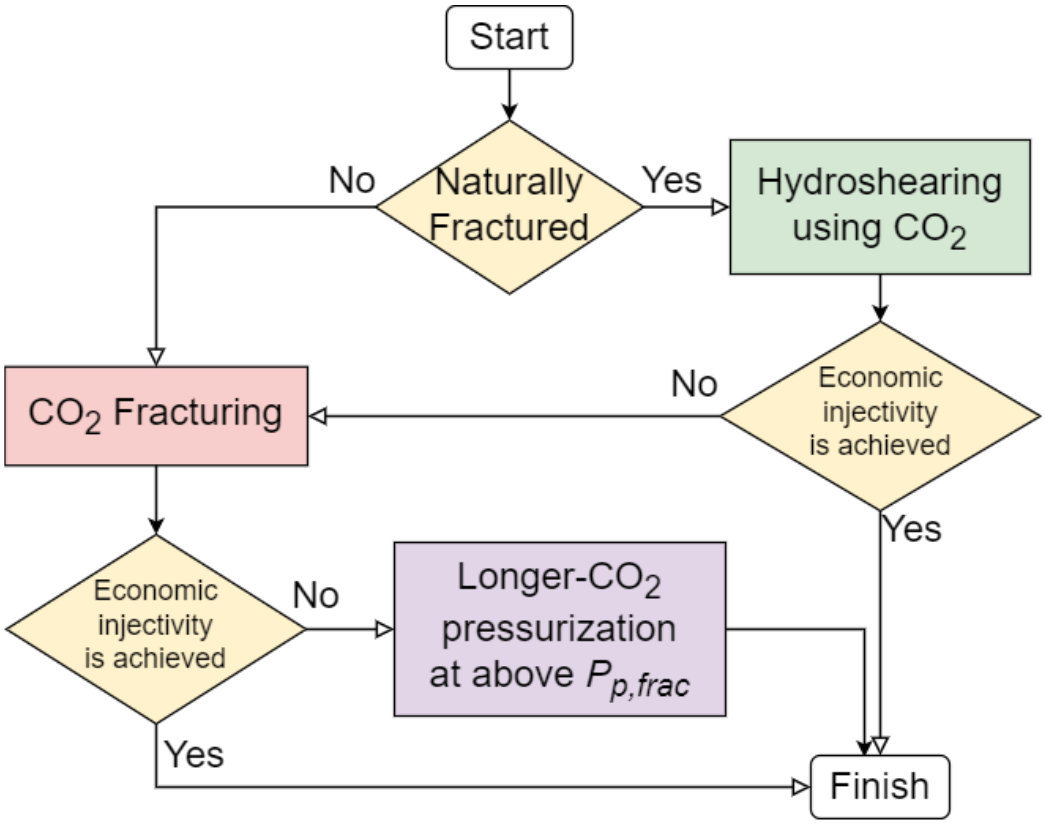

Figure 4.16. General flow chart for stimulation methods may be employed in conventional geothermal environments at temperatures > c.a. 200 °C

4.6. Conclusions of this Chapter

The author elucidated through experiments that injection of GLDA solution into CO_2 injection-induced CFNs results in similar permeability-enhancement factor under a conventional geothermal temperature with varying stress states, at both weakly acidic and alkaline conditions. The higher viscosities of GLDA solutions, as compared to CO_2, likely cause penetration and mineral dissolution only effectively occur in a certain number of wide fractures, so as significant deformation in the fracture network is not promoted.

At large scale and in radial flow geometry, injection of GLDA solutions at pH 4 (weakly acidic condition) tend to result in zone with high permeability enhancement factor around the borehole. It might be because void formation (due to biotite dissolution) and fracture aperture widening (due to dissolution of majorly feldspar minerals) are more effective near the borehole due to the higher pore pressure. This finding suggests that injection of weakly acidic GLDA solutions should be performed using low concentration to reduce the viscosity and dissolution rate; thus, achieving GLDA penetration into more fractures and greater chemically stimulated radius. Constant injection pressure would also achieve optimum chemical-stimulation radius, as it would keep large pressure-gradient in the stimulation front, enhancing GLDA solution flow into the chemically unstimulated zone.

Consistent with previous studies, successive GLDA solution injection at pH 8 would provide optimum permeability enhancement in the chemically stimulated zone. It would occur via quartz

dissolution, which would provide more connecting flow-paths in the chemically stimulated zone. Injection at pH 8 should also be performed using constant injection pressure for the GLDA solution to reach most parts in the zone previously stimulated in GLDA injection at pH 4.

Based on the findings in Chapter 2–4, combined with knowledge from previous studies, two-general stimulation schemes can be created; both schemes follow the general suggestion to reduce the risk of large induced seismicity, where the stimulation should be initiated using method that required the lowest pressures. In conventional geothermal environments with temperatures up to 200 °C, CO_2 injection should be performed first to achieve initial gain of permeability. The next phase of chemical stimulation using chelating agent and further hydraulic stimulation phase can be performed based on whether the commercial injectivity has been achieved. In geothermal environments with temperatures > c.a. 200 °C, the scheme would comprise CO_2 injection to achieve CFN or hydroshearing and further stimulation by long CO_2-pressurization duration above fracture pressure, if necessary.

Chapter 5 : Conclusions

Formation of complex CFNs in granite via the stimulation of pre-existing microfractures by low viscosity water (near or above its critical temperature) has been suggested to provide efficient thermal extraction from a geothermal reservoir (Watanabe et al., 2017b; 2019); thus, CFNs have potential significant contribution in the creation of geothermal reservoir in superhot (> c.a. 400 °C) geothermal environments. Nonetheless, the utilization of water is characterized by specific challenges. For instance, it is challenging to maintain the permeability in a water based superhot-EGS due to competing process between free-face dissolution and stress solution of fracture asperities (Watanabe et al., 2020).

Previous studies (e.g., Brown, 2000; Pruess, 2006) have suggested CO_2 as a replacement for water in EGS reservoirs development, especially in conventional geothermal environments, because CO_2 is less reactive to rock forming minerals (e.g., Brown, 2000; Pruess, 2006), relatively easier and safer to handle as compared to the competing replacements of N_2 and He (Gandossi and Estorff, 2015; Moridis, 2018), and reduces water footprint (Wilkins et al., 2016). Moreover, CO_2 has low viscosity (<100 μPa·s) over vast range of conditions (Heidaryan et al. 2011), which highlights its potential to induce CFNs from conventional (c.a. 150– 300 °C) to superhot geothermal conditions. Nonetheless, even though laboratory experiments (Ishida et al., 2016; Isaka et al., 2019) on CO_2 injection have been performed to demonstrate fracturing in granite under geothermal conditions (up to 300 °C), the possibility and characteristics of the more complex CFN formation via CO_2 injection in conventional and superhot geothermal environments were yet to be elucidated. The possibility and characteristics of CO_2 injection-induced CFN formation in naturally fractured geothermal environments, along with the shearing of the natural fractures, were also required to be elucidated as they potentially contribute to significant permeability enhancement. As implied by previous studies (Ishida et al., 2016; Watanabe et al., 2017b; Isaka et al., 2019), CO_2 injection-induced CFN would contain narrow fractures, especially at conventional geothermal conditions. Therefore, complementary methods to overcome the challenge, such as chemical stimulation using chelating agent at conventional geothermal conditions (Watanabe et al., 2021b), need to be elucidated.

This study demonstrated that CFNs can be induced by CO_2 injection at conventional and superhot geothermal conditions, via CO_2 injection experiments into granite samples. Fracture aperture in the CFNs was suggested to increase with increasing differential stress and temperature. CO_2 injection-induced CFNs were also elucidated to be formed at pressures predictable by Griffith failure criterion, in agreement with the previous studies on CFN formation at superhot temperatures. CO_2 injection into granite samples with sawcut inclined from the direction of maximum principal stress revealed that CFNs can possibly be formed in naturally fractured geothermal environments (environments with meter scale natural fractures, as implied by Tester et al. (2006)), along with large-shear displacement on the natural fractures, although the CFNs comprise narrow fractures.

Goto et al. (2021) have suggested and demonstrated that long duration pressurization at above fracture pressure could overcome the challenge of narrow fracture aperture in the CFNs at superhot geothermal conditions, whereas at a conventional geothermal temperature (200 °C) with hydrostatic

stress conditions, permeability enhancement in the network of microfractures has been demonstrated using injection of chelating agent (Watanabe et al., 2021b; Takahashi et al., 2023). This study demonstrated that permeability enhancement via chelating agent injection is unaffected by variation in stress state, under both weakly acidic and alkaline conditions. It is likely because the chelating agent solution, which has higher viscosity than both water and CO_2, only penetrates and dissolves minerals in certain wide fractures or at limited locations in the fracture network. Nonetheless, it was demonstrated that at larger scale and under radial-flow geometry, chelating agent injection at weakly acidic condition tends to create intense chemically stimulated zone near injection wellbore; thus, injection at weakly acidic condition should be performed at a low concentration for the chelating agent penetration and mineral dissolution to occur at more fractures, and achieving larger chemically stimulated zone is possible. Subsequent injection at weakly alkaline condition would increase the permeability enhancement factor inside the rock volume initially stimulated at weakly acidic condition, in agreement with the results from Takahashi et al. (2023). Injection of GLDA solution at pH 4 and 8 should be performed using constant injection pressure to achieve optimum chemical stimulation radius.

Based on results of this study, combined with knowledge from previous studies (e.g., Chabora et al., 2012; Kwiatek et al., 2019), two stimulation schemes can be created based on temperature. At temperatures up to approximately 200 °C, the schemes comprise CO_2 fracturing or CO_2 injection to induce shear-slip on the natural fractures if they are present, followed by chelating agent injections if necessary. Further CO_2 fracturing and chelating agent stimulation may be performed as well. Above c.a. 200 °C, the stimulation also comprises initially CO_2 fracturing or hydroshearing using CO_2. However, application of chelating agent is difficult at these temperatures; thus, further stimulation comprises long duration CO_2 pressurization at above fracture pressure, if required.

The results of this study suggest that creating granitic geothermal reservoir using CO_2 injection, along with the additional stimulation methods, is a potentially feasible method. Nevertheless, before its application in actual geothermal environments, several aspects need to be elucidated. First, as CO_2 has lower viscosity than water, the stimulation processes and growth of the stimulated zone within the subsurface during CO_2 injection would probably be different from those known in hydraulic stimulation using water injections. Second, thermal extraction characteristics in CO_2 injection-induced stimulated natural fractures and CFN is yet to be elucidated. Third, CO_2 may dissolve in the resident brine in the stimulation front, at which mineral dissolution or deposition may occur (Ueda et al., 2005) and affect the reservoir growth. Fourth, the process of permeability enhancement at reservoir scale in injection of chelating agent solutions also needs to be elucidated. Fifth, the significance of geological complexities, such as spatial variation in rock type, geological structures, and the resident brine, are yet to be investigated. Understanding these is essential to determine the volumes required, including the detail of the injection methods and schemes in both CO_2 and chelating agent injections. In such cases, newly designed laboratory experiments and computer simulations may be suitable to elucidate these points.

References

Asanuma, H., Muraoka, H., Tsuchiya, N., and Ito, H. (2012). The concept of the Japan Beyond-Brittle Project (JBBP) to develop EGS reservoirs in ductile zones. *GRC Transaction*s, 36, 359-364.

Batchelor, A. S. (1986). Reservoir Behaviour in a Stimulated Hot Dry Rock System. *Proceedings on Eleventh Workshop on Geothermal Reservoir Engineering*, (pp. 35-41).

Bauer, S., Huang, K., Chen, Q., Ghassemi, A., and Barrow, P. (2016). Laboratory and Numerical Evaluation of EGS Shear Stimulation. *Proceedings, 41st Workshop on Geothermal Reservoir Engineering*. Stanford: Stanford University.

Biegel, R. L., Wang, W., Scholz, C. H., Boitnott, G. N., and Yoshioka, N. (1992). Micromechanics of rock friction 1. Effects of surface roughness on initial friction and slip hardening in westerly granite. *Journal of Geophysical Research Solid Earth, 97*(B6), 8951-8964. doi:10.1029/92JB00042.

Biot, M. A. (1941). General Theory of Three-Dimensional Consolidation. *Journal of Applied Physics*, 12, 155-164. doi:10.1063/1.1712886.

Brown, D. W. (2000). A hot dry rock geothermal energy concept utilizing supercritical CO_2 instead of water. *Proceedings of the twenty-fifth workshop on geothermal reservoir engineering*, (pp. 233-238).

Byerlee, J. D. (1967). Frictional characteristics of granite under high confining pressure. J*ournal of Geophysical Research, 72*(14), 3639-3648. doi:10.1029/JZ072i014p03639.

Byerlee, J. D. (1970). The mechanics of stick-slip. *Tectonophysics, 9*(5), 475-486. doi:10.1016/0040-1951(70)90059-4.

Chabora, E., Zemach, E., Spielman, P., Drakos, P., Hickman, S., Lutz, S., Boyle, K., Falconer, A., Robertson-Tait, A., Davatzes, N. C., Rose, P., Majer, E. Jarpe, S. (2012). Hydraulic stimulation of well 27-15, Desert Peak geothermal field, Nevada, USA. *Proceedings of thirty-seventh workshop on geothermal reservoir engineering. 30*. Stanford: Stanford University.

Cladouhos, T. T., Petty, S., Bonneville, A., Schultz, A., and Sorlie, C. F. (2018). Super Hot EGS and the Newberry Deep Drilling Project. *Proceedings, 43rd Workshop on Geothermal Reservoir Engineering*. Stanford: Stanford University.

Cornet , F. H., and Jianmin, Y. (1995). Analysis of induced seismicity for stress field determination and pore pressure mapping. Pure and Applied Geophysics, 145, 677-700. doi:10.1007/BF00879595.

Cornet, F. H. (2016). Seismic and aseismic motions generated by fluid injections. *Geomechanics for Energy and the Environment, 5*, 42-54. doi:10.1016/j.gete.2015.12.003.

Cox, S. F. (2010). The application of failure mode diagrams for exploring the roles of fluid pressure and stress states in controlling styles of fracture-controlled permeability enhancement in faults and shear zones. *Geofluids, 10*(1-2). doi:10.1111/j.1468-8123.2010.00281.x.

Dake, L. P. (1983). *Fundamentals of reservoir engineering*. Elsevier.

Elders, W. A., Shnell, J., Friðleifsson, G., Albertsson, A., and Zierenberg, R. A. (2018). Improving Geothermal Economics by Utilizing Supercritical and Superhot Systems to Produce Flexible and Integrated Combinations of Electricity, Hydrogen, and Minerals. *GRC Transactions, 42*.

Evans, K. F., Genter, A., and Sausse, J. (2005). Permeability creation and damage due to massive fluid injections into granite at 3.5 km at Soultz: 1. Borehole observations. J*ournal of Geophysical Research Solid Earth, 110*(B4). doi:10.1029/2004JB003168.

Evans, K. F., Zappone, A., Kraft, T., Deichmann, N., and Moia, F. (2012). A survey of the induced seismic responses to fluid injection in geothermal and CO_2 reservoirs in Europe. *Geothermics, 41*, 30-54. doi:10.1016/j.geothermics.2011.08.002.

Gandossi, L. and Estorff, U. V. (2015). An overview of hydraulic fracturing and other formation stimulation technologies for shale gas production – Update 2015; EUR 26347; doi: 10.2790/379646.

Gautam, P. K., Verma, A. K., Jha, M. K., Sharma, P., and Singh, T. N. (2018). Effect of high temperature on physical and mechanical properties of Jalore granite. *Journal of Applied Geophysics, 159*, 460-474. doi:10.1016/j.jappgeo.2018.07.018.

Ghassemi, A. (2012). A Review of Some Rock Mechanics Issues in Geothermal Reservoir Development. *Geotechnical and Geological Engineering, 30*(3), 647-664. doi:10.1007/s10706-012-9508-3.

Goebel, T., Schorlemmer, D., Becker, T. W., Dresen, G., and Sammis, C. G. (2013). Acoustic emissions document stress changes over many seismic cycles in stick-slip experiments. *Geophysical Research Letters, 40*(10), 2049-2054. doi:10.1002/grl.50507.

Goto, R., Nakayama, D., Takahashi, R., Pramudyo, E., Takuma, K., and Watanabe, N. (2023). Cooling-induced permeability enhancement for networks of microfractures in superhot geothermal environments. *Geothermal Energy, 11*(1). doi:10.1186/s40517-023-00251-9.

Goto, R., Sakaguchi, K., Parisio, F., Yoshioka, K., Pramudyo, E., and Watanabe, N. (2022). Wellbore stability in high-temperature granite under true triaxial stress. *Geothermics, 100*. doi:10.1016/j.geothermics.2021.102334.

Goto, R., Watanabe, N., Sakaguchi, K., Miura, T., Chen, Y., Ishibashi, T., Pramudyo, E., Parisio, F., Yoshioka, K., Nakamura, K., Komai, T., and Tsuchiya, N. (2021). Creating Cloud-Fracture Network by Flow-induced Microfracturing in Superhot Geothermal Environments. *Rock Mechanics and Rock Engineering, 54*, 2959-2974. doi:10.1007/s00603-021-02416-z.

Griffith, A. A. (1924). Theory of rupture. First International Congress on Applied Mechanics, (pp. 56-63).

Heidaryan, E., Hatami, T., Rahimi, M., and Moghadasi, J. (2011). Viscosity of pure carbon dioxide at supercritical region: Measurement and correlation approach. *The Journal of Supercritical Fluids, 56*(2), 144-151. doi:10.1016/j.supflu.2010.12.006.

Heuze, F. E. (1983). High-temperature mechanical, physical and Thermal properties of granitic rocks—A review. *International Journal of Rock Mechanics and Mining Sciences and Geomechanics Abstracts, 20*(1), 3-10. doi:10.1016/0148-9062(83)91609-1.

Hirose, T., Mizoguchi, K., and Shimamoto, T. (2012). Wear processes in rocks at slow to high slip rates. *Journal of Structural Geology, 38*, 102-116. doi:10.1016/j.jsg.2011.12.007.

Hsu, C.-J., and Schoenberg, M. (1993). Elastic waves through a simulated fractured medium. *Geophysics, 58*(7), 964-977. doi:10.1190/1.1443487.

Hu, L., and Ghassemi, A. (2020). Heat production from lab-scale enhanced geothermal systems in

granite and gabbro. *International Journal of Rock Mechanics and Mining Sciences, 126*. doi:10.1016/j.ijrmms.2019.104205.

Huang, K., Cheng, Q., Ghassemi, A., and Bauer, S. (2019). Investigation of shear slip in hot fractured rock. *International Journal of Rock Mechanics and Mining Sciences, 120*, 68-81. doi:10.1016/j.ijrmms.2019.05.006.

Hubbert, M. K., and Willis, D. G. (1957). Mechanics Of Hydraulic Fracturing. *Transaction of the AIME, 210*(1), 153-168. doi:10.2118/686-G.

Huttrer, G. W. (2020). Geothermal Power Generation in the World 2015-2020 Update Report. World Geothermal Congress (pp. 1-17). Reykjavik: *Proceedings World Geothermal Congress*.

Isaka, B. A., Ranjith, P. G., Rathnaweera, T. D., Wanniarachchi, W. M., Kumari, W. G., and Haque, A. (2019). Testing the frackability of granite using supercritical carbon dioxide: Insights into geothermal energy systems. *Journal of CO_2 Utilization, 34*, 180-197. doi:10.1016/j.jcou.2019.06.009.

Ishibashi, T., Watanabe, N., Asanuma, H., and Tsuchiya, N. (2016). Linking microearthquakes to fracture permeability change: The role of surface roughness. *Geophysical Research Letters, 43*(14), 7486-7493. doi:10.1002/2016GL069478.

Ishida, T., Chen, Y., Bennour, Z., Yamashita, H., Inui, S., Nagaya, Y., Naoi, M., Chen, Q., Nakayama, Y., and Nagano, Y. (2016). Features of CO_2 fracturing deduced from acoustic emission and microscopy in laboratory experiments. *Journal of Geophysical Research: Solid Earth, 121*(11), 8080-8090. doi:10.1002/2016JB013365.

Ishihara, S. (1991). Aji stone: the historical and modern use, and its geologic background. *Chishitsu News, 441*, 60-67. (in Japanese).

Jaeger, J. C., Cook, N. G., and Zimmerman, R. (2007). *Fundamental of rock mechanics (4 ed.)*. John Wiley and Sons.

Karásek, P., Šťavíková, L., Planeta, J., Hohnová, B., & Roth, M. (2013). Solubility of fused silica in sub-and supercritical water: Estimation from a thermodynamic model. *The Journal of Supercritical Fluids, 83*, 72-77. doi: 10.1016/j.supflu.2013.08.012.

Knill, J. L., Franklin, J. A., and Malone, A. W. (1968). A study of acoustic emission from stressed rock. *International Journal of Rock Mechanics and Mining Sciences and Geomechanics Abstracts, 5*(1), 87-88. doi:10.1016/0148-9062(68)90025-9.

Kwiatek, G., Saarno, T., Ader, T., Bluemle, F., Bohnhoff, M., Chendorain, M., Dresen, G., Heikkinen, P., Kukkonen, I., Leary, P., Leonhardt, M., Malin, P., Martínez-Garzón, P., Passmore, K., Passmore, P., Valenzuela, S., and Wollin, C. (2019). Controlling fluid-induced seismicity during a 6.1-km-deep geothermal stimulation in Finland. *Science Advances, 5*(5), eaav7224. doi: 10.1126/sciadv.aav7224.

Lin, W., Nakamura, T., and Takahashi, M. (2003). Anisotropy of thermal property, ultrasonic wave velocity, strength property and deformability in Inada granite. *Journal of the Japan Society of Engineering Geology, 44*(3), 175-187. doi:10.5110/jjseg.44.175.

Lu, S.-M. (2018). A global review of enhanced geothermal system (EGS). *Renewable and Sustainable*

Energy Review, 81, 2902-2921. doi:10.1016/j.rser.2017.06.097.

Manning, C. E. (1994). The solubility of quartz in H_2O in the lower crust and upper mantle. *Geochimica et Cosmochimica Acta, 58*(22), 4831-4839. doi: 10.1016/0016-7037(94)90214-3

Martell, A. E., Motekaitis, R. J., Fried, A. R., Wilson, J. S., and MacMillan, D. T. (1975). Thermal decomposition of EDTA, NTA, and nitrilotrimethylenephosphonic acid in aqueous solution. *Canadian Journal of Chemistry, 53*(22), 3471-3476. doi: 10.1139/v75-498.

Mitchell, E. K., Fialko, K., and Brown, K. M. (2013). Temperature dependence of frictional healing of Westerly granite: Experimental observations and numerical simulations. *Geochemistry, Geophysics, Geosystems, 14*(3), 567-582. doi:10.1029/2012GC004241.

Moridis, G. (2018). Literature review and analysis of waterless fracturing methods. *Lawrence Berkeley National Laboratory*.

Nemoto, K., Moriya, H., Niitsuma, H., and Tsuchiya, N. (2008). Mechanical and hydraulic coupling of injection-induced slip along pre-existing fractures. *Geothermics, 37*(2), 157-172. doi:10.1016/j.geothermics.2007.11.001.

Nishiyama, T., Chen, Y., Kusuda, H., Ito, T., Kaneko, K., Kita, H., & Sato, T. (2002). The examination of fracturing process subjected to triaxial compression test in Inada granite. *Engineering Geology*, *66*(3-4), 257-269. doi: /10.1016/S0013-7952(02)00046-7.

Nishiyama, T., and Kusuda, H. (1994). Identification of pore spaces and microcracks using fluorescent resins. *International Journal of Rock Mechanics and Mining Sciences and Geomechanics Abstracts, 31*(4), 369-375. doi:10.1016/0148-9062(94)90904-0.

Ohnaka, M. (1975). Frictional characteristics of typical rocks. *Journal of Physics of the Earth, 23*(1), 87-112. doi:10.4294/jpe1952.23.87.

Parisio, F., and Vilarrasa, V. (2020). Sinking CO_2 in Supercritical Reservoirs. *Geophysical Research Letters, 47*. doi:10.1029/2020GL090456.

Parisio, F., Yoshioka, K., Sakaguchi, K., Goto, R., Miura, T., Pramudyo, E., Ishibashi, T., and Watanabe, N. (2021). A laboratory study of hydraulic fracturing at the brittle-ductile transition. *Scientific Reports, 11*(1). doi:10.1038/s41598-021-01388-y.

Pine, R. J., and Batchelor, A. S. (1984). Downward migration of shearing in jointed rock during hydraulic injections. *International Journal of Rock Mechanics and Mining Sciences and Geomechanics Abstracts, 21*(5). doi:10.1016/0148-9062(84)92681-0.

Pinto, I. S., Neto, I. F., and Soares, H. M. (2014). Biodegradable chelating agents for industrial, domestic, and agricultural applications—a review. Environmental Science and Pollution Research, 21, 11893-11906. doi: 10.1007/s11356-014-2592-6.

Pramudyo, E., Goto, R., Sakaguchi, K., Nakamura, K., and Watanabe, N. (2022). CO_2 Injection-Induced Shearing and Fracturing in Naturally Fractured Conventional and Superhot Geothermal Environments. *Rock Mechanics and Rock Engineering, 56*(3), 1663-1677.

Pramudyo, E., Goto, R., Watanabe, N., Sakaguchi, K., Nakamura, K., and Komai, T. (2021). CO_2 injection-induced complex cloud-fracture networks in granite at conventional and superhot geothermal conditions. *Geothermics, 97*. doi:10.1016/j.geothermics.2021.102265.

Pruess, K. (2006). Enhanced geothermal systems (EGS) using CO_2 as working fluid—A novel approach for generating renewable energy with simultaneous sequestration of carbon. *Geothermics, 35*(4), 351-367. doi:10.1016/j.geothermics.2006.08.002.

Randolph, J. B., and Saar, M. O. (2011). Combining geothermal energy capture with geologic carbon dioxide sequestration. *Geophysical Research Letters, 38*(10). doi:10.1029/2011GL047265.

Rinaldi, A. P., Rutqvist, J., Sonnenthal, E. L., and Cladouhos, T. T. (2015). Coupled THM Modeling of Hydroshearing Stimulation in Tight Fractured Volcanic Rock. *Transport in Porous Media, 108*, 131-150. doi:10.1007/s11242-014-0296-5.

Rose, P. E., Xu, T., Fayer, S., and Pruess, K. (2010). Chemical Stimulation for EGS: the Use of Chelating Agents at High pH for the Simultaneous Dissolution of Calcium Carbonate, Silicas, and Silicates. *Proceedings World Geothermal Congress*.

Rutqvist, J., and Rinaldi, A. P. (2019). Fault reactivation and seismicity associated with geologic carbon storage, shale-gas fracturing and geothermal stimulation–Observations from recent modeling studies. *14th ISRM Congress*. OnePetro.

Salalá, L., Takahashi, R., Argueta, J., Wang, J., Watanabe, N., and Tsuchiya, N. (2023). Permeability enhancement and void formation by chelating agent in volcanic rocks (Ahuachapán and Berlín geothermal fields, El Salvador). *Geothermics, 107*. doi:10.1016/j.geothermics.2022.102586

Sasada, M. (1991). Inada granite. Chishitsu News, 441, 34-40. (in Japanese).

Secor, D. T. (1965). Role of fluid pressure in jointing. *American Journal of Science, 263*(8), 633-646. doi:10.2475/ajs.263.8.633.

Sokhanvarian, K., Nasr-El-Din, H. A., and de Wolf, C. A. (2016). Thermal stability of oilfield aminopolycarboxylic acids/salts. *SPE Production and Operations, 31*(01), 12-21. doi: 10.2118/157426-PA.

Takahashi, R., Wang, J., and Watanabe, N. (2023). Process and optimum pH for permeability enhancement of fractured granite through selective mineral dissolution by chelating agent flooding. *Geothermics, 109*. doi:10.1016/j.geothermics.2022.102646.

Takahashi, Y., Miyazaki, K., and Nishioka, Y. (2011). Plutonic rocks and metamorphic rocks in the Tsukuba Mountains. *J. Geol. Soc. Jpn., 117*, 21-31. doi:10.5575/geosoc.117.S21. (in Japanese).

Takaya, Y. (2011). Experimental study on alteration characteristics during chemical weathering of granite. *Geogr. Rev. Jpn. Ser. A., 84*, 131-144. doi:10.4157/grj.84.131. (in Japanese with English abstract).

Tester, J. W., Anderson, B. J., Batchelor, A. S., Blackwell, D. D., DiPippo, R., Drake, E. M., Garnish, J., Livesay, B., Moore, M. C., Nichols, K., Petty, S., Toksöz, M. N., and Veatch, Jr., R. W. (2006). Impact of Enhanced Geothermal Systems (EGS) on the United States in the 21st Century. Idaho National Laboratory, Renewable Energy and Power Department. Massachusetts Institute of Technology. Retrieved from https://energy.mit.edu/wp-content/uploads/2006/11/MITEI-The-Future-of-Geothermal-Energy.pdf.

Ueda, A., Kato, K., Ohsumi, T., Yajima, T., Ito, H., Kaieda, H., Metcalfe, R., and Takase, H. (2005). Experimental studies of CO_2-rock interaction at elevated temperatures under hydrothermal

conditions. Geochemical Journal, 39(5), 417-425.

Walendziewski, J., and Steininger, M. (2001). Thermal and catalytic conversion of waste polyolefines. *Catalysis Today, 65*(2-4), 323. doi:10.1016/S0920-5861(00)00568-X.

Wallroth, T., Eliasson, T., and Ulf, S. (1999). Hot dry rock research experiments at Fjällbacka, Sweden. *Geothermics, 28*(4-5), 617-625. doi:10.1016/S0375-6505(99)00032-2.

Wang, J., Watanabe, N., Inomoto, K., Kamitakahara, M., Nakamura, K., Komai, T., & Tsuchiya, N. (2022). Sustainable process for enhanced CO_2 mineralization of calcium silicates using a recyclable chelating agent under alkaline conditions. *Journal of Environmental Chemical Engineering, 10*(1), 107055. doi: 10.1016/j.jece.2021.107055.

Watanabe , N., Saito, K., Okamoto, A., Nakamura, K., Ishibashi, T., Saishu, H., Komai, T. and Tsuchiya, N. (2020). Stabilizing and enhancing permeability for sustainable and profitable energy extraction from superhot geothermal environments. *Applied Energy, 260*. doi:10.1016/j.apenergy.2019.114306.

Watanabe, N., Abe, H., Okamoto, A., Nakamura, K., and Komai, T. (2021a). Formation of amorphous silica nanoparticles and its impact on permeability of fractured granite in superhot geothermal environments. *Scientific Reports, 11*(1). doi:10.1038/s41598-021-84744-2.

Watanabe, N., Egawa, M., Sakaguchi, K., Ishibashi, T., and Tsuchiya, N. (2017b). Hydraulic fracturing and permeability enhancement in granite from subcritical/brittle to supercritical/ductile conditions. *Geophysical Research Letters, 44*(11), 5468-5475. doi:10.1002/2017GL073898.

Watanabe, N., Numakura, T., Sakaguchi, K., Saishu, H., Okamoto, A., Ingebritsen, S. E., and Tsuchiya, N. (2017a). Potentially exploitable supercritical geothermal resources in the ductile crust. *Nature geoscience, 10*, 140-144. doi:https://doi.org/10.1038/ngeo2879.

Watanabe, N., Sakaguchi, K., Goto, R., Miura, T., Yamane, K., Ishibashi, T., Chen, Y., Komai, T., and Tsuchiya, N. (2019). Cloud-fracture networks as a means of accessing superhot geothermal energy. *Scientific reports, 9*(1), 1-11. doi:10.1038/s41598-018-37634-z.

Watanabe, N., Takahashi, K., Takahashi, R., Nakamura, K., Kumano, Y., Akaku, K., Tamagawa, T., and Komai, T. (2021b). Novel chemical stimulation for geothermal reservoirs by chelating agent driven selective mineral dissolution in fractured rocks. *Scientific Reports, 11*(1). doi:10.1038/s41598-021-99511-6.

Wilkins, R., Menefee, A. H., and Clarens, A. F. (2016). Environmental Life Cycle Analysis of Water and CO2-Based Fracturing Fluids Used in Unconventional Gas Production. *Environmental Science and Technology, 50*(23). doi:10.1021/acs.est.6b02913.

Yamaguchi, U. (1970). The number of test-pieces required to determine the strength of rock. *International Journal of Rock Mechanics and Mining Sciences and Geomechanics Abstracts, 7*(2), 209-227. doi:10.1016/0148-9062(70)90013-6.

Ye, Z., and Ghassemi, A. (2018). Injection-Induced Shear Slip and Permeability Enhancement in Granite Fractures. *Journal of Geophysical Research: Solid Earth, 123*(10), 9009-9032. doi:10.1029/2018JB016045.

Ye, Z., and Ghassemi, A. (2019). Injection-induced propagation and coalescence of preexisting fractures in granite under triaxial stress. *Journal of Geophysical Research: Solid Earth, 124*(8), 7806-7821. doi:10.1029/2019JB017400.

Ye, Z., and Ghassemi, A. (2020). Heterogeneous Fracture Slip and Aseismic-Seismic Transition in a Triaxial Injection Test. *Geophysical Research Letters, 47*(14). doi:10.1029/2020GL087739.

Achievements

Journal papers (International/Peer-reviewed)

Goto, R., Nakayama, D., Takahashi, R., Pramudyo, E., Takuma, K., and Watanabe, N. (2023). Cooling-induced permeability enhancement for networks of microfractures in superhot geothermal environments. *Geothermal Energy, 11*(1), 1-24.

Pramudyo, E., Goto, R., Sakaguchi, K., Nakamura, K., and Watanabe, N. (2022). CO_2 Injection-Induced Shearing and Fracturing in Naturally Fractured Conventional and Superhot Geothermal Environments. *Rock Mechanics and Rock Engineering, 56*(3), 1663-1677. (Presented in Chapter 3).

Goto, R., Sakaguchi, K., Parisio, F., Yoshioka, K., Pramudyo, E., and Watanabe, N. (2022). Wellbore stability in high-temperature granite under true triaxial stress. *Geothermics, 100*, 102334.

Pramudyo, E., Goto, R., Watanabe, N., Sakaguchi, K., Nakamura, K., and Komai, T. (2021). CO_2 injection-induced complex cloud-fracture networks in granite at conventional and superhot geothermal conditions. *Geothermics, 97*, 102265. (Presented in Chapter 2).

Parisio, F., Yoshioka, K., Sakaguchi, K., Goto, R., Miura, T., Pramudyo, E., Ishibashi, T. and Watanabe, N. (2021). A laboratory study of hydraulic fracturing at the brittle-ductile transition. *Scientific reports, 11*(1), 22300.

Goto, R., Watanabe, N., Sakaguchi, K., Miura, T., Chen, Y., Ishibashi, T., Pramudyo, E., Parisio, F., Yoshioka, L., Nakamura, K., Komai, T. and Tsuchiya, N. (2021). Creating cloud-fracture network by flow-induced microfracturing in superhot geothermal environments. *Rock Mechanics and Rock Engineering, 54*, 2959-2974.

International Conference Papers

Pramudyo, E., Goto, R., Sakaguchi, K., Nakamura, K., and Watanabe, N. (2022, November). CO_2 Injection-Induced Shearing and Complex Fracturing in Naturally Fractured Geothermal Environment. *Nineteenth International Conference on Flow Dynamics*, Sendai, Japan November 9 – 11 2022.

Goto R., Pramudyo, E., Watanabe, N., Sakaguchi, K., Chen, Y. and Komai, T. (2021, September). Flow-Induced Microfracturing of Granite in Conventional and Superhot Geothermal Environments. *SPWLA 26th Formation Evaluation Symposium of Japan*.

Goto R., Pramudyo, E., Miura, T., Watanabe, N., Sakaguchi, K., Komai, T., and Tsuchiya, N. (2021). Hydraulic fracturing and permeability enhancement in granite at supercritical temperatures, *Proceedings World Geothermal Congress 2020+1*.

Pramudyo, E., Watanabe, N., Takeyama, S., Goto, R., Miura, T., Hattori, K., Sakaguchi, K. and Komai, T. (2019, September). Supercritical carbon dioxide fracturing of granite from conventional to superhot geothermal conditions. *SPWLA 25th Formation Evaluation Symposium of Japan*. OnePetro.

Conference Presentations (Oral)

Pramudyo, E., Goto, R., Sakaguchi, K., and Watanabe, N. (2023). Shear-slip and Complex Fracturing by CO_2 Injection in Naturally Fractured Granite at Geothermal Conditions. *EGU General Assembly 2023*, Vienna, Austria, 24–28 Apr 2023. (International).

Pramudyo, E., Goto, R., Sakaguchi, K., Nakamura, K., and Watnabe, N. (2022). CO_2 Injection-Induced Shearing and Complex Fracturing in Naturally Fractured Geothermal Environment. *Nineteenth International Conference on Flow Dynamics*, Sendai, Japan November 9 – 11 2022. (International).

Pramudyo, E., Watanabe, N., Goto, R., Sakaguchi, K., Nakamura, K., and Komai, T.: Characteristics and mechanism of CO_2-based fracturing of granite in conventional and superhot geothermal environments. *EGU General Assembly 2021*, online, 19–30 Apr 2021, EGU21-10538. (International).

Conference Presentation (Poster)

Pramudyo, E., Watanabe, N., Goto, R., Miura, T., Takeyama, S., Hattori, K., Nakamura, K., Sakaguchi, K., and Komai, T. (2020, March). Carbon Dioxide-based Fracturing of Granite under Conventional to Superhot Geothermal Conditions. *17th International Workshop on Water Dynamics*. (International; Abstract only).

Pramudyo, E., Watanabe, N., Takeyama, S., Goto, R., Hattori, K., Nakamura, K., Sakaguchi, K., and Komai, T. (2019, June). Supercritical Carbon Dioxide Fracturing of Granite at Geothermal Conditions. *Mining and Materials Processing Institute of Japan (MMIJ) annual conference* (Domestic).

Pramudyo, E., Watanabe, N., Goto, R., Takeyama, S., Nakamura, K., and Komai, T., (2019, March). Gas-based Fracturing in Granite from Subcritical/Brittle to Supercritical/Ductile Conditions. *16th International Workshop on Water Dynamics*. (International).

Awards

2022 Japanese Society for Rock Mechanics (JSRM) Paper Award: Goto, R., Watanabe, N., Sakaguchi, K., Chen, Y., Ishibashi, T., and Pramudyo, E.. Creating Cloud-Fracture Network by Flow-Induced Microfracturing in Superhot Geothermal Environments.

2020 SPWLA International Student Paper Contest: 1st place oral MSc category. Pramudyo E., Watanabe, N., Goto, R., Takeyama, S., Sakaguchi, K., and Komai, T. (2020, June). Creating complex fracture patterns at lower pressures by CO_2-based fracturing in granite from conventional to superhot geothermal conditions.

2019 Japan Formation Evaluation Society (JFES) best presentation and extended abstract: Pramudyo, E., Watanabe, N., Takeyama, S., Goto, R., Miura, T., Hattori, K., Sakaguchi, K. and Komai, T. (2019, September). Supercritical carbon dioxide fracturing of granite from conventional to superhot geothermal conditions. In SPWLA 25th Formation Evaluation Symposium of Japan.

Acknowledgements

First of all, the author would like to express his deep sense of gratitude to Prof. Noriaki Watanabe, who has been a wonderful-research and academic supervisor. Prof. Watanabe tutored the author with extreme patience and tolerance, throughout the course of the author's master's and doctoral study in the Resource and Energy Security Science Laboratory of Tohoku University. The author has learned abundance of valuable lessons from Prof. Watanabe.

Sincere gratitude is presented to the members of the dissertation-reviewing committee: Prof. Atsushi Okamoto, Assoc. Prof. Kiyotoshi Sakaguchi, Assoc. Prof. Masaoki Uno, and Assist. Prof. Jiajie Wang. This dissertation has been significantly improved through comments and suggestions they provided.

The author is indebted to Prof. (emeritus) Takeshi Komai, who provided the opportunity to join the Resource and Energy Security Science Laboratory of Tohoku University when the author started his master's study. The author also extended his gratitude to Assist. Prof. Nakamura Kengo who provided various assistances in the author's research activity. Needless to say, the kindness and supports from laboratory technical assistant Ms. Noriko Isogai, as well as all fellow students of this laboratory, could not be overlooked.

The author would like to thank the Japan Society for the Promotion of Science (JSPS) which partially supported this study through Grants-in-Aid for Scientific Research (B) (no. 22H02015), Challenging Research (Pioneering) (no. 21K18200), and JSPS Fellows (no. 20J20108). The author would like to thank Toei Scientific Co., Ltd. for manufacturing the experimental system. The author also would like to thank Editage (www.editage.com) for English language editing.

Finally, the author expresses his appreciation for supports from countless parties; the author wishes wonderful life be always with them.